MOLECULAR INSIGHTS INTO THE CONFORMATIONAL CONVERSION, NANOSCALE ASSEMBLY AND STRUCTURAL HETEROGENEITY OF PRIONS AND AMYLOIDS

VIJIT DALAL

Thesis submitted for the partial fulfillment of the degree of

DOCTOR OF PHILOSOPHY

Department of Biological Sciences

Indian Institute of Science Education and Research (IISER) Mohali

November 2015

Dedicated

to

my family

Declaration

The work presented in this thesis has been carried out by me under the supervision of Dr. Samrat Mukhopadhyay at the Department of Biological Sciences, Indian Institute of Science Education and Research (IISER) Mohali.

This work has not been submitted in part or full for a degree, a diploma, for a fellowship to any university or institute.

Whenever contribution of others are involved every effort is made to indicate this clearly, with due acknowledgment of collaborative research and discussions. This thesis is a bona fide record of original work done by me and all sources listed within have been detailed in the bibliography.

Date Place Vijit Dalal

In my capacity as supervisor of the candidate's thesis work, I certify that above statements by the candidate are true to the best of my knowledge.

Dr. Samrat Mukhopadhyay

(Supervisor)

Acknowledgement

Though only my name appears on the cover of this thesis, a great many people have contributed to the work described herein. It gives me immense pleasure to convey my gratitude to all those people as without their help, advices and support it would not have been possible for me to write my thesis.

First and foremost, I owe my deepest gratitude to my Ph.D. supervisor Dr. Samrat Mukhopadhyay whose expertise, understanding, and patience, added considerably to my graduate experience. I have been amazingly fortunate to have a supervisor who gave me the freedom to explore on my own and at the same time the guidance to recover, when my steps faltered. I thank him for providing an excellent scientific environment, stimulating discussions and for having immense faith in me. He has been a source of motivation and enthusiasm. He helped me to overcome many crisis situations during this journey. My strong work ethics and enthusiasm for my research, is attributed entirely to my supervisor. His mentorship has helped me a lot in developing scientific temperament and skills. Samrat taught me how to question thoughts and express ideas. I am also thankful to him for encouraging the use of correct grammar and consistent notation in my writings, for carefully reading and commenting on countless revisions of my manuscripts and the countless efforts he has put to teach me not only research but also how to communicate my ideas effectively. I am indebted to him for his continuous encouragement and guidance. I appreciate his vast knowledge and skill in many areas. One simply could not wish for a better or friendlier supervisor.

I am thankful to Dr. Mily Bhattacharya (SERB-DST Young Scientist). She is one of the best teachers that I have had in my life who truly made a difference in my life. She has been always there to listen my problems and gave advices. I am deeply grateful to her for unconditional help and encouragement and for the insightful discussions that helped me to sort out the technical details of my work and for all her efforts she invested in revising my manuscripts. Without her support it would not have been possible for me to conduct the research described in chapter 5.

I would like to thank my doctoral committee members Dr. Purnananda Guptasarma and Dr. Kavita Babu for their valuable suggestions on my work and presentations.

I am thankful to all the former and present lab members of The Mukhopadhyay Lab for their cordiality and contribution to make my stay a memorable one. This includes Mily, Pushpender, Neha, Arpana, Mitun, Dominic, Karishma, Hemaswasthi, Priyanka, Priyanka Jr., Anubhuti, Shruti, Nilanjana, Simarbir, Shikha and Shwetha. It was a pleasure working with them.

I am grateful to Dr. Mahak Sharma for discussions, helping in learning different aspects of cell biology, for allowing me to work in her laboratory with all her resources and for the collaborative research described in chapter 4. I am also very thankful to her lab members and my friends Divya and Ritu for their great help in cell biology experiments. Ritu helped me extensively in image analysis.

I would like to acknowledge Dr. Purnananda Guptasarma for providing the human prion protein (90-231) plasmid and Dr. Prof. Roberto Chiesa. (Department of Neuroscience, IRCCS-Mario Negri Institute for Pharmacological Research, Milan, Italy) for providing GFP-PrP^{C} plasmid.

The enormous support from members of other laboratories is greatly appreciated. I am also thankful to the official staff at IISER Mohali for their support and taking care of all the paper work.

I am thankful to IISER Mohali for providing all the facilities and the financial support throughout my thesis.

I would like to express my sincere appreciation to all my friends. I owe a special thanks to my beautiful friend Puneet whose support and care helped me to overcome setbacks. I greatly value her friendship and deeply appreciate her belief in me.

Most importantly, I am very thankful to the Almighty for blessing me with the best parents in the world. None of this would have been possible without the love and patience of my family. My parents to whom this dissertation is dedicated to, has been a constant source of love, concern, support and moral and spiritual strength all these years. I would like to express my heart-felt gratitude to my husband Dr. Devendra Kumar Gupta for his incessant love, support and care that helped to stay focused on my graduate study and gave me the strength to finish this journey.

Synopsis

Molecular Insights into the Conformational Conversion, Nanoscale Assembly and Structural Heterogeneity of Prions and Amyloids

Chapter 1: Introduction

Prion diseases belong to a unique class of fatal neurodegenerative disorders classified as transmissible spongiform encephalopathies that are caused by conformational transition of largely α-helical normal cellular form (PrP^{C}) into a predominantly β-sheet-rich scrapie form (PrP^{Sc}). The proteinaceous infectious agents have a fascinating property of being infectious, genetic and sporadic in nature. In the past several years, there is a quantum jump in the prion research that improves our understanding and also opens new avenues for further research. Yet, the fundamental questions about prions remain elusive. In this thesis, we steered our efforts to understand the mechanistic details of prion protein misfolding and aggregation and the factors influencing the pathogenic conformational switching event. By using a diverse array of spectroscopic and microscopic techniques coupled with other biochemical and cell biological tools, we deciphered the molecular mechanism of the prion protein misfolding into oligomers and protease resistant cytotoxic amyloid fibrils (PrPres) (Figure 1).

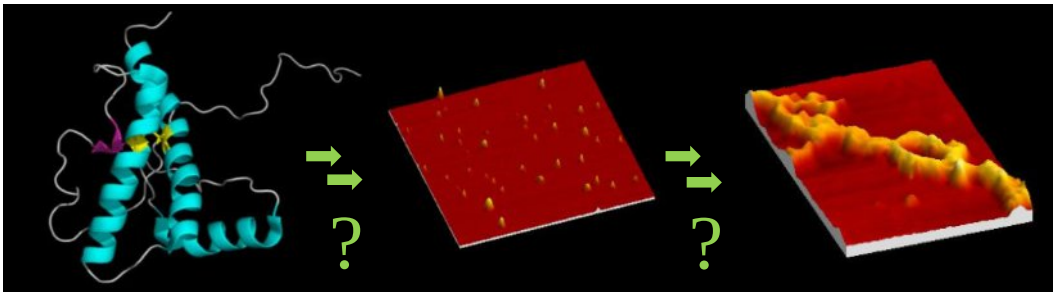

Figure 1. Conformational switching of PrP into protease resistant amyloid fibrils *via* oligomeric intermediates.

Our work provides the biophysical insights into the key early on-/off- pathway intermediates, the role of hydration dynamics in the on-pathway oligomers and the morphological characterization of the amyloid fibrils. Additionally, we put forward the use of near-field scanning optical microscopy in providing the structural underpinnings of protein amyloid fibrils at the nanoscopic spatial resolution beyond the optical diffraction-limit. Taken

together, we believe that the work presented in this thesis not only improves our present knowledge about prions biogenesis but, also holds significance in understanding the underlying origin of various neurodegenerative disorders including Alzheimer's and Parkinson's diseases that are caused by prion-like conformational switching mechanism.

<u>Chapter 2:</u> Conformational Switching and Nanoscale Assembly of Human Prion Protein into Diverse Polymorphic Amyloids *via* Structurally-Labile Oligomers

Conformational switching of the prion protein (PrP) from an α-helical normal cellular form (PrP^{C}) to self-propagating β-rich scrapie form (PrP^{Sc}) underlies the etiology of prion diseases. Anionic lipids play a critical role in the misfolding and conformational conversion of the membrane-anchored PrP into the amyloidogenic pathological form. In this study, we have used a diverse array of techniques to interrogate the early intermediates during amyloid formation from recombinant human PrP in the presence of a membrane mimetic anionic detergent such as sodium dodecyl sulfate. We have been able to detect and characterize two distinct types of interconvertible oligomers. Our results demonstrate that highly ordered large β-oligomers represent benign off-pathway intermediates that lack the ability to mature into amyloid fibrils. On the contrary, structurally-labile small oligomers are capable of switching to an ordered amyloid-state that exhibits profound toxicity to mammalian cells (Figure 2). The fluorescence resonance energy transfer measurements revealed that the partially

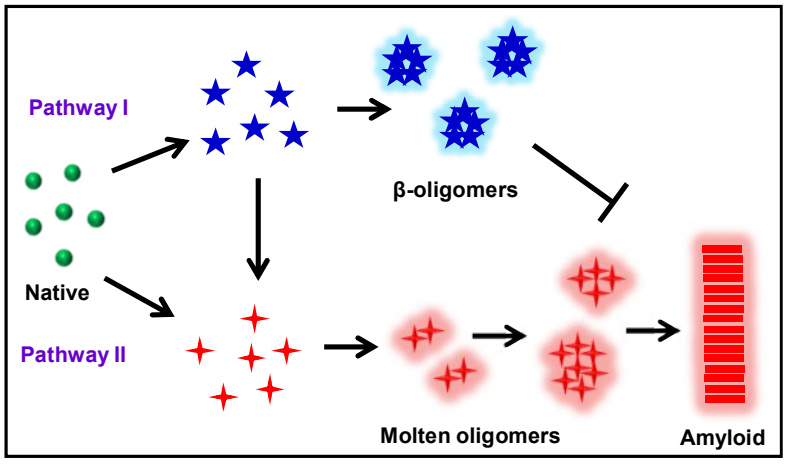

Figure 2. Proposed schematic model for PrP aggregation. (Dalal V. et al. *Biochemistry* 2015)

disordered PrP serves as precursors to small amyloid-competent oligomers. These on-pathway oligomers are eventually sequestered into higher order supramolecular assemblies

that conformationally mature into polymorphic amyloids possessing varied nanoscale morphology as evident by the atomic force microscopy imaging. The nanoscale diversity of fibril architecture is attributed to the heterogeneous ensemble of early obligatory oligomers and offers a plausible explanation for the existence of multiple prion strains *in vivo*.

<u>Chapter 3:</u> Investigation of Ordered Water within the Oligomers of the Human Prion Protein

The conformational conversion of the prion protein (PrP) into diseased scrapie isoform involves the obligatory partial unfolding of the native structure and oligomerization (PrP*). The mobility of water molecules in the hydration layer is coupled with the fluctuations in the protein structure and mediates several important functions including intermolecular protein-protein interactions and self assembly into aggregates. In this work, we addressed the various conformational and hydration attributes of the native prion protein, off-pathway structured β-oligomers and on-pathway disordered oligomers. In order to characterize the structural role of the ordered water molecules we have selected the C-terminus end region of the PrP comprising significant number of underwrapped backbone hydrogen bonds that are prone to water attack. The time-resolved fluorescence was used to establish the considerable motional flexibility of the probe in the on-pathway oligomers.

Using solvation dynamics measurements we observed a much impeded time scale (~ 1 ns) of water relaxation around the on-pathway disordered oligomers that is orders of magnitude slower than the bulk water and can be ascribed to the bound ordered water molecules. We

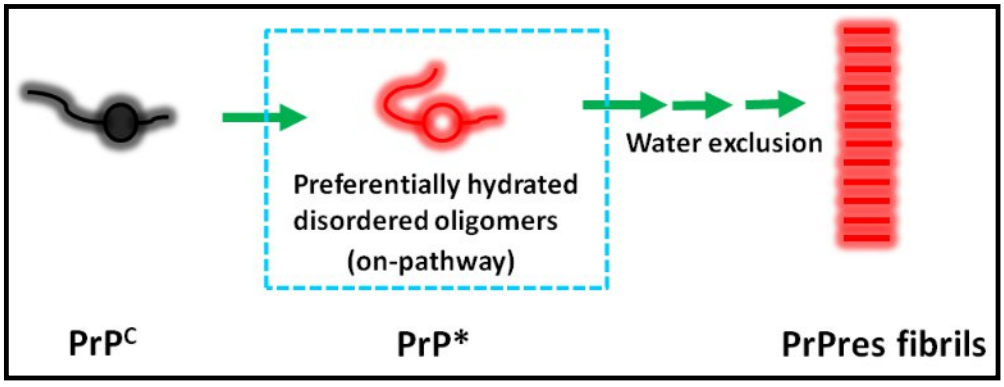

Figure 3. Proposed role of hydration dynamics in PrP oligomerization and amyloid fibrils. (Dalal V. et al. manuscript under review)

speculate that the preferentially hydration stabilizes the unstructured oligomers, exquisitely mediate the intermolecular interactions between oligomers and entropically favor the formation of amyloid fibrils by exclusion of the ordered water molecules (Figure 3). Moreover, the dynamic role of water molecules in aggregation opens a new avenue for better understanding of the neurodegenerative diseases caused by protein misfolding.

Chapter 4: Trafficking of Cellular Prion Protein and its Disease Related Mutants

PrP^{C} is a glycoprotein tethered to the outer cell surface of plasma membrane by glycosyl-phosphatidylinositol anchor and mostly localized in the lipid rafts. To discern the transition of PrP^{C} to its pathologic conformation it is imperative to delineate the trafficking pathway of PrP^{C} and its various disease related isoforms. The precise mechanism of prion protein endocytosis is still unclear. There are conflicting reports that suggest the role of both caveolae- and clathrin- dependent mechanism in the internalization of PrP^{C} in the different cell types. In this study, we carried out the initial colocalization experiments to get insights into the trafficking of PrP^{C} and its disease related mutants. In order to examine the behavior of PrP isoforms in the cultured cells we have used two different mutants, D177N and E200K, related to inherited prion diseases. The Confocal analysis demonstrates that both wild-type PrP^{C} and mutants colocalizes with the golgi marker, giantin. But the mutant isoforms of PrP^{C} exhibit an impaired transportation to the cell surface and accumulate in form unusual punctate structures (Figure 4). Currently, we are investigating the identity of these subcellular punctate compartments. These preliminary results lay the foundation of future experiments in the lab targeting trafficking of prion protein isoforms that is crucial to understand the cellular sites of PrP^{C} and PrP^{Sc} interaction and the biogenesis of PrP^{Sc}.

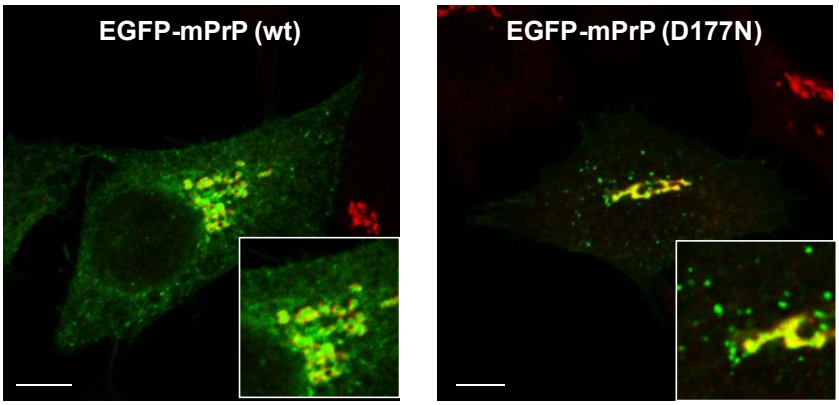

Figure 4. Confocal scanning fluorescence imaging of PrP isoforms in the HeLa cells.

<u>Chapter 5:</u> Nanoscale Fluorescence Imaging of Single Amyloid Fibrils

Prions and other amyloids are implicated in a variety of debilitating human diseases. The amyloid aggregates being nanoscopic in dimensions do not lend themselves to the conventional microscopic resolution which is hindered by the diffraction limit. The salient enigmatic features of prions e.g. the ability to self propagate, species barrier and the molecular basis of strain phenomenon and toxicity are believed to be encrypted in the aggregates structure. Therefore, it is important to perform high-resolution fluorescence imaging of individual amyloid fibrils to optically map the structural basis of amyloid fibrils far beyond the diffraction-limit. We have developed super-resolution fluorescence imaging method to look into amyloid architecture using near-field scanning optical microscopy with the future aim to investigate prions species barrier. In this work, we have used fluorescently stained amyloid fibrils derived from disease-associated human β_2-microglobulin to establish the potentials of the near-field scanning fluorescence microscopy (Figure 5). Human β_2-microglobulin serves as a model amyloid-forming protein to investigate protein aggregation. Moreover, its amyloid formation is well characterized; it reproducibly forms fibrils of desired morphology under given conditions. Using this high-resolution nanophotonic technique, we were able to resolve the fibrils that were spatially separated by ~ 75 nm. Interrogation of individual fibrils along its length by simultaneously monitoring both nanoscale topography and fluorescence brightness revealed heterogeneous packing of the amyloid cross-beta architecture. We anticipate that this method holds promise to detect conformational distributions and heterogeneity in the amyloids that are believed to correlate with the supramolecular packing of misfolded proteins within the fibrils that underlie the structural basis of the strain phenomenon in prion and amyloid biology.

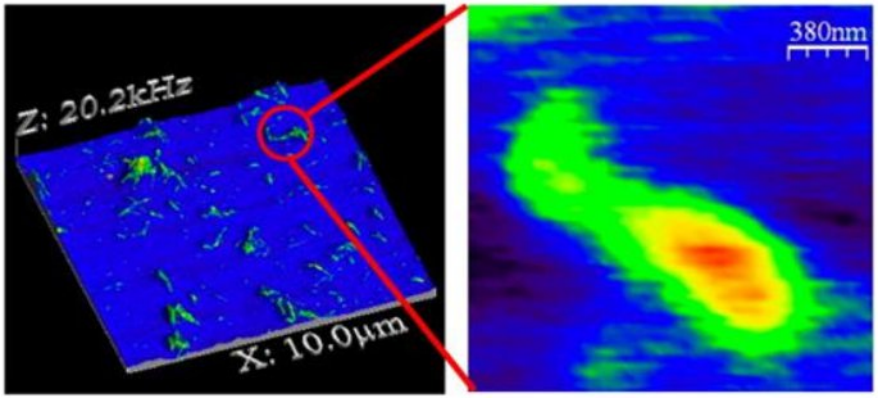

Figure 5. NSOM imaging of amyloid fibrils. (Dalal V. et al. *J. Phys. Chem. Lett.* 2012)

Table of Contents

Chapter 1

Introduction

1.1 Prion diseases

Prion diseases are fatal neurodegenerative disorders that affect humans and other mammals. In humans prion diseases are marked in form of different syndromes such as Kuru, Creutzfeldt-Jacob disease (CJD), Gerstmann-Sträussler-Scheinker (GSS) syndrome and fatal familial insomnia (FFI). The animal prion diseases include bovine spongiform encephalopathy or 'mad cow' disease in cattle, scrapie in sheep and chronic wasting disease in cervids (1-3). In humans prion encephalopathies are characterized by the progressive dementia accompanied by cognitive impairments and motor dysfunction such as myoclonus, cerebellar ataxia and pyramidal and extra pyramidal signs leading to extensive neurodegeneration. FFI disease symptoms include dysautonomia and sleep disorders. After a protracted incubation time the disease appears insidiously and death usually occurs within months (CJD, Kuru and FFI) and years (GSS) after the appearance of symptoms (4,5) . Due to neuronal degeneration the diseased brain tissue is characterized by sponge-like microscopic appearance and thus, prion disorders are also classified as transmissible spongiform encephalopathies (TSE) (6). Prion diseases are unique as they are manifested in three different forms: sporadic, genetic and infectious (7). In humans, TSE is a very rare disease; CJD has a sporadic origin and is the most common of all prion disorders which occurs at a rate of 1 in every 1 million population per year (8).

Scrapie was first documented as an infectious neurological disease in 1939 after experimentally transmitting it to goats (9). In 1954, Gajdusek highlighted that Kuru which was decimating the Fore tribe in Papua New Guinea was caused by the cannibalistic practice. The initial attempts of transmitting Kuru failed due to the longer incubation period of the disease (10). Later William Hadlow pointed out the resemblance between Kuru and scrapie and following his suggestion Gajdusek in 1966 demonstrated the transmissible and infectious nature of Kuru by experimentally transmitting it to non-human primates (11). A few decades ago, the BSE outbreak in United Kingdom caused death of thousands of cattle and approximately 150 human lives succumbed to death by a new variant CJD (vCJD) generated by transmission of prions from BSE contaminated beef (12). This inadvertent spread of TSE in form of a new variant aroused an alarming issue due to the transmissible nature of prions through food chain and also by the use of contaminated neurosurgical instruments (13,14). The species specificity and existence of different prion strains was first hypothesized by Pattison in 1961 and later it was also observed in closely related species like hamster and mice (15). Although prion diseases are rare in nature but, the various perplexing properties

associated with prions have shrouded the minds of scientists. Nonetheless, the existence of different prions strains and interspecies transmission also pose a threat to human health (16).

The exact nature of prion pathogenic agent has been in question since the mid-1960. Different experiments for transmission of prion variants to different recipient species revealed the strain properties and also suggested the requirement of long incubation periods (6). To explain the hybrid and phenotypically distinct pathology virion hypothesis was initially proposed and infectivity was postulated to be caused by slow virus (17). However, the infectious agent was later found to be resistant against nuclease treatment and UV radiation which suggested that the infectious agent lacks nucleic acid and could not be virus (18,19). After performing meticulous and painstaking experiments, Prusiner proposed the protein-only hypothesis to explain the proteinaceous nature of the infectious element. According to protein-only hypothesis, the scrapie infectious agent is a protein that self-replicates itself in the host and has transmissible properties. The novel pathogen was termed as prion (proteinaceous infectious particle) (6). This discovery was based on various ground-breaking experiments e.g. isolation of protease resistant scrapie protein from infected animals brain (20). Prusiner in collaboration with Weissmann and Hood found out the amino acid sequence of scrapie peptide fragment that was utilized to characterize the DNA sequence. These experiments established that scrapie protein is a host-encoded protein called prion protein and *Prnp,* gene encodes the cellular prion protein (PrP^{C}) (21,22). The infectivity titer was proportionate to the concentration of brain extracted scrapie form. Moreover, the treatment of brain purified scrapie prion protein with detergents and anti-prion antibodies hampered the infectivity (23). The generation of scrapie prion protein (PrP^{Sc}) till now is best explained by the protein-only hypothesis which suggests that PrP^{Sc} replicates and amplifies itself by interacting and imposing its conformation on PrP^{C} (6). This postulate is also reinforced by the fact that inoculation of PrP^{Sc} in the normal mice induces the conversion of host PrP^{C} into PrP^{Sc} and prion pathogenesis. Moreover, ablation of *Prnp* in mice lead to complete resistance to prion diseases (24,25). The protein-only hypothesis also satisfies the John Griffth original intuition that scrapie infectious agent correspond to a self-replicating protein (26). Nonetheless, if PrP^{Sc} generation requires only PrP^{C}, the infectivity has not been produced under entirely *in vitro* conditions. To explain this unified theory has been suggested. It combines the protein-only and nucleic acids postulates and proposes that $PrP^{C} \rightarrow PrP^{Sc}$ is the central etiological event but the conversion, infectivity and strain behavior are dictated by an another element co-prion that co-purifies with brain derived PrP^{Sc} (27).

Thus, prion diseases are caused by the conformational conversion of normal, soluble in non-ionic detergent, protease-sensitive cellular prion protein (PrP^{C}) into an aberrant, less soluble, proteinase K-resistant pathogenic scrapie isoform (PrP^{Sc}). And, prions are novel self-propagating infectious agent composed of mainly (if not only) PrP^{Sc} and exhibit non-Mendelian inheritance (6,25). After decades of relentless effort, our understanding of prion diseases has improved considerably. But, still molecular mechanism in prion biology is poorly understood and there are several fundamental issues that need to be addressed, for example, the mechanistic details of the conversion process and factors influencing the transition, mechanism of neurodegeneration, strain phenomenon and species barrier, structural details of PrP^{Sc}, exact composition of infectious agent, neuroinvasion of the digested prions and of course physiological function of PrP^{C} (1).

1.2 The cellular prion protein (PrP^{C})

The human PrP^{C} is synthesized from *PRNP* gene (human prion protein gene) which is located on the short arm of chromosome 20 at position p12 and mouse PrP^{C} is present on chromosome 2. The PRNP gene is highly conserved in all mammalian species and contains three exons. Exon 3 constitutes the entire open reading frame for mRNA transcription and for the synthesis of mature PrP^{C} consisting 208 amino acids (28). PrP^{C} demonstrate extensive sequence homology (approximately 80%) from amphibians to mammals. PrP^{C} is ubiquitously expressed by various cells/tissues in our body e.g. lymphocyte, stromal cells of lymphoid organ, leukocytes, kidney, heart, digestive tract, muscle etc. but its expression is highest in neurons (29). Albeit PrP^{C} is produced in the highest amount in brain compared to other body tissues; it constitutes less than 0.1% of the total protein in the central nervous system (30). Thus, owing to the low quantity and impurities associated with the purified protein, natural PrP^{C} is not suitable for high-resolution structural studies. These obstacles were surmounted by expressing PrP in the bacterial system that also provides the advantage of labeling with heavy atoms like ^{15}N or ^{13}C. Although the recombinant PrP lack the post-translation modifications (glycosylation and GPI-anchor), it is used as surrogate of PrP^{C} for structural investigations (30). The high-resolution three dimensional structure of PrP has been solved using NMR spectroscopy and X-ray crystallography. In its native soluble free form the N-terminus region of the mature protein encompassing residues 24 to 125 is disordered and conformationally-flexible (Figure 1.1b). The C-terminal region from residues 126 to 228 is structured and assembled in a globular domain that consists of three α-helices (helix 1: 144–154, helix 2: 173–194 and helix 3: 200–228) and two short antiparallel β-sheets comprising

residues 128–131 and 161–164. Helix 2 and helix 3 are bridged by single disulfide bond between Cys179–Cys214 which is very essential for attaining the native helical structure (Figure 1.1b). The loop of residues 166-171, between the β-sheet and helix 2 is not well-defined because of structural disorderness. So, within the structured C-terminus, the loop (166-171), end of helix 2 (187-194) and C-terminal part of helix 3 (219-228) exhibit increased structural flexibility (31,32). The structural comparison of human PrP with murine and Syrian hamster PrP revealed that the length of helix 3 matches with the Syrian hamster PrP and the structurally flexible loop of residues 166-171 coincide with the mouse PrP. The loop 166-171 and C-terminus residues of helix 3 are structurally and functionally very interesting because the minor structural difference between the human and bovine PrP or mouse and hamster PrP have been mapped in these regions. And, this region also serves as the binding site of putative not–well characterized protein X which is believed to mediate the conformational change. This suggests that the species-specific differences in PrP such as species-barrier and immunity of certain species to prion diseases are enciphered in the amino acid sequence and in the structure. All these structural information is based on recombinant PrP and not on PrP^C assuming that two N-linked glycosylation at Asn181 and Asn197 and GPI- anchor do not influence the structure significantly. Additionally, the N-terminal disordered segment has five octapeptide repeats that bind to copper/zinc ions in a co-operative fashion that would stimulate structure formation in this region that might influence the local conformational state of the globular domain (30,31).

1.3 Function of PrP^C and its various interacting partners

The highly evolutionary conserved nature of PrP^C point out its relevant role in biological processes. The physiological function of PrP^C has been extensively studied but it is not well-defined. To decipher the functional importance of PrP^C scientists aim to characterize its various binding partners by yeast two-hybrid screens, co-immunoprecipitation, cross-linking and other methods. Given the outer cell surface localization of PrP^C a plethora of binding partners have been identified like laminin receptor, neural cell-adhesion molecules, casein kinase2, p75 neurotrophin receptor, synapsin b1, potassium channel TREK-1, caveolin, Grb-2 and Pint1 suggesting the potential role in cell adhesion, ligand uptake and is also hypothesized as potential membrane signaling candidate by acting as a recognition molecule (33-35). Nonetheless, the biological significance of many of these interactions is not clear as many of the identified molecules are primarily cytoplasmic and their direct interaction with PrP^C is unlikely. PrP^C is also involved in signal transduction by up regulating

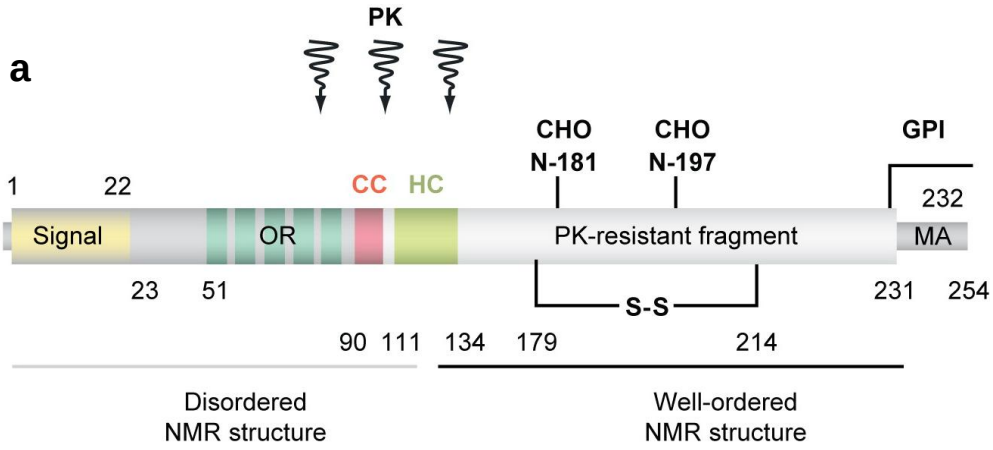

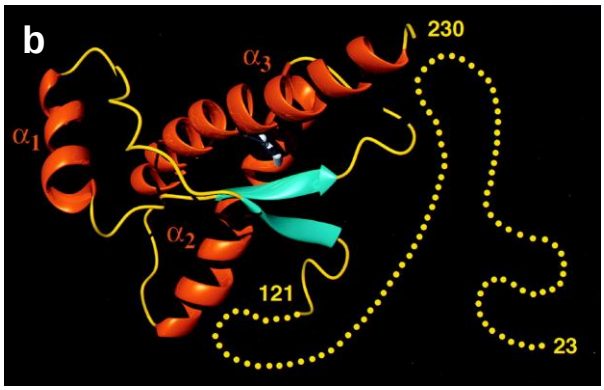

c

Biochemical properties

PrP^{C}	PrP^{Sc}
Rich in α-helices	Rich in β-sheets
Soluble	Insoluble
PK sensitive	PK resistant
No aggregation	Aggregation

Figure 1.1 (a) Schematic depicting organization of the cellular prion protein including its post-translational modifications. The secretory signal peptide is present at the extreme N-terminus. The numbers denote the respective positions of the amino acids. The proteinase K (PK) resistant core of PrP^{Sc} is shown in gray. The arrows indicate the variable cleavage site of proteinase K between amino acids 78–102 in PrP^{Sc}. OR (*dark green*): octapeptide-repeats; CC (*pink*): charged cluster; HC (*green*), hydrophobic core; S-S, single disulfide bridge; MA: membrane anchor segment; GPI: glycosyl phosphatidylinositol; CHO: glycosylation sites. Adapted from reference 3. (b) Cartoon representation of the three-dimensional structure of the human prion protein (23–230). The α-helices are shown in orange, anti-parallel β-sheets in cyan, disulfide bond between helix 2 and helix 3 in blue-white dots and N-terminal disordered segment in yellow dots. Adapted from reference 31; Copyright 2000 National Academy of Sciences, U.S.A. (c) Comparison of the biochemical features of PrP^{C} and PrP^{Sc}. Adapted from reference 3.

the phosphorylation levels of the tyrosine kinase Fyn, and caveolin-1 and Grb2 (34, 35). It is also involved in copper/zinc uptake and might regulate the activity of antioxidant enzyme Cu/Zn superoxide dismutase (SOD-1) and offers resistance to oxidative stress (34,35). It aids in neuroprotection by interacting with stress-inducible protein 1 and also has anti-apoptosis activity by preventing Bax induced apoptosis. However, PrP^C seem to be Bax specific as it do not avert Bak, t-Bid or staurosporine induced neuronal apoptosis. PrP^C also help in neuronal survival, neurite extension and is also believed to play role in synaptic structure and function maintenance (34-37). Recently, PrP^C is linked to the production of amyloid-β peptide and Alzheimer progression and also in cancer development due to its ability to modulate apoptosis and cellular proliferation (36,37).

To better understand the physiological role of PrP^C different *Prnp* knockout mouse strains have been generated but, there development and phenotypes are controversial and do not provide any conclusive result. The first *Prnp* ablated mouse made by the Weismann group did not display significant difference compared to normal mouse (24). However, the other *Prnp* knockout strains generated later e.g. Ngsk and Rcm0 developed the progressive ataxia and an extensive degeneration of Purkinje cells. And thus, the requirement of PrP^C in maintaining cerebellar homeostasis was concluded (38,39). These observations were in contrast to other mouse *Prnp* deleted strains Zrch-I and Edbg that did not exhibit signs of cerebellar dysfunction. The contradiction was solved by identification of a novel gene *Prnd* situated 16 kilobases downstream of *Prnp* and encode for PrP-like protein named Doppel or Dpl (40). In the Ngsk and Rcm0 engineered mouse *Prnd* came under transcriptional control of *Prnp* promoter and lead to the increased expression of Dpl that is usually expressed in very low amounts. Dpl has neurotoxic properties and it is suggested that PrP^C and Dpl might compete for a conjectural common receptor and PrP^C act by blocking the action of Dpl (40,41).

1.4 The prion protein family

The PRN gene family contains mainly three members, PRNP, PRND, and SPRN and also a fourth hypothetical novel gene PRNT. The paralogs of PRNP synthesize proteins that have similar amino acid sequence and similar tertiary fold (42,43). PRND is the first prion-like gene discovered in PRN gene locus at chromosome 20, 27 kilobases downstream from PRNP (39). It codes for Doppel protein that is mainly expressed in testis and is important for the functioning of male reproductive system. The nascent protein is of 179 residues and is subjected to similar post-translational modifications like PrP^C and the mature protein is

targeting to lipid rafts. Dpl shares 25% sequence identity with PrP^C C-terminus structured domain but they are reported to be present in distinct raft domains (42,43). Moreover, Dpl has an additional disulfide bond that restricts its conformational and structural flexibility. SPRN encodes for Shadoo/Sho protein. SPRN is not located in PRN gene locus and is present on chromosome 10 in humans. Like PRNP, SPRN is also highly conserved in nature as it has been found in distantly related organisms like, from zebra fish to rodents and primates (42). Sho also undergoes the similar processing like PrP^C and Dpl and mature protein consist of ~98 residues. Sho expression is confined to brain and it has mRNA binding sites and is believed to play role in neuronal signaling and in maintaining neuronal plasticity like PrP^C (44). PRNT is located in the PRN genomic locus ~ 3 kilobases downstream of PRND. It is predicted to have 94 residues and is found only in primates. Like Dpl, its expression is also restricted to testis (42).

1.5 The pathogenic mutations and polymorphism in PrP^C

Prion diseases can be caused by genetic factors. Mutations in the PRNP gene can occur in form of single point changes, truncation, insertions or deletions in the octarepeat region and silent mutations. Around 30 point mutations are recognized in the PrP^C that lead to inherited prion diseases (Figure 1.2). These mutations are known to either directly alter the structural stability and dynamics of the protein or act by manipulating the cellular interactions or processing of PrP thereby increasing the risk of developing prion pathogenesis. M/V129 and E/K 219 represent the most common polymorphisms in human PrP and are associated with early onset and variable phenotype of disease (29,45).

Salt-bridge interactions often play a crucial role in maintaining the tertiary structure of protein. Six mutations have been mapped to globular domain of PrP that influence salt-bridge interactions: R148H, D178N, E196K, E200K, R208H and E211Q. D178N is involved in various disease phenotypes and is the most comprehensively studied. It causes FFI with M129 and familial CJD (fCJD) with V129. Moreover, D178N mutation is hypothesized to decrease the PrP^{Sc} conversion barrier as it significantly increases the aggregation propensity of the mutant protein. E200K mutation is responsible for fCJD. Although, E200 forms salt-bridge with K204 but it is not structurally important and the disease is caused by altering the

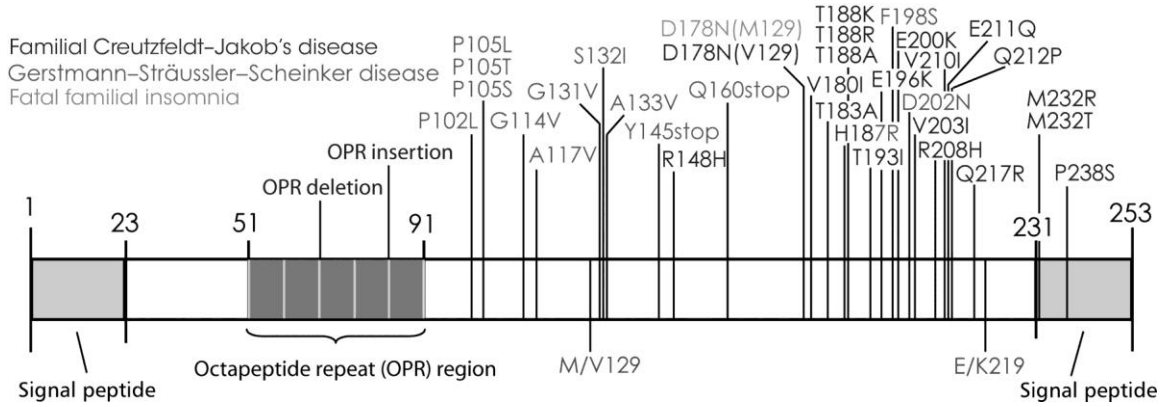

Figure 1.2 An outline of the pathogenic mutations in the cellular human prion protein. The predominant mutations are shown in gray. Reproduced with permission from reference 45.

overall surface electrostatic potential of PrP that might be important for interaction with other molecules (45).

GSS is caused mainly by four missense point mutations: P102L, P105/L/T/S, G114V and A117V. All these mutations are located in the flexible N-terminus and suggest the participation of N-terminus in the conversion process. This idea is supported by the protease-resistant and neurotoxic properties of aggregates form from peptide 106-126. Certain mutations that showed no substantial effects on globular structure by simulation or *in vitro* experiments at molecular level might have structural effects under altered environmental conditions by interactions with other cellular molecules. For example, P105L, A117V and P102L mutations does not affect the fibrillization ability. Experimental and simulation studies revealed that P102L does not disturb the thermodynamic stability of recombinant Syrian hamster PrP 90-231. But, CD data on the corresponding mutant of mouse PrP exhibited the decrease in α-helicity and the cellular PrP with P105L and A117V mutation has been found to display altered membrane topology (45).

Likewise, there are several other polar residue pathogenic mutations that might act by interfering with other stabilizing interactions. T183A, H187R and T188R/K are located in helix 2 and D202N, Q212P and Q217R are in helix 3. T183A mutation causes atypical glycosylation and Q217R lacks the GPI-anchor that causes defective trafficking. Similarly, two stop mutations have been identified: Y145stop and Q160stop, which lead to diseased condition by impaired trafficking. Few other mutations (M232R/T, P238S) are mapped to GPI-signal peptide are linked with fCJD. There are several other mutations (G114V, S132I,

A133V, T193I) that are found in some cases of genetic prion diseases but their mode of action is not known (45).

1.6 Structural biology of PrP^{Sc}

PrP exists in two alternative isoforms, PrP^{C} and PrP^{Sc}. Both isoforms have the same primary sequence of amino acids and can be distinguished on the basis of structural composition and other chemical and physical properties. PrP^{Sc} formed by the conformational conversion of PrP^{C} displays several unique features e.g. prions exist in different phenotypic forms termed as strains that self replicates and propagates themselves by imposing their conformation on substrate protein (PrP^{C}) (1). In 1994, Wickner broadened the prion concept to explain the epigenetic inheritance in yeast and other fungi in terms of self-propagating proteinaceous units (46). This finding also supported the protein-only hypothesis. The prerequisite for a protein entity to act as prion is that they must self-propagate by replication in the pool of the substrate protein in the new host (47). Further research in this direction has extended the prion phenomenon and revealed that numerous other proteins can also exist in aggregated state that cause diseases in humans and display a few prion attributes, if not all (48,49). The replication of PrP^{Sc} is not clear and different models have been proposed. Our knowledge about molecular basis of prion replication is limited as the atomic resolution structure of PrP^{Sc} is not yet discovered. Determining its structure holds the key to elucidate various bizarre facets of prions just like solving the DNA structure facilitated our comprehension about DNA replication and transcription (50). Despite of the prolonged interest in understanding the molecular integrity of PrP^{Sc} very little information is available. The proteinase K (PK) digestion is usually used to isolate PrP^{Sc} from diseased brain tissues in form of prion rods. PK treatment leads to the digestion of first ~ 89 residues and result in the generation of PK-resistant amyloid core termed as PrP 27-30, depending upon the empirical size of the monomer in western blots, that preserves the infectivity (1). Fiber diffraction experiments have demonstrated the generic predisposition of structurally or evolutionary distant protein aggregates to ordered cross β-sheet structure categorized as amyloid where parallel β strands are arranged perpendicular to the fibril growth axis (51). The low-resolution X-ray fiber diffraction pattern of PrP 27-30 revealed the meridional reflection at ~ 4.7 Å, typical of cross-β amyloid architecture and a weak and broad equatorial signal at 8 Å whereas typical amyloids are characterized by a sharp equatorial reflection at 10 Å (52). These amyloid structures also show characteristic staining by aromatic dyes, Congo red and Thioflavin T and S (53). This implies that PrP^{Sc} structure is composed of amyloid

characteristic cross- β core but there exist significant variations compared to other amyloids (52). Like other amyloids, the high-resolution structural studies based on X-ray crystallography and nuclear magnetic resonance (NMR) are hampered by the insolubility, non-crystalline and heterogeneous nature of PrP^{Sc} (30). The conventional low-resolution optical spectroscopic (circular dichroism (CD) and Fourier-transform infrared (FTIR)) analysis revealed that the conversion to peculiar infectious isoform (PrP^{Sc}) involves a substantial increase in β-sheet content. The FTIR studies indicated that PrP^{Sc} has 43% β-sheet and 42% α-helix, in contrary PrP^{C} holds 3% β-sheet and 42% α-helix (54,55). Various experiments using CD, NMR and molecular dynamics (MD) simulations have exposed that the N-terminus unstructured region particularly residues 106-126 and 89-143 are highly unstable and form β-sheet aggregates (56,57). The sharp decrease in α-helix content and PK resistant nature of C-terminal core indicates the changes in globular C-terminus. But, the C-terminus β-sheet constitution in PrP^{Sc} is highly debated. The biochemical analysis based on antibody mapping and binding of anti-prion compounds like tetracycline indicates the involvement of helix 2 in β-sheet formation (58). The structural studies of PrP^{Sc} are obscured by the presence of GPI anchor and complex glycans (30). Nevertheless, the unglycosylated and anchorless scrapie fibrils isolated from scrapie-infected transgenic mice expressing GPI-less PrP^{C} exhibit the similar FTIR analysis (spectral peaks between 1615 and 1636 cm^{-1}) as wild-type PrP^{Sc} which suggests that absence/presence of glycosylation and GPI anchor do not impose any change in PrP^{Sc} structure (49). Considerable efforts have been made to predict the PrP^{Sc} structure. On the basis of different biophysical techniques such as electron crystallography, hydrogen-deuterium exchange coupled to NMR and electron paramagnetic resonance (EPR) and MD simulations several structural models have been put forward but none of these models satisfy all the experimental data (59) (Figure 1.3).

The first high resolution structure of was obtained from electron crystallography analysis of two-dimensional (2D) crystals of PrP 27-30 with p3 symmetry (hexagonal lattice) (60) (Figure 1.3a). The 2D crystals were observed in the preparation of prion rods with high infectivity titer using electron microscopy. The image analysis and projection maps yielded ~ 7 Å resolution structural data. For reconstructing the model the structural constraints were based on the monomer dimensions, mutational analysis of miniprion (PrP^{Sc}106 (Δ23-88, Δ141-176)) and the position of sugars. The miniprion and PrP^{Sc} were found to crystallize in isomorphous 2D crystals. Parallel β-helical fold was proposed as the main structural element of PrP^{Sc} with the N-linked glycans pointing above and below the plane and α-helices arranged on periphery (60). The parallel β-helices model was further extended to frame trimeric or

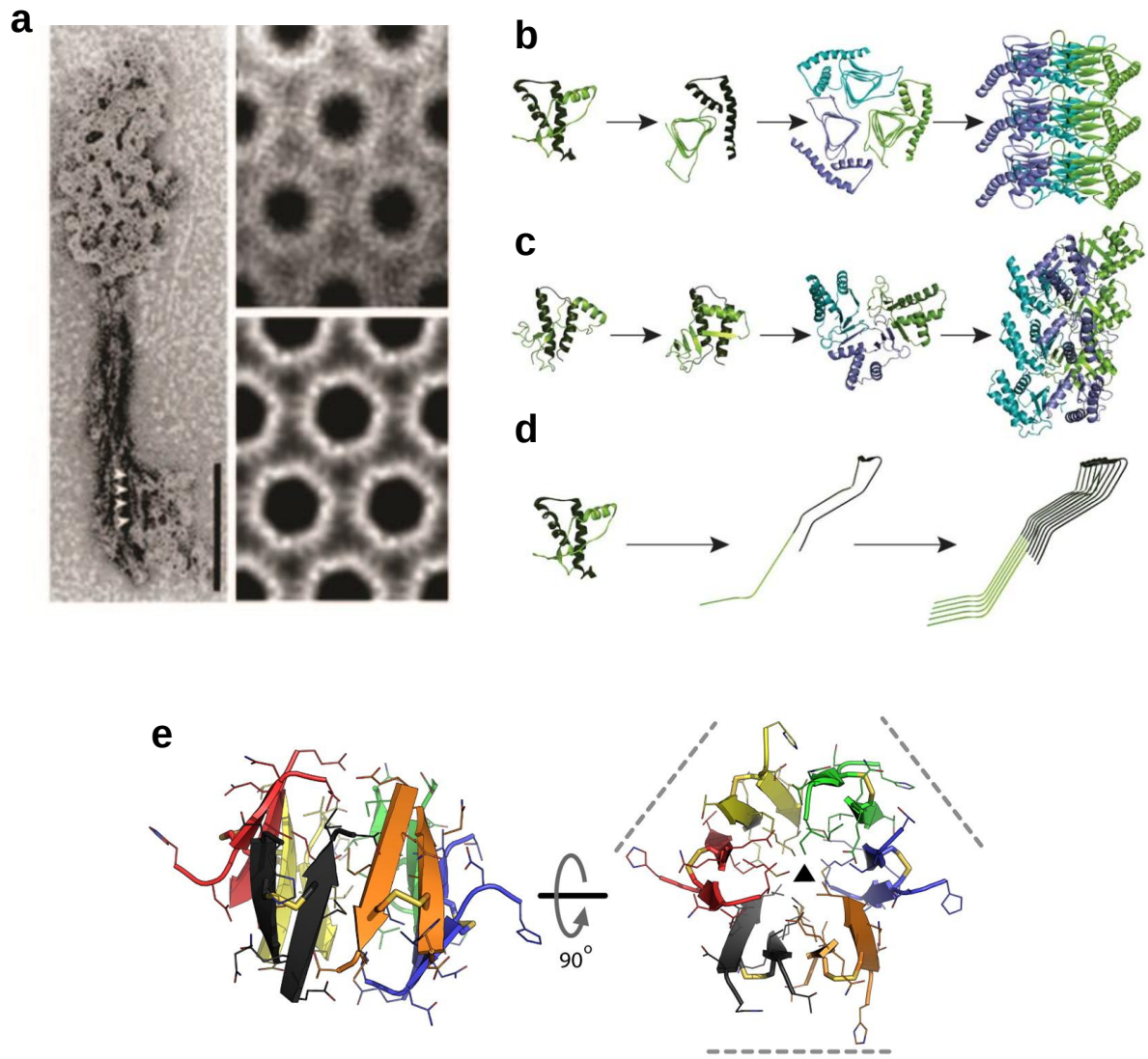

Figure 1.3 Structural models for PrP^{Sc}. (a) Hexagonal two-dimensional crystals of PrP 27-30. The left panel shows the prion rod with crystals at both the ends. Scale bar: 100 nm. Adapted from reference 60; Copyright 2007 National Academy of Sciences, U.S.A. (b), (c) and (d) represent the β-helical model, the spiral model and the parallel, in-register β-sheet model, respectively. Reproduced with permission from reference 50. (e) The hexameric oligomer structure of PrP fragment. Adapted from reference 67; Copyright 2013 American Chemical Society.

parallel left-handed β-helical model (61) (Figure 1.3b). The trimeric model was proposed by threading the N-terminus disordered region and helix 1 (~ 90-175) through a known β-helical fold. In this model the left-handed β-helices stacked horizontally forming triangular rungs

represent the fundamental symmetrical unit. There are six residues in each side of the triangular rung. The growth of aggregate occurs by vertical stacking of trimeric disks. Thus, the major conformational transformation occurs between residues 89 and 170 and the helix 2 and 3 are conserved. According to electron microscopy results of PrP 27-30 2D crystals fit to the unit cell with a dimension of 69 X 69 Å, but the in trimeric model the protofibrils have minimum and maximum diameter of 68 and 90 Å, excluding sugars and it did not fit to the unit cell (61,62). Interestingly, the HET-s prion from filamentous fungi *Podospora anserina* has been shown to form a left-handed solenoid which is structurally analogous to left-handed β-helical model (63).

Another model, the β-spiral model has been proposed on the basis of MD and docking procedures of hydrophobic patches to simulate the conversion process and structural modeling (64) (Figure 1.3c). The starting point of the model is recombinant Syrian hamster PrP comprising residues 109-219 and is based on the MD simulations of the conformational changes occurring under the low pH aggregating conditions. There are total four short β-strands. Residues 135-140 make an isolated β-strand. Amyloid β-core is made up of three short β-strands comprising residues 116-119, 129-132 and 160-164 that are stacked in a spiral like manner. Each trimeric oligomeric unit allows growth in either direction along fiber axis and larger aggregates are formed via hydrophobic packing and hydrogen bonding across intermolecular β-sheets with a 3_1 axis of symmetry. The protofibrils have minimum and maximum diameter of 58 and 67 Å, excluding sugars and the model is in agreement with the unit cell. The spiral model conserves all three α-helices of PrP^{C} which is inconsistent with PK-resistance and HX-MS data (62,64).

An alternative, the extended parallel in-register β-sheet model has been proposed on the basis of hydrogen-deuterium exchange studies and distance information by site-directed spin labeling combined with EPR (65) (Figure 1.3d). According to this model the conversion process involves the conformational change and refolding of the entire protein with the β-sheet core is composed of C-terminal region encompassing residues ~ 160 to 220 that correspond mainly to helix 2 and 3. Based on the analysis of inter-residue distance from spin labeling studies the model suggests that in PrP^{Sc} the core is composed of β-sheets stacked parallel forming an in-register alignment of β-sheet permitting unhindered growth of fibrils with relatively short turns and/or loops and no α-helices. This model is consistent with the proteolysis data. But, since fibrils obtained from recombinant PrP were used for the structural determination, it not clear to what extent they resembles the PrP^{Sc}. Besides, line of experiments using atomic force microscopy, X-ray fiber diffraction and hydrogen exchange

have revealed the significant differences in the cross- β structure of recombinant PrP fibrils and brain derived scrapie PrP (52). Moreover, parallel in-register β-sheet model is shared by several yeast prions such as Ure2p, Rnq1 and Sup35 and also appear as the common structural motif in other amyloid aggregates of amyloid β, α-synuclein and tau (50).

Thus, all three different structural models are based on low-resolution data and provided the divergent structural interpretations. It is notable; Eisenberg group has made a breakthrough development by obtaining the first high-resolution X-ray diffraction data on micro crystals of short amyloid fibrils formed from amyloidogenic peptides of yeast and mammalian prion protein (66). These amyloid fibrils composed of short stretches of β-sheets display a unique dehydrated steric-zipper arrangement where adjacent β-sheets are stabilized by tight interdigitation of side chains. However, similar crystallographic studies are not yet possible for larger polypeptides. Recently, X-ray crystallography has been applied to study oligomer structure derived from human PrP fragment (residues 177–182 and 211–216) corresponding to helix 2 and helix 3 covalently joined by disulfide bond. The crystal structure revealed the unique structural organization of these oligomers. Instead of forming the steric-zipper assembly, this fragment formed β-rich hexameric oligomers with three four-stranded anti-parallel β-sheets were arranged in a prismatic assembly forming the faces of a triangular prism (67) (Figure 1.3e).

1.7 Biosynthesis of PrP^C

The biosynthetic route of PrP^C is similar to typical secreted or membrane proteins. PrP^C is synthesized as 254 amino acids polypeptide chain on rough endoplasmic reticulum (ER) and resides on the outer cell membrane in the lipid rafts (1,6) (Figure 1.1a, 1.4). Following the synthesis, the N-terminal signal peptide translocates PrP in the ER where nascent protein is bestowed with several posttranslational modifications such as cleavage of N-terminal signal peptide and C-terminal hydrophobic segment with the attachment of GPI anchor, formation of disulfide bond and N-linked glycosylation at two sites (68,69). The core of PrP-GPI anchor is distinguished by the addition of sialic acid and it is sensitive to cleavage by phosphatidylinositol-specific phospholipase C (PIPLC) which attacks the diacyl glycerol (69). The folding of immature PrP is facilitated by its association with cholesterol-rich lipid rafts as cholesterol act as lipochaperone in the ER and its depletion commences the misfolding process. Various ER resident chaperones e.g. BiP and calnexin are also believed to assist in PrP folding. The PrP mutants linked to genetic prion disorders display alerted biochemical features as early as in the ER. Thus, ER might be involved in prion formation

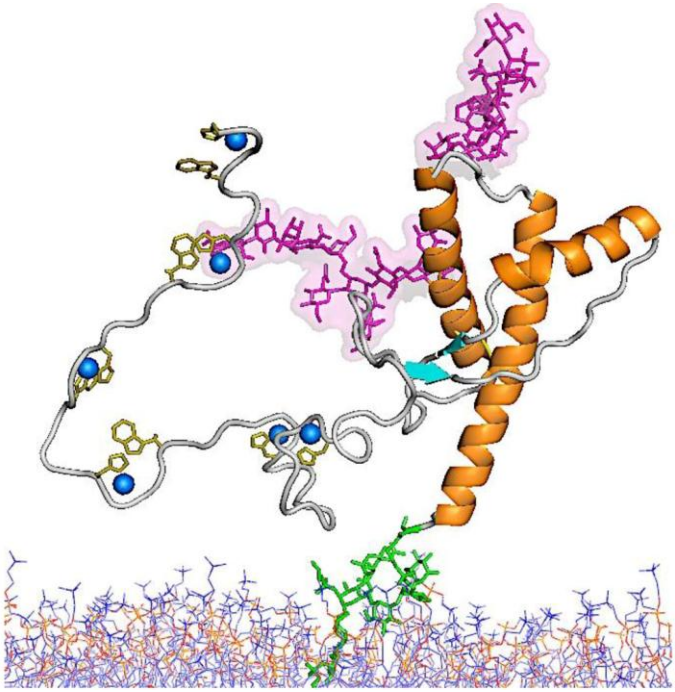

Figure 1.4 Schematic structure of the mature PrP^C anchored to the membrane with the GPI-anchor (shown in green). Glycans on N181 and N197 are shown in form sticks (pink). The copper ions bound to octarepeats are depicted in blue. Reproduced with permission from reference 59.

and might act as an amplification compartment. The accurately folded PrP molecules are then transported to Golgi for further processing and maturation of the N-linked glycans making them resistant to endoglycosidase H, before their transit to cell surface (69-74). Glycans are supposed to confer structural stability and PrP with mutated glycosylation sites demonstrated diseased phenotypes. Surprisingly, glycosylation is not invariably necessary as unglycosylated or monoglycosylated wild-type PrP^C is also detected at the cell membrane. Moreover, different prion strains exhibit variable glycoform patterns (75). Mature PrP^C, as a part of its usual metabolism, undergoes two cleavages, although, its biological relevance is vague. First cleavage occurs within its GPI-anchor at the cell surface releasing PrP in the extracellular milieu. Another, cleavage happens in the highly conserved region (His-111 or Met-112) in the endocytic acidic compartments (73,76).

1.8 Role of lipid rafts in prion biology

The exact localization of PrP in the neurons and other cells remains uncertain. However, PrP^C is insoluble in cold non-ionic detergent and co-purifies with detergent insoluble membrane microdomains (DIM) rich in cholesterol and sphingolipids which is sensitive to temperature, and indicates that PrP^C is clustered in rafts (70,71). Unlike other GPI-anchored proteins, PrP^C has three raft-localization signals and it is not solely dependent on its GPI-anchor. The N-terminal disordered ectodomain and sphingolipid-binding domain in the C-terminus play an important role in mediating the raft-association (77,78). The current findings propose very contradictory role of rafts in prion biology, being both protective and destructive. Rafts association is suggested to stabilize the native PrP conformation by proper folding. Whereas, numerous parasites and pathogens exploit lipid rafts to pierce in the host cells. Since, PrP^C and PrP^{Sc} are found in rafts; prions might also hijack rafts and use them as their entry site for replication by conversion of PrP^C (70,71)

1.9 Internalization of PrP^C

PrP^C at the cell surface is rapidly endocytosed and a part of it is recycled back to the surface (73) (Figure 1.5). But, the mechanism and role of PrP internalization is largely unknown. Both, clathrin-mediated and caveolae-dependent mechanisms have been hypothesized for PrP^C internalization (70,71). PrP^C has been shown to endocytose via clathrin-dependent pathway and constitutively cycle through the cell with a transit time of approximately 60 min (79). It might get degraded through the endosomal-lysosomal pathway or transferred back to cell membrane via recycling endosomes (79). The N-terminal segment of the PrP is essential for its localization in clathrin-coated pits and internalization (80). Being a GPI-anchored raft-localized protein, it lacks cytoplasmic tail to interact with adaptor proteins and is believed to interact with a transmembrane putative PrP^C-receptor (like laminin receptor) through its N-terminal portion (73). Moreover, incubation of cells in hypertonic sucrose and expression of dominant negative mutant of dynamin I (K44A) inhibits the clathrin-mediated endocytosis (81). Experiments in other cell types (e.g. Chinese hamster ovary cells and primary hippocampal neurons) indicated that PrP was absent in clathrin-coated pits and internalization occurs through caveolae-dependent pathway (82). The N-terminal region of PrP has conserved octapeptide repeats that are known to bind copper and is believed to regulate copper/zinc homeostasis. Also, copper ions have been shown to induce the PrP^C-endocytosis in neuronal cells through clathrin-mediated pathway. But, it is not certain whether this

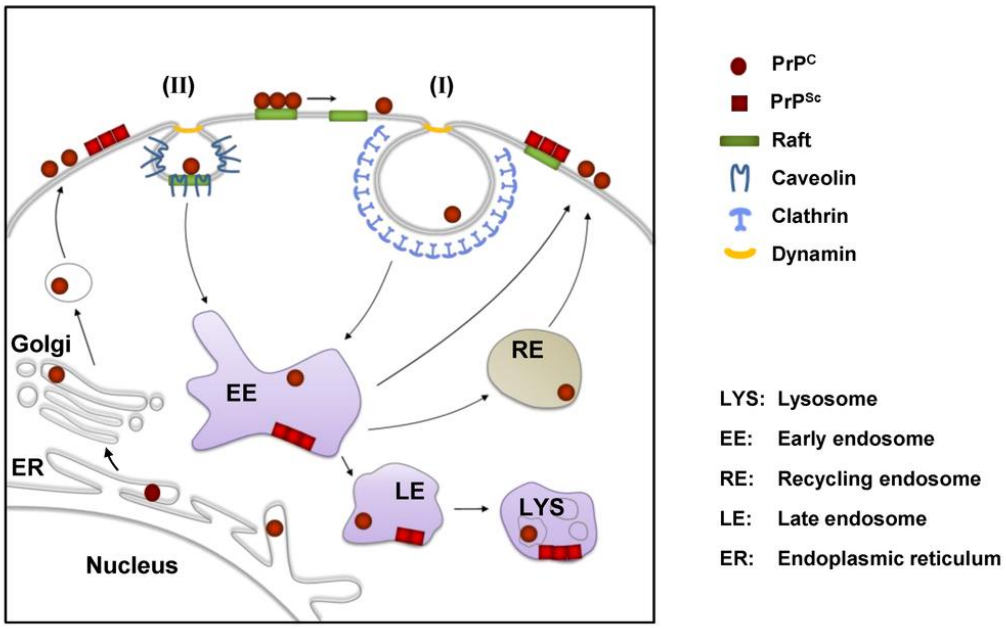

Figure 1.5 Cell biology of PrP^{C}. PrP^{C} is synthesized in ER. The post-translationally modified and properly folded PrP^{C} traffics through Golgi and secretory pathway and is translocated to the lipid rafts on the cell surface. PrP^{C} can be endocytosed *via* clathrin-dependent process or it can be internalized in caveolae-dependent manner. The internalized PrP^{C} is either recycled back to the cell surface or it is degraded in lysosomes. Interaction of PrP^{C} with PrP^{Sc} can occur either on the cell surface or in the endo-lysosomal organelles. Reproduced with permission from reference 86.

endocytic mechanism is similar to the constitutive internalization process of PrP (83). However, other reports demonstrated that in neuronal cells PrP^{C} first translocates out of the raft before its endocytosis through the clathrin machinery (71). Taken together, different studies suggest that the PrP^{C} endocytosis is a flexible and complex process and there might be various internalization routes in different cell types. The familial disease related pathogenic mutants of PrP e.g. P101L, D177N, Q217R, Y145stop, E199K demonstrate aberrant trafficking to cell surface, impaired sub-cellular localization and display various biochemical properties similar to scrapie isoforms including PIPLC and protease resistance and detergent insolubility (84,85). The mutant isoforms start misfolding in the ER and acquire PIPLC resistance as early as in the ER (73). However, very little is known about the sub-cellular localization and trafficking of mutants (86). We have begin to investigate various aspects related to the endocytosis of wild type PrP^{C} and mutants involved in genetic prion disorders (chapter 4).

1.10 Alternative transmembrane topologies of PrP

Though PrP^{C} is typically tethered to the cell surface by its GPI-anchor, alternate transmembrane forms have also been found depending upon its anchoring to the cell membrane that depends upon its synthesis and translocation through Sec61 translocation channel in the ER. Due to the inefficient translocation of central hydrophobic domain (amino acids 110-135) of PrP through the Sec61 channel, it can occur in different topologies viz. ^{Ntm}PrP where N-terminus resides in the ER and C-terminus in the cytosol, ^{Ctm}PrP where N-terminus is cytosolic and cytosolic PrP (cyPrP) which is released in the cytosol due to failed translocation. Mutations in the hydrophobic domain lead to increased formation of ^{Ctm}PrP. However, the neurodegeneration caused by ^{Ctm}PrP is not similar to scrapie PrP and thus, not transmissible (68,87).

1.11 Role of ER and endocytic pathway and other ligand molecules in formation of PrP^{Sc}

The cellular organelles involved in the transconformation ($PrP^{C} \rightarrow PrP^{Sc}$) and generation of scrapie isoform are still elusive. PrP^{Sc} has been found to localize in lipid rafts and endocytic compartments. A growing body of evidence proposes the role of endocytic pathway in the conversion of PrP^{C} to PrP^{Sc}. The N-terminus of PrP^{Sc} is proteolytically cleaved in the acidic compartments instantly after its generation and is found to accumulate in the late endosomes. PrP^{Sc} formation is not dependent on cell surface recycling and it is substantially increased by dominant-negative mutants of small GTPase Rab4 and Rab6. Moreover, it indicates the role of early endosomes and retrograde trafficking to the ER and Golgi in the amplification of PrP^{Sc} by disquieting the synthesis of PrP^{C} (88). The proteasome machinery might be involved in the degradation of mutant or misfolded PrP (85,89). The role of ER chaperones is also not understood well. They might bind and stabilize the partially folded forms making them more toxic (69). PrP^{C} is also known to interact with various accessory molecules like polyanions, nucleic acids, glycosaminoglycans (GAG), heparan sulphate proteoglycan (HSPG) that promote the generation of PrP^{Sc}. Laminin receptor and its precursor (LRP/LR) have been shown to participate in the uptake of PrP^{Sc} and prion pathogenesis (90). Moreover, PrP^{Sc} positive endosomal/lysosomal organelles undergo exocytic fusion in form of exosomes, thereby releasing the infectious particles into the extracellular medium and thus play an important role in dissemination of prions from cell to cell (91). Prions are now also believed to transmit to the neighboring cells by means of tunneling nanotubes, a recently described

mechanism of cell-to-cell communication (92,93). These are membranous structures that bridges cells and mediate the transport of cytoplasmic molecules, membrane components and organelles (92,93).

After conversion to scrapie isoform, it can accumulate intracellularly in the cytoplasm, organelles or cell membrane or extracellularly as amyloid plaques. However, the light microscopy visualization of PrP^{Sc} from diseased host is characterized by diffused granular punctate structures that do not resemble amyloid fibrils (94). The difference between the scrapie aggregates and amyloid fibrils (prion rods) obtained after membrane detergent extraction is not yet clear. Thus, the misfolding of PrP is quite complex and heterogeneous and produces diverse aggregates like large plaques, amyloid fibrils and amyloid incompetent oligomers. However, the relationship of these misfolded forms with the disease is not yet clear (49). The current research on the neurodegenerative diseases caused by protein misfolding postulates that oligomers as the prime pathogenic species (95). In order to decipher the relative relationship between PrP^{Sc} infectivity and size different experiments based on field-flow fractionation that partially disaggregate PrP^{Sc} and fractionate them by size and sedimentation velocity of the detergent solubilized PrP^{Sc} have been performed (96,97). These experiments revealed that infectivity properties are associated with the size of scrapie isoform. The oligomeric species and/or low density aggregates with 17-27 nm diameter and 300-600 kDa molecular mass displayed marked infectivity and conversion activity. In comparison, these activities were considerably low in large fibrils and almost null in oligomers constituted by $\leq$5 PrP monomers. These studies indicate that the non-fibrillar population made up of 14-28 PrP molecules are the most infectious particles (96). Besides, the size of the infectious unit is subjected to strain differences which might also determine the replication dynamics and strain-specific biological phenotypes (97). Though, recently larger scrapie aggregates are shown to replicate and propagate better *in vivo* (98).

1.12 *In vitro* approaches to elucidate the $PrP^{C} \rightarrow PrP^{Sc}$ conformational transition

Formulating the PrP transconversion process under *in vitro* designed conditions provide several advantages to characterize chemical and physical properties of PrP^{C} and PrP^{Sc} and the steps involved in the formation of PK resistant scrapie isoform (PrPres). *In vitro* conformational conversion can be induced chemically by changing solvent conditions such as at low pH or at low concentrations of denaturing agents (urea, guanidium chloride, ionic detergents) and different salts or by subjecting to physical changes (high pressure and high temperature) (30). The quantitative analysis of unfolding of the structured domain of

recombinant PrP (121-231) at varying concentrations of urea revealed that it follows one co-operative denaturation transition at neutral pH. And, the reversibility of the denaturation process highlighted that the α-helical native monomeric state is of the lowest free energy. Whereas, at low pH (4.0), the appearance of an intermediate stage with increased ellipticity at 218 nm was recognized (99). Further work, showed that the low pH β-conformer has an inherent tendency to aggregate which represented the most stable state. Moreover, under acidic pH and mild denaturing agents, recombinant PrP adopted an oligomeric β-sheet structure that matured into PrP^{Sc}-like amyloid conformation. These studies established that the folding of PrP into its α-helical conformation is kinetically driven and the β-sheet-rich isoform is the most thermodynamically stable state (100). However, a different study based on disulfide bond reduction at acidic pH demonstrated the formation of monomeric β-rich state. Subsequent experiments using a reduction-oxidation process converted native recombinant PrP into oligomers with characteristic of PrP^{Sc} and lead to the generation of three dimensional dimeric domain swapped model with intermolecular disulfide bonds. Interestingly, these oligomers for the first time also depicted the autocatalytic seeded conversion ability (101). Nevertheless, the relevance of these studies is not established as PrP^{C} to PrP^{Sc} conversion preserves the intramolecular disulfide bridge and other experiments do not support the transient opening of disulfide bond (30). Different *in vitro* studies has also demonstrated the formation of amyloid fibrils under native non-reducing conditions and also in the absence of denaturing agents at low pH in the acetate buffer (102). In the different batch of experiments, a low concentration of sodium dodecyl sulfate (SDS) was used to induce the conformational conversion at the neutral pH (103,104). The low concentration of SDS mimic the membrane-environment, this conversion system is regarded the closest to the natural conditions. Initially, using high concentration of SDS (0.3%) the natural PrP27-30 was converted into an α-helical, non-infectious thermodynamically stable dimer. At lower concentrations of SDS the α-helical dimer co-operatively assembles into a β-rich oligomeric state. This conversion system has been applied to recombinant PrP fragment 90-231, that also showed the similar behavior. These β-rich oligomers consisted of 12-16 PrP molecules are highly soluble and stable in solution. But, low concentration of SDS with salt (250 mM sodium chloride) leads to fibril formation (105). In the chapter 2, we have investigated the crucial role of salt in the fibrillization process and key intermediates involved. However, infectivity could not be established using the *in vitro* generated PK-resistant amyloid fibrils.

In one of the first efforts, Prusiner group generated the synthetic prions from recombinant PrP which could manifest prion-like symptoms when injected into transgenic mice over-

expressing N-terminally truncated PrP^{C} (106). However, TSE symptoms were noticed after a very long incubation periods. This raised a specific issue as the transgenic mice could also spontaneously develop the disease during the long incubation time. Subsequent experiments reveled that synthetic prions could be propagated to wild-type mice after passaging several times in transgenic mice (107). Further, Baskakov also demonstrated the infectious properties of recombinant prions after passaging it twice in wild-type mice (108). Although, in these seminal studies recombinant/synthetic prions did not display direct infectivity. However, they displayed the physicochemical attributes of PrP^{Sc}. The *in vitro* conversion studies have proved very beneficial in dissecting the key alterations occurring in the native PrP structure at different stages of the conversion reaction. The information gathered from these studies indicated that $PrP^{C} \rightarrow PrP^{Sc}$ transition is characterized by multi-steps. It starts with initial conformational changes in the native monomeric PrP that leads to formation of critical nucleus that further grows in size constituting higher-order oligomers, which polymerizes to form PK-resistant amyloid fibrils *via* nucleated conformational conversion mechanism (chapter 2).

In the cell-free conversion system prion replication is recapitulated using brain-derived PrP^{Sc} as template. The conversion was followed by using the ^{35}S-labelled PrP^{C} purified from cultured cells. PrP^{Sc} catalyzed the conversion of ^{35}S-PrP^{C} into highly protease-resistant PrP bound to the PrP^{Sc} seed (109). But cell-free system suffered from several drawbacks. For example, slower conversion rate, low concentration of newly converted product and inability to isolate it from the template used as inoculum that made it difficult to test the infectivity of *in vitro* generated PrP^{Sc} product (109).

Recently, an important advancement has been made in prion research with the development of protein misfolding cyclic amplification (PMCA) assay (110). PMCA is an innovative and highly sensitive method for *in vitro* efficient replication of prions. It indefinitely amplifies the infectious PrP^{Sc} using normal brain homogenate as PrP^{C} substrate mixed sub-stoichiometric PrP^{Sc} seed. The mixture is subjected to successive cycles of incubation with intermittent sonication. The incubation allows the seeded polymerization of substrate into PrP^{Sc} polymer whereas, sonication disintegrate the polymer to produce more seed. The product is serially diluted in normal brain homogenate followed by additional amplification cycles. The beauty of the cyclic conversion reaction is that the product displays the identical physicochemical and infectious properties as the seed. Moreover, the method is so efficient that during replication it conserves the strain-specific properties and thus, faithfully propagate the strain related variations like strain memory, species barrier and strain

adaptation (111,112). This strongly indicates that the prion strain properties are enciphered in the PrP^{Sc} structure and is not dependent on living cell for propagation. In addition, PMCA can spot as little as ~1 attogram of PrP^{Sc} and thus, also serves as an effective prion-diagnostic method (49).

The propagation of infectious PrP^{Sc} in cell-free *in vitro* environment by PMCA validated the protein-only hypothesis but the use of crude brain homogenate limited its use. Moreover, because of the complex composition of brain homogenate it is difficult to rule out the participation of other molecules in the conversion reaction. Further, substituting the brain homogenate with purified PrP^{C} did not show significant conversion efficiency. The only problem related with PMCA method is the use of sonication. Sonication is a non-physiological process. Sonication of proteins has been known to generate amyloid-like aggregates (113). The energy released during sonication may help in overcoming the energy barrier for scrapie formation.

1.12.1 Role of cofactors in PrP^{Sc} propagation

In an alternative procedure, Supattapone group verified the PMCA conversion efficiency in the absence of sonication. They found that sonication is not absolutely required for PrP^{Sc} generation from brain homogenate but it does accelerate the amplification process. They also demonstrated that the host specific RNA molecules highly exhilarate the conversion process (114). These results indicated that, besides PrP^{C}, the accessory molecules present in the crude brain homogenate are imperative for successful *in vitro* PrP^{Sc} formation. The PMCA technique was further improved by the use of purified PrP^{C} from healthy brain samples as substrate rather than brain homogenate. This was the first instance where scrapie infectivity was generated from pure compounds with the addition of synthetic polyanionic accessory molecules (nucleic acids, lipids and heparan sulfate proteoglycan) in the presence of PrP^{Sc} seed (115). As mentioned above sulfated glycans also act as PrP^{C} binding partners, co-purifies with PrP^{Sc} from diseased brain tissue and are hypothesized to act as receptors for PrP^{Sc} on the cell membrane. Later, Ma laboratory using PMCA technique reported the generation of infectious prions from recombinant PrP with the only addition of synthetic anionic lipid (1-palmitoyl-2-oleoyl-sn-glycero-3-phosphoglycerol (POPG)) and mouse-isolated total RNA (116). Further research from same group used the synthetic RNA in place of endogenous RNA and generated infectious prions that are sufficient to cause bona fide prion disease in wild-type mice (117).These experiments indicate that the specific accessory molecules termed as cofactors play a decisive role in de novo infectious prion formation.

1.12.2 Role of cofactor maintaining prion infectivity and strain properties

The discovery of cofactors is an important turning point in prion research. The exact characteristics of biomolecules that can act as cofactors are still obscure. The identity of cofactor molecule might vary in different species. Various studies have suggested species-dependent potency of cofactors. For example, the amplification of hamster and sheep PrP^{Sc} is highly dependent on RNA and the degradation of RNA eliminated the generation of prions (115,118). For hamster prion amplification GAGs could be used but the nucleic acids ~ 40 bases in length were found more efficient in triggering the amplification (119). Although, RNA specificity is not dependent on nucleotide sequence except polypurines, that do not support PMCA amplification (118). However, RNA is not required for propagation of mouse and prairie vole PrP^{Sc}. And, the cofactors for these species were believed to be partially proteinaceous owing to their sensitivity to proteases (120). However, recent reconstitution experiments based on nuclease-resistance, normal phase chromatography, phospholipase C digestion, ^{31}P NMR and mass spectrometry have identified a single promiscuous endogenous cofactor, phosphatidylethanolamine (PE) (121). Endogenous or even synthetic PE serves a solitary cofactor for prion formation and propagation from multiple species including hamster, mouse, vole and deer. PE is a more efficient cofactor than POPG + RNA as it yields higher conversion rate. Also, anionic phospholipids are incapable of prion formation if RNA is depleted (121). Thus, variety of molecules can act as cofactors, their identity and expression levels might vary in different types of neurons. And, different PrP^{Sc} strains prefer different cofactors for their efficient natural replication. This might also explain the observed variable scrapie susceptibility of different cell types and the distinct neurotropic pattern observed in prion diseases. The stochastic formation of PrP^{Sc} in presence of only cofactors and PrP^{C}, implicate that the cofactor molecules may play a vital role in sporadic generation of CJD prions (122-124).

A different batch of experiments deciphered the role of cofactors in prion infectivity. The withdrawal of cofactor PE during PMCA serial propagation resulted in change of PrP^{Sc} conformation confirmed by the ~2kDa shifted protease-resistant core. This "protein-only" conformation was not infectious but it preserved the autocatalytic activity and, on subsequent addition of PE it did not revert to the infectious cofactor-dependent conformation (125). It points that cofactor involvement is crucial for the infectivity of PrP^{Sc} conformers by maintaining PrP^{Sc} structure in a meta-stable form. The presence of cofactor strongly

influences the PrP^{Sc} conformation. For example, the use of single cofactor PE leads to the convergence of three different strains used as seed for serial PMCA (sPMCA) into a single novel strain. The observation was verified by strain-typing assays which revealed similar conformational stability and clinical symptoms (126). It is possible that diverse strain properties of mammalian prions might arise from their dependence on specific cofactor molecules.

As mentioned above PrP has a large interactome representing array of biomolecules that can potentially function as cofactors. Since, PrP^{C} is anchored to plasma membrane, the prion conversion cofactors are believed to be present on the cell surface and suggests the putative role of lipids in PrP transition. Experimental results further support this view; in the presence of anionic lipids (phosphatidylserine, phosphatidylinositol, and phosphatidylglycerol) PrP adopts a β-rich conformation (127). In the modified sPMCA and cell-free conversion assay, detergents like SDS have been used as an imperfect alternative for anionic lipids to stimulate the PrP conformational conversion to infectious prions (109). This suggests that SDS being similar to anionic lipids can act as a conversion enhancing cofactor.

1.12.3 Molecular mechanism of cofactor molecules induced prion propagation

The molecularly defined infectious prions are usually generated using anionic lipids (PG, PS) and RNA or PE. But, the mechanistic details of cofactor induced infectious prions replication remains elusive. Polyanionic cofactors like nucleotides might function by interacting with specific PrP sequence and might provide structural backbone for sustaining the infectious conformation. However, a study using photocleavable nucleotides revealed that hydrolyses of polyanions did not change the infectious properties of PrP^{Sc} (128). Thus, polyanionic cofactors including RNA might act during the conversion process but they are not involved in PrP^{Sc} structure. Lipids may influence the prion generation in the fundamentally different ways. PE and PG, both are efficient cofactors, but the physical properties of both lipids are very different. Thus the mode of action of cofactor molecules is very vague. These accessory factors might act at different steps in PrP conversion and combination of different cofactors might impart very unique propagation and infectivity properties on prions (123). According to "cofactor selection" hypothesis different prion strains require a specific set of cofactor molecules to efficiently propagate the strain properties (120). The cofactor molecules might act as catalytic scaffold, concentrating the PrP^{C} and PrP^{Sc} thereby bringing them close and would help in surmounting the energy barrier for conversion. They may also function either

by stabilizing the PrP^{Sc} conformation or by rendering PrP^{C} susceptible to conversion (50,129). Therefore, the molecular and the structural details of the cofactor action are not clear. Recently, a little progress has been made in this direction by applying DXMS to structurally dissect the formation of bona fide prions produced by using POPG + RNA cofactor PMCA system (130). The study provided insights into the conformational dynamics and structural rearrangement during prion generation. The subsequent addition of cofactors leads to progressive conformational changes resulting into insoluble PrP-POPG-RNA (PrP^{Int2}) complex, an on-pathway intermediate to the infectious PrP^{Sc} formation (Figure 1.6).

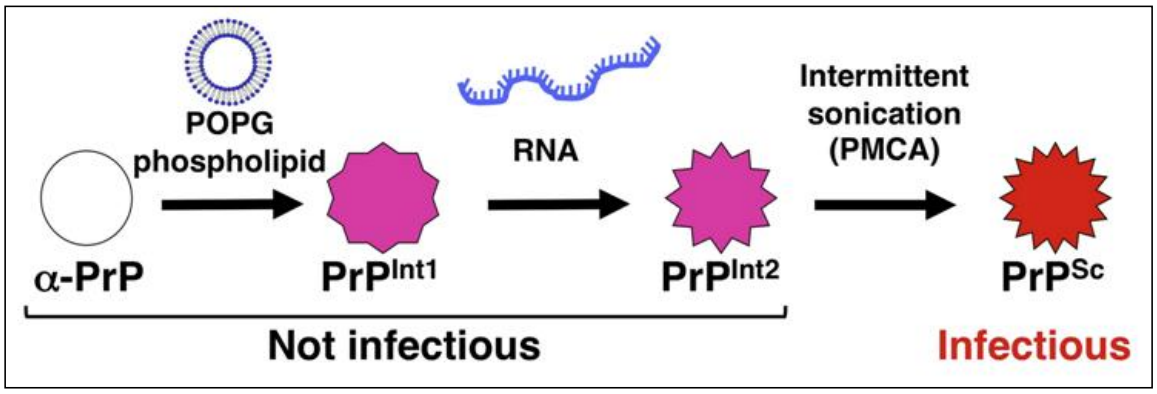

Figure 1.6 Schematic model of PrP transition into PrP^{Sc} through PMCA method by successive addition of POPG and RNA followed by intermittent sonication. Reproduced with permission from reference 130.

In the PrP^{Int2} complex major structural changes occur in all three helices, one β-sheet and N-terminus is highly exposed. The formation of infectious prions is accompanied with the global increase in solvent protection. The notable decreased solvent exposure is observed in the hydrophobic domain (111-126). The decreased exchange rate might be result of cofactor binding (lipid) to this region. The biologically active prions exhibit ~ 40 – 70% deuterium incorporation depending upon different prion strains. Thus, cofactors exert significant conformational influence on PrP^{Sc} structure and behavior (130). The infectivity and structural differences observed between *in vivo* and *in vitro* generated prions might also result from cofactor driven covalent modifications during PrP^{Sc} formation.

These observations certainly highlight the indispensable role of cofactor molecules for efficient propagation of prion strains and also in maintaining various strain characteristics. The detailed understanding of the criteria by which certain biomolecules are recruited to

function as cofactors and the molecular effects of cofactors on the secondary/tertiary structure of PrP during transition process and the cofactor induced packaging of PrP^{Sc} polymer is needed. Moreover, according to emerging consensus oligomers are accountable for neurodegeneration. But, PrP^{Sc} form recovered after PMCA has been found extremely pathogenic to the host. So, we need to comprehend the structural similarity between the much talked about toxic oligomers and pathogenic PrP^{Sc} generated using PMCA method.

1.13 Nanoimaging of prions beyond the diffraction limit

Prion strains represent the different types of self-propagating aggregated conformational states of the PrP^{Sc}. Prion strains demonstrate amyloid polymorphism and the cross-species transmission results in adjournment of pathogenesis. This phenomenon is called as species barrier. But, the successive passaging in the new host lead to strain adaptation which often result in conformational change in PrP^{Sc} and the decrease in disease onset time (1). Our knowledge about prion strains, species barrier and strain adaptation is very limited. Differences in the PrP primary structure might govern the inter-species transmission of the prions. And, the variable glycosylation patterns bestow the conformational diversity to mammalian prions (53). The presence of glycans might impose steric constraints that modulate the structural packing of PrP^{Sc} (131). These interesting issues could be addressed by single molecule imaging. Owing to the nanoscopic dimension, the structured protein aggregates cannot be imaged by diffraction-limited conventional light microscopy. Thus, there is a pressing need to develop new super-resolution imaging method that can be easily applied to amyloid fibrils. This would allow us to map the structural changes happening at the various stages of these processes. From this vantage point, we have adapted a scanning probe microscopy based super-resolution fluorescence imaging technique (near-field scanning fluorescence imaging) to study the amyloid framework (132). We speculate that this method can be successfully applied to study the features that distinguish different prion strains (chapter 5).

1.14 The fundamental role of water in PrP oligomerization and fibrillation

The sensitivity and destabilization of native PrP structure to temperature, pressure and pH purports the fundamental role of hydration in the misfolding and aggregation (133). The water molecules encapsulating the protein surface make up the hydration shell and termed as biological water (134). The nano-confined biological water in the vicinity of proteins plays an important role in guiding the protein-protein interactions (134,135). Interestingly, among all the soluble proteins in the PDB, PrP^{C} has the largest number of defectively wrapped backbone hydrogen bonds vulnerable to water interaction located in helix 1, helix 2-helix 3 loop, helix 3 C terminus (136). Thus, these are the structurally labile regions with a higher propensity of unfolding and aggregation. Moreover, molecular dynamics (MD) simulation analysis point out the pervasive nature of these sites for interaction with lipid membranes (137). Using solvent relaxation, we have investigated the hydration aspects of prion misfolding. We deciphered that amyloid-competent oligomers of PrP are structurally stabilized by the ordered water molecules. In our experiments, we observed approximately a nanosecond relaxation of confined interfacial water that means its motion is impeded by 3 orders of magnitude compared to the bulk water that relaxes in the time range between 100s of femtoseconds to picoseconds (chapter 3).

1.15 Thesis perspective

Prions are the only pathogenic misfolded protein that can be generated *in vitro* using molecularly defined constituents. A recently published report has suggested the possibility of iatrogenic transmission of Alzheimer's disease caused by the aggregation of amyloid β (138). This indicates that prion-like mechanism is much wide-spread in nature and may represent a ubiquitous feature of the neurodegenerative diseases caused by protein misfolding and aggregation. Thus, it is of significant interest to fully comprehend the molecular details of prion formation and various attributes related to prions such as amyloid polymorphism, strain adaptation, species-barrier and the high-resolution structural details of PrP^{Sc}. This thesis aims at uncovering the underlying biophysical mechanism of prion protein misfolding and amyloid formation under membrane-mimetic conditions and the fundamental structural role of the ordered water molecules in the formation amyloid-competent oligomers of PrP. In the last part of this thesis, I have discussed the super-resolution fluorescence nanoimaging methodology to look into the amyloid architecture using near-field scanning optical microscopy with the future aim to investigate the basis of prion strains and prions species

barrier. Taken together, I believe that the work embodied in this thesis will improve our understanding towards the intriguing mechanism of prion misfolding and aggregation.

1.16 References

1. Prusiner, S. B. (2004) *Prion biology and diseases*, Cold Spring Harbor Laboratory Press
2. Collinge, J. (2001) Prion diseases of humans and animals: their causes and molecular basis. *Annual review of neuroscience* **24**, 519-550
3. Aguzzi, A., Sigurdson, C., and Heikenwaelder, M. (2008) Molecular mechanisms of prion pathogenesis. *Annu. Rev. pathmechdis. Mech. Dis.* **3**, 11-40
4. Prusiner, S. B., and Hsiao, K. K. (1994) Human prion diseases. *Annals of neurology* **35**, 385-395
5. Budka, H., Aguzzi, A., Brown, P., Brucher, J. M., Bugiani, O., Gullotta, F., Haltia, M., Hauw, J. J., Ironside, J. W., and Jellinger, K. (1995) Neuropathological diagnostic criteria for Creutzfeldt-Jakob disease (CJD) and other human spongiform encephalopathies (Prion diseases). *Brain Pathology* **5**, 459-466
6. Prusiner, S. B. (1998) Prions. *Proc Natl Acad Sci U S A* **95**, 13363-13383
7. Chesebro, B. (2003) Introduction to the transmissible spongiform encephalopathies or prion diseases. *British medical bulletin* **66**, 1-20
8. Wells, G. A., and Wilesmith, J. W. (1995) The neuropathology and epidemiology of bovine spongiform encephalopathy. *Brain Pathology* **5**, 91-103
9. Cuille J., Chelle P.L. (1939) Experimental transmission of trembling to the goat. *C R Seances Acad Sci* **208**, 1058–1060
10. Gajdusek, D. C., and Zigas, V. (1957) Degenerative disease of the central nervous system in New Guinea: the endemic occurrence of kuru in the native population. *New England Journal of Medicine* **257**, 974-978
11. Gajdusek, D. C., Gibbs, C. J., and Alpers, M. (1966) Experimental transmission of a Kuru-like syndrome to chimpanzees. *Nature* **209**, 794-796
12. Ironside, J. W. (2003) The spectrum of safety: variant Creutzfeldt-Jakob disease in the United Kingdom. in *Seminars in hematology*, Elsevier
13. Bruce, M. E., Will, R., Ironside, J., McConnell, I., Drummond, D., Suttie, A., McCardle, L., Chree, A., Hope, J., and Birkett, C. (1997) Transmissions to mice indicate that 'new variant'CJD is caused by the BSE agent. *Nature* **389**, 498-501

14. Will, R. G., Ironside, J., Zeidler, M., Estibeiro, K., Cousens, S., Smith, P., Alperovitch, A., Poser, S., Pocchiari, M., and Hofman, A. (1996) A new variant of Creutzfeldt-Jakob disease in the UK. *The Lancet* **347**, 921-925
15. Pattison, I., and Millson, G. (1961) Scrapie produced experimentally in goats with special reference to the clinical syndrome. *Journal of Comparative Pathology and Therapeutics* **71**, 101-IN110
16. Collinge, J. (1999) Variant creutzfeldt-jakob disease. *The Lancet* **354**, 317-323
17. Hope, J. (1994) The nature of the scrapie agent: the evolution of the virino. *Annals of the New York Academy of Sciences* **724**, 282-289
18. Alper, T., and Cramp, W. (1967) Does the agent of scrapie replicate without nucleic acid? *Nature* **214**, 764-766
19. Prusiner, S. B. (1982) Novel proteinaceous infectious particles cause scrapie. *Science (New York, N.Y.)* **216**, 136-144
20. Bolton, D. C., McKinley, M. P., and Prusiner, S. B. (1982) Identification of a protein that purifies with the scrapie prion. *Science* **218**, 1309-1311
21. Oesch, B., Westaway, D., Wälchli, M., McKinley, M. P., Kent, S. B., Aebersold, R., Barry, R. A., Tempst, P., Teplow, D. B., and Hood, L. E. (1985) A cellular gene encodes scrapie PrP 27-30 protein. *Cell* **40**, 735-746
22. Basler, K., Oesch, B., Scott, M., Westaway, D., Wälchli, M., Groth, D., McKinley, M., Prusiner, S., and Weissmann, C. (1986) Scrapie and cellular PrP isoforms are encoded by the same chromosomal gene. *Cell* **46**, 417-428
23. Gabizon, R., McKinley, M. P., Groth, D., and Prusiner, S. B. (1988) Immunoaffinity purification and neutralization of scrapie prion infectivity. *Proceedings of the National Academy of Sciences* **85**, 6617-6621
24. Büeler, H., Fischer, M., Lang, Y., Bluethmann, H., Lipp, H.-P., DeArmond, S. J., Prusiner, S. B., Aguet, M., and Weissmann, C. (1992) Normal development and behaviour of mice lacking the neuronal cell-surface PrP protein. *Nature* **356**, 577-582
25. Büeler, H., Aguzzi, A., Sailer, A., Greiner, R.-A., Autenried, P., Aguet, M., and Weissmann, C. (1993) Mice devoid of PrP are resistant to scrapie. *Cell* **73**, 1339-1347
26. Griffith, J.S. (1967) Self-replication and scrapie. *Nature* **215**, 1043−1044
27. Weissmann, C. (1991) A'unified theory'of prion propagation.
28. Kretzschmar , H. A., Stowring, L. E., Westaway, D., Stubblebine, W. H., Prusiner, S. B., and Dearmond, S. J. (1986) Molecular cloning of a human prion protein cDNA. *DNA* **5**, 315-324

29. Prusiner, S. B. (1991) Molecular biology of prion diseases. *Science* **252**, 1515-1522
30. Riesner, D. (2003) Biochemistry and structure of PrP^{C} and PrP^{Sc}. *British Medical Bulletin* **66**, 21-33
31. Zahn, R., Liu, a., Lührs, T., Riek, R., von Schroetter, C., López García, F., Billeter, M., Calzolai, L., Wider, G., and Wüthrich, K. (2000) NMR solution structure of the human prion protein. *Proceedings of the National Academy of Sciences of the United States of America* **97**, 145-150
32. Biljan, I., Giachin, G., Ilc, G., Zhukov, I., Plavec, J., and Legname, G. (2012) Structural basis for the protective effect of the human prion protein carrying the dominant-negative E219K polymorphism. *The Biochemical journal* **446**, 243-251
33. Fasano, C., Campana, V., and Zurzolo, C. (2006) Prions: protein only or something more? Overview of potential prion cofactors. *J Mol Neurosci* **29**, 195-214
34. Westergard, L., Christensen, H. M., and Harris, D. a. (2007) The cellular prion protein (PrP(C)): its physiological function and role in disease. *Biochimica et biophysica acta* **1772**, 629-644
35. Zomosa-Signoret, V., Arnaud, J.-D., Fontes, P., Alvarez-Martinez, M.-T., and Liautard, J.-P. (2008) Physiological role of the cellular prion protein. *Veterinary research* **39**, 1-16
36. Campana, V., Sarnataro, D., and Zurzolo, C. (2005) The highways and byways of prion protein trafficking. *Trends in cell biology* **15**, 102-111
37. Chiesa, R., and Harris, D. a. (2009) Fishing for prion protein function. *PLoS Biology* **7**, 0439-0443
38. Sakaguchi, S., Katamine, S., Nishida, N., Moriuchi, R., Shigematsu, K., Sugimoto, T., Nakatani, A., Kataoka, Y., Houtani, T., and Shirabe, S. (1996) Loss of cerebellar Purkinje cells in aged mice homozygous for a disrupted PrP gene. *Nature* **380**, 528-531
39. Moore, R. C., Lee, I. Y., Silverman, G. L., Harrison, P. M., Strome, R., Heinrich, C., Karunaratne, A., Pasternak, S. H., Chishti, M. A., and Liang, Y. (1999) Ataxia in prion protein (PrP)-deficient mice is associated with upregulation of the novel PrP-like protein doppel. *Journal of molecular biology* **292**, 797-817
40. Weissmann, C., and Aguzzi, A. (1999) PrP's double causes trouble. *Science* **286**, 914
41. Behrens, A., and Aguzzi, A. (2002) Small is not beautiful: antagonizing functions for the prion protein PrP C and its homologue Dpl. *Trends in neurosciences* **25**, 150-154

42. Watts, J. C., and Westaway, D. (2007) The prion protein family: diversity, rivalry, and dysfunction. *Biochimica et Biophysica Acta (BBA)-Molecular Basis of Disease* **1772**, 654-672
43. Ciric, D., and Rezaei, H. (2015) Biochemical insight into the prion protein family. *Frontiers in cell and developmental biology* **3**
44. Kanaani, J., Prusiner, S. B., Diacovo, J., Baekkeskov, S., and Legname, G. (2005) Recombinant prion protein induces rapid polarization and development of synapses in embryonic rat hippocampal neurons in vitro. *Journal of neurochemistry* **95**, 1373-1386
45. Van der Kamp, M. W., and Daggett, V. (2009) The consequences of pathogenic mutations to the human prion protein. *Protein Engineering Design and Selection* **22**, 461-468
46. Wickner, R. B. (1994) [URE3] as an altered URE2 protein: evidence for a prion analog in Saccharomyces cerevisiae. *Science* **264**, 566-569
47. Chien, P., Weissman, J. S., and DePace, A. H. (2004) Emerging principles of conformation-based prion inheritance. *Annual review of biochemistry* **73**, 617-656
48. Dobson, C. M. (1999) Protein misfolding, evolution and disease. *Trends in biochemical sciences* **24**, 329-332
49. Caughey, B., Baron, G. S., Chesebro, B., and Jeffrey, M. (2009) Getting a grip on prions: oligomers, amyloids, and pathological membrane interactions. *Annual review of biochemistry* **78**, 177-204
50. Diaz-Espinoza, R., and Soto, C. (2012) High-resolution structure of infectious prion protein: the final frontier. *Nature structural & molecular biology* **19**, 370-377
51. Eanes, E., and Glenner, G. (1968) X-ray diffraction studies on amyloid filaments. *Journal of Histochemistry & Cytochemistry* **16**, 673-677
52. Wille, H., Bian, W., McDonald, M., Kendall, A., Colby, D. W., Bloch, L., Ollesch, J., Borovinskiy, A. L., Cohen, F. E., and Prusiner, S. B. (2009) Natural and synthetic prion structure from X-ray fiber diffraction. *Proceedings of the National Academy of Sciences* **106**, 16990-16995
53. Cobb, N. J., and Surewicz, W. K. (2009) Prion diseases and their biochemical mechanisms†. *Biochemistry* **48**, 2574-2585
54. Pan, K. M., Baldwin, M., Nguyen, J., Gasset, M., Serban, A., Groth, D., Mehlhorn, I., Huang, Z., Fletterick, R. J., and Cohen, F. E. (1993) Conversion of alpha-helices into

beta-sheets features in the formation of the scrapie prion proteins. *Proceedings of the National Academy of Sciences of the United States of America* **90**, 10962-10966

55. Caughey, B. W., Dong, A., Bhat, K. S., Ernst, D., Hayes, S. F., and Caughey, W. S. (1991) Secondary structure analysis of the scrapie-associated protein PrP 27-30 in water by infrared spectroscopy. *Biochemistry* **30**, 7672-7680
56. Kuwata, K., Matumoto, T., Cheng, H., Nagayama, K., James, T. L., and Roder, H. (2003) NMR-detected hydrogen exchange and molecular dynamics simulations provide structural insight into fibril formation of prion protein fragment 106–126. *Proceedings of the National Academy of Sciences* **100**, 14790-14795
57. Barducci, A., Chelli, R., Procacci, P., and Schettino, V. (2005) Misfolding pathways of the prion protein probed by molecular dynamics simulations. *Biophysical journal* **88**, 1334-1343
58. Ji, H.-F., and Zhang, H.-Y. (2010) Beta-Sheet Constitution of Prion Proteins. *Trends in biochemical sciences* **35**, 129-134
59. Acevedo-Morantes, C. Y., and Wille, H. (2014) The Structure of Human Prions: From Biology to Structural Models—Considerations and Pitfalls. *Viruses* **6**, 3875-3892
60. Wille, H., Michelitsch, M. D., Guenebaut, V., Supattapone, S., Serban, A., Cohen, F. E., Agard, D. A., and Prusiner, S. B. (2002) Structural studies of the scrapie prion protein by electron crystallography. *Proceedings of the National Academy of Sciences of the United States of America* **99**, 3563-3568
61. Govaerts, C., Wille, H., Prusiner, S. B., and Cohen, F. E. (2004) Evidence for assembly of prions with left-handed β-helices into trimers. *Proceedings of the National academy of Sciences of the United States of America* **101**, 8342-8347
62. DeMarco, M. L., Silveira, J., Caughey, B., and Daggett, V. (2006) Structural properties of prion protein protofibrils and fibrils: an experimental assessment of atomic models. *Biochemistry* **45**, 15573-15582
63. Wasmer, C., Lange, A., Van Melckebeke, H., Siemer, A. B., Riek, R., and Meier, B. H. (2008) Amyloid fibrils of the HET-s (218–289) prion form a β solenoid with a triangular hydrophobic core. *Science* **319**, 1523-1526
64. DeMarco, M. L., and Daggett, V. (2004) From conversion to aggregation: protofibril formation of the prion protein. *Proceedings of the National Academy of Sciences of the United States of America* **101**, 2293-2298
65. Cobb, N. J., Sönnichsen, F. D., McHaourab, H., and Surewicz, W. K. (2007) Molecular architecture of human prion protein amyloid: a parallel, in-register beta-

structure. *Proceedings of the National Academy of Sciences of the United States of America* **104**, 18946-18951

66. Sawaya, M. R., Sambashivan, S., Nelson, R., Ivanova, M. I., Sievers, S. A., Apostol, M. I., Thompson, M. J., Balbirnie, M., Wiltzius, J. J., and McFarlane, H. T. (2007) Atomic structures of amyloid cross-&bgr; spines reveal varied steric zippers. *Nature* **447**, 453-457
67. Apostol, M. I., Perry, K., and Surewicz, W. K. (2013) Crystal structure of a human prion protein fragment reveals a motif for oligomer formation. *J Am Chem Soc* **135**, 10202-10205
68. Chakrabarti, O., Ashok, A., and Hegde, R. S. (2009) Prion protein biosynthesis and its emerging role in neurodegeneration. *Trends Biochem Sci* **34**, 287-295
69. Lehmann, S., Milhavet, O., and Mange, A. (1999) Trafficking of the cellular isoform of the prion protein. *Biomedicine & pharmacotherapy* **53**, 39-46
70. Prado, M. A., Alves-Silva, J., Magalhaes, A. C., Prado, V. F., Linden, R., Martins, V. R., and Brentani, R. R. (2004) PrPc on the road: trafficking of the cellular prion protein. *J Neurochem* **88**, 769-781
71. Taylor, D. R., and Hooper, N. M. (2006) The prion protein and lipid rafts. *Mol Membr Biol* **23**, 89-99
72. Morris, R. J., Parkyn, C. J., and Jen, A. (2006) Traffic of prion protein between different compartments on the neuronal surface, and the propagation of prion disease. *FEBS letters* **580**, 5565-5571
73. Harris, D. A. (2003) Trafficking, turnover and membrane topology of PrP Protein function in prion disease. *British medical bulletin* **66**, 71-85
74. Chakrabarti, O., Ashok, A., and Hegde, R. S. (2009) Prion protein biosynthesis and its emerging role in neurodegeneration. *Trends in biochemical sciences* **34**, 287-295
75. Pauline, M. R., Anthony H. M., Mark R. W., and Dwek, R. A. (2002) Glycosylation and prion protein. *Current Opinion in Structural Biology* **12,** 578-586
76. Harris, D. a. (1999) Cell biological studies of the prion protein. *Current issues in molecular biology* **1**, 65-75
77. Sunyach, C., Jen, A., Deng, J., Fitzgerald, K. T., Frobert, Y., Grassi, J., McCaffrey, M. W., and Morris, R. (2003) The mechanism of internalization of glycosylphosphatidylinositol-anchored prion protein. *The EMBO journal* **22**, 3591-3601

78. Nunziante, M., Gilch, S., and Schatzl, H. M. (2003) Essential role of the prion protein N terminus in subcellular trafficking and half-life of cellular prion protein. *J Biol Chem* **278**, 3726-3734

79. Shyng, S. L., Huber, M. T., and Harris, D. A. (1993) A prion protein cycles between the cell surface and an endocytic compartment in cultured neuroblastoma cells. *J Biol Chem* **268**, 15922-15928

80. Lee, K. S., Magalhaes, A. C., Zanata, S. M., Brentani, R. R., Martins, V. R., and Prado, M. A. (2001) Internalization of mammalian fluorescent cellular prion protein and N-terminal deletion mutants in living cells. *J Neurochem* **79**, 79-87

81. Magalhães, A. C., Silva, J. A., Lee, K. S., Martins, V. R., Prado, V. F., Ferguson, S. S., Gomez, M. V., Brentani, R. R., and Prado, M. A. (2002) Endocytic intermediates involved with the intracellular trafficking of a fluorescent cellular prion protein. *Journal of Biological Chemistry* **277**, 33311-33318

82. Peters, P. J., Mironov, A., Peretz, D., van Donselaar, E., Leclerc, E., Erpel, S., DeArmond, S. J., Burton, D. R., Williamson, R. A., and Vey, M. (2003) Trafficking of prion proteins through a caveolae-mediated endosomal pathway. *The Journal of cell biology* **162**, 703-717

83. Perera, W. S. S., and Hooper, N. M. (2001) Ablation of the metal ion-induced endocytosis of the prion protein by disease-associated mutation of the octarepeat region. *Current Biology* **11**, 519-523

84. Lehmann, S., and Harris, D. A. (1996) Mutant and infectious prion proteins display common biochemical properties in cultured cells. *J Biol Chem* **271**, 1633-1637

85. Ma, J., and Lindquist, S. (2001) Wild-type PrP and a mutant associated with prion disease are subject to retrograde transport and proteasome degradation. *Proceedings of the National Academy of Sciences* **98**, 14955-14960

86. Grassmann, A., Wolf, H., Hofmann, J., Graham, J., and Vorberg, I. (2013) Cellular aspects of prion replication in vitro. *Viruses* **5**, 374-405

87. Kim, S. J., and Hegde, R. S. (2002) Cotranslational partitioning of nascent prion protein into multiple populations at the translocation channel. *Molecular biology of the cell* **13**, 3775-3786

88. Béranger, F., Mangé, A., Goud, B., and Lehmann, S. (2002) Stimulation of PrPC retrograde transport toward the endoplasmic reticulum increases accumulation of PrP^{Sc} in prion-infected cells. *Journal of Biological Chemistry* **277**, 38972-38977

89. Ma, J., Wollmann, R., and Lindquist, S. (2002) Neurotoxicity and neurodegeneration when PrP accumulates in the cytosol. *Science* **298**, 1781-1785

90. Caughey, B., and Baron, G. S. (2006) Prions and their partners in crime. *Nature* **443**, 803-810

91. Février, B., Vilette, D., Laude, H., and Raposo, G. (2005) Exosomes: a bubble ride for prions? *Traffic* **6**, 10-17

92. Magalhães, A. C., Baron, G. S., Lee, K. S., Steele-Mortimer, O., Dorward, D., Prado, M. a. M., and Caughey, B. (2005) Uptake and neuritic transport of scrapie prion protein coincident with infection of neuronal cells. *The Journal of neuroscience : the official journal of the Society for Neuroscience* **25**, 5207-5216

93. Rustom, A., Saffrich, R., Markovic, I., Walther, P., and Gerdes, H.-H. (2004) Nanotubular highways for intercellular organelle transport. *Science* **303**, 1007-1010

94. Caughey, B., Raymond, G. J., and Bessen, R. A. (1998) Strain-dependent differences in β-sheet conformations of abnormal prion protein. *Journal of Biological Chemistry* **273**, 32230-32235

95. Chiti, F., and Dobson, C. M. (2006) Protein misfolding, functional amyloid, and human disease. *Annual review of biochemistry* **75**, 333-366

96. Silveira, J. R., Raymond, G. J., Hughson, A. G., Race, R. E., Sim, V. L., Hayes, S. F., and Caughey, B. (2005) The most infectious prion protein particles. *Nature* **437**, 257-261

97. Tixador, P., Herzog, L., Reine, F., Jaumain, E., Chapuis, J. m., Le Dur, A., Laude, H., and Beringue, V. (2010) The physical relationship between infectivity and prion protein aggregates is strain-dependent. *PLoS Pathog* **6**, e1000859

98. Ayers, J. I., Schutt, C. R., Shikiya, R. A., Aguzzi, A., Kincaid, A. E., and Bartz, J. C. (2011) The strain-encoded relationship between PrP^{Sc} replication, stability and processing in neurons is predictive of the incubation period of disease. *PLoS Pathog* **7**, e1001317

99. Hornemann, S., and Glockshuber, R. (1998) A scrapie-like unfolding intermediate of the prion protein domain PrP (121–231) induced by acidic pH. *Proceedings of the National Academy of Sciences* **95**, 6010-6014

100. Baskakov, I. V., Legname, G., Prusiner, S. B., and Cohen, F. E. (2001) Folding of prion protein to its native alpha-helical conformation is under kinetic control. *The Journal of biological chemistry* **276**, 19687-19690

101. Knaus, K. J., Morillas, M., Swietnicki, W., Malone, M., Surewicz, W. K., and Yee, V. C. (2001) Crystal structure of the human prion protein reveals a mechanism for oligomerization. *Nature Structural & Molecular Biology* **8**, 770-774

102. Cobb, N. J., Apetri, A. C., and Surewicz, W. K. (2008) Prion protein amyloid formation under native-like conditions involves refolding of the C-terminal alpha-helical domain. *The Journal of biological chemistry* **283**, 34704-34711

103. Post, K., Pitschke, M., Schäfer, O., Wille, H., Appel, T. R., Kirsch, D., Mehlhorn, I., Serban, H., Prusiner, S. B., and Riesner, D. (1998) Rapid Acquisition of ß-Sheef Structure in the Priori Protein Prior to Multimer Formation. **379**, 1307-1317

104. Jansen, K., Schäfer, O., Birkmann, E., Post, K., Serban, H., Prusiner, S. B., and Riesner, D. (2001) Structural intermediates in the putative pathway from the cellular prion protein to the pathogenic form. *Biological chemistry* **382**, 683-691

105. Stöhr, J., Weinmann, N., Wille, H., Kaimann, T., Nagel-Steger, L., Birkmann, E., Panza, G., Prusiner, S. B., Eigen, M., and Riesner, D. (2008) Mechanisms of prion protein assembly into amyloid. *Proceedings of the National Academy of Sciences of the United States of America* **105**, 2409-2414

106. Legname, G., Baskakov, I. V., Nguyen, H.-O. B., Riesner, D., Cohen, F. E., DeArmond, S. J., and Prusiner, S. B. (2004) Synthetic mammalian prions. *Science (New York, N.Y.)* **305**, 673-676

107. Colby, D. W., Giles, K., Legname, G., Wille, H., Baskakov, I. V., DeArmond, S. J., and Prusiner, S. B. (2009) Design and construction of diverse mammalian prion strains. *Proceedings of the National Academy of Sciences* **106**, 20417-20422

108. Makarava, N., Kovacs, G. G., Bocharova, O., Savtchenko, R., Alexeeva, I., Budka, H., Rohwer, R. G., and Baskakov, I. V. (2010) Recombinant prion protein induces a new transmissible prion disease in wild-type animals. *Acta neuropathologica* **119**, 177-187

109. Kocisko, D. A., Come, J. H., Priola, S. A., Chesebro, B., Raymond, G. J., Lansbury, P. T., and Caughey, B. (1994) Cell-free formation of protease-resistant prion protein. *Nature* **370**, 471-474

110. Saborio, G. P., Permanne, B., and Soto, C. (2001) Sensitive detection of pathological prion protein by cyclic amplification of protein misfolding. *Nature* **411**, 810-813

111. Castilla, J., Gonzalez-Romero, D., Saá, P., Morales, R., De Castro, J., and Soto, C. (2008) Crossing the species barrier by PrP Sc replication in vitro generates unique infectious prions. *Cell* **134**, 757-768

112. Castilla, J., Morales, R., Saá, P., Barria, M., Gambetti, P., and Soto, C. (2008) Cell-free propagation of prion strains. *The EMBO journal* **27**, 2557-2566

113. Stathopulos, P. B., Scholz, G. A., Hwang, Y. M., Rumfeldt, J. A., Lepock, J. R., and Meiering, E. M. (2004) Sonication of proteins causes formation of aggregates that resemble amyloid. *Protein Science* **13**, 3017-3027

114. Deleault, N. R., Lucassen, R. W., and Supattapone, S. (2003) RNA molecules stimulate prion protein conversion. *Nature* **425**, 717-720

115. Deleault, N. R., Harris, B. T., Rees, J. R., and Supattapone, S. (2007) Formation of native prions from minimal components in vitro. *Proceedings of the National Academy of Sciences* **104**, 9741-9746

116. Wang, F., Wang, X., Yuan, C.-G., and Ma, J. (2010) Generating a prion with bacterially expressed recombinant prion protein. *Science (New York, N.Y.)* **327**, 1132-1135

117. Wang, F., Zhang, Z., Wang, X., Li, J., Zha, L., Yuan, C.-G., Weissmann, C., and Ma, J. (2012) Genetic informational RNA is not required for recombinant prion infectivity. *Journal of virology* **86**, 1874-1876

118. Deleault, N. R., Geoghegan, J. C., Nishina, K., Kascsak, R., Williamson, R. A., and Supattapone, S. (2005) Protease-resistant prion protein amplification reconstituted with partially purified substrates and synthetic polyanions. *Journal of Biological Chemistry* **280**, 26873-26879

119. Geoghegan, J. C., Valdes, P. A., Orem, N. R., Deleault, N. R., Williamson, R. A., Harris, B. T., and Supattapone, S. (2007) Selective incorporation of polyanionic molecules into hamster prions. *Journal of Biological Chemistry* **282**, 36341-36353

120. Deleault, N. R., Kascsak, R., Geoghegan, J. C., and Supattapone, S. (2010) Species-dependent differences in cofactor utilization for formation of the protease-resistant prion protein in vitro. *Biochemistry* **49**, 3928-3934

121. Deleault, N. R., Piro, J. R., Walsh, D. J., Wang, F., Ma, J., and Geoghegan, J. C. (2012) Isolation of phosphatidylethanolamine as a solitary cofactor for prion formation in the absence of nucleic acids. *Proceedings of the National Academy of Sciences* **109,** 8546-8551

122. Gill, A. C., Agarwal, S., Pinheiro, T. J., and Graham, J. F. (2010) Structural requirements for efficient prion protein conversion: Cofactors may promote a conversion-competent structure for PrPC. *Prion* **4**, 235-243

123. Ma, J. (2012) The role of cofactors in prion propagation and infectivity. *PLoS pathogens* **8**, e1002589
124. Supattapone, S. (2014) Elucidating the role of cofactors in mammalian prion propagation. *Prion* **8**, 100-105
125. Deleault, N. R., Walsh, D. J., Piro, J. R., Wang, F., Wang, X., Ma, J., Rees, J. R., and Supattapone, S. (2012) Cofactor molecules maintain infectious conformation and restrict strain properties in purified prions. *Proceedings of the National Academy of Sciences* **109**, E1938-E1946
126. Noble, G. P., Wang, D. W., Walsh, D. J., Barone, J. R., Miller, M. B., Nishina, K. A., Li, S., and Supattapone, S. (2015) A Structural and Functional Comparison Between Infectious and Non-Infectious Autocatalytic Recombinant PrP Conformers. *PLoS Pathog* **11**, e1005017
127. Wang, F., Yang, F., Hu, Y., Wang, X., Wang, X., Jin, C., and Ma, J. (2007) Lipid interaction converts prion protein to a PrP^{Sc}-like proteinase K-resistant conformation under physiological conditions. *Biochemistry* **46**, 7045-7053
128. Piro, J. R., Harris, B. T., and Supattapone, S. (2011) In situ photodegradation of incorporated polyanion does not alter prion infectivity. *PLoS Pathog* **7**, e1002001-e1002001
129. Ma, J. (2012) The role of cofactors in prion propagation and infectivity. *PLoS Pathog* **8**, e1002589-e1002589
130. Miller, M. B., Wang, D. W., Wang, F., Noble, G. P., Ma, J., Woods, V. L., Li, S., and Supattapone, S. (2013) Cofactor molecules induce structural transformation during infectious prion formation. *Structure* **21**, 2061-2068
131. Collinge, J. (2001) Prion diseases of humans and animals: their causes and molecular basis. *Annu Rev Neurosci* **24**, 519-550
132. Dalal, V., Bhattacharya, M., Narang, D., Sharma, P. K., and Mukhopadhyay, S. (2012) Nanoscale Fluorescence Imaging of Single Amyloid Fibrils. *The Journal of Physical Chemistry Letters* **3**, 1783-1787
133. Cordeiro, Y., Kraineva, J., Ravindra, R., Lima, L. M., Gomes, M. P., Foguel, D., Winter, R., and Silva, J. L. (2004) Hydration and packing effects on prion folding and beta-sheet conversion. High pressure spectroscopy and pressure perturbation calorimetry studies. *J Biol Chem* **279**, 32354-32359

134. Pal, S. K., Peon, J., and Zewail, A. H. (2002) Biological water at the protein surface: dynamical solvation probed directly with femtosecond resolution. *Proc Natl Acad Sci U S A* **99**, 1763-1768

135. Bagchi, B. (2005) Water dynamics in the hydration layer around proteins and micelles. *Chem Rev* **105**, 3197-3219

136. Fernandez, A., and Scheraga, H. A. (2003) Insufficiently dehydrated hydrogen bonds as determinants of protein interactions. *Proc Natl Acad Sci U S A* **100**, 113-118

137. De Simone, A., Dodson, G. G., Verma, C. S., Zagari, A., and Fraternali, F. (2005) Prion and water: tight and dynamical hydration sites have a key role in structural stability. *Proc Natl Acad Sci U S A* **102**, 7535-7540

138. Jaunmuktane, Z., Mead, S., Ellis, M., Wadsworth, J. D. F., Nicoll, A. J., Kenny, J., Launchbury, F., Linehan, J., Richard-Loendt, A., Walker, A. S., Rudge, P., Collinge, J., and Brandner, S. (2015) Evidence for human transmission of amyloid-[bgr] pathology and cerebral amyloid angiopathy. *Nature* **525**, 247-250

Chapter 2

Conformational Switching and Nanoscale Assembly of Human Prion Protein into Diverse Polymorphic Amyloids *via* Structurally-Labile Oligomers

This work has been published in *Biochemistry.*

V. Dalal, S. Arya, M. Bhattacharya and S. Mukhopadhyay "Conformational Switching and Nanoscale Assembly of Human Prion Protein into Diverse Polymorphic Amyloids *via* Structurally-Labile Oligomers" ***Biochemistry*** 2015, *54*, 7505-7513.

2.1 INTRODUCTION

Prion diseases belong to a unique class of fatal neurodegenerative disorders that include transmissible spongiform encephalopathies and are manifested as infectious, genetic and sporadic diseases. The human prion diseases include Creutzfeldt-Jakob disease, kuru, fatal familial insomnia and Gerstmann-Sträussler-Scheinker syndrome, whereas, the animal prion diseases are scrapie and bovine spongiform encephalopathy or 'mad cow' disease (1-7). An enlarging body of data reveals that the key step in the pathogenesis is the misfolding and aggregation of an endogenous glycosylphosphatidylinositol-anchored protein, termed as the prion protein (PrP) (1-7). Recent studies have proposed that this prion-like conformational switching serves as the underlying mechanism in various neurodegenerative disorders including Alzheimer's and Parkinson's diseases that are characterized by amyloid deposits in brain (7). Additionally, the fact that infectious prions can be generated from recombinant PrP provides compelling evidence in favor of the protein-only hypothesis (8, 9). Hence, recapitulating the transition of PrP from the native to the misfolded form under *in vitro* cell-free conditions serves as a good model for unraveling the cascade of molecular events during the conversion process (10-15).

PrP is largely α-helical in the normal cellular form (PrP^{C}) and converts into a predominantly β-sheet-rich (scrapie) form (PrP^{Sc}) that matures into amyloids (1-6). The proteinase-K treatment of PrP^{Sc} results in a protease-resistant fragment (PrP 90-231) that is infectious, displays the attributes of scrapie amyloid aggregates and has been observed to accumulate in prion-infected brains (5). Therefore, a construct encompassing residues 90 to 231 (protease-resistant core of PrP^{Sc}) has been widely used to address several important and intriguing aspects like self-perpetuating conformational propagation, infectivity and the strain phenomenon (16-20). The solution NMR structure of recombinant human PrP 90-231 is shown in Figure 2.5a. In its native form, the N-terminal region encompassing residues 90 to 125 is disordered. The well-structured globular domain (residues 126 to 231) consists of three α-helices and two short antiparallel β-strands (21, 22). In the presence of mild denaturants and other aggregation-conducive *in vitro* conditions, PrP misfolds and self-associates into amyloid fibrils resembling various biochemical characteristics of PrP^{Sc} (11, 12). However, the structural elucidation of the misfolded and aggregated form has been challenging due to the insolubility and the heterogeneous nature of the aggregates (23, 24).

Since PrP^{C} is a membrane-anchored protein (25), membranes especially lipid rafts-mediated misfolding of both cellular and recombinantly-expressed PrP has been hypothesized to play a pivotal role in its conversion to the protease-resistant pathogenic isoform (PrP^{Sc}) and in the prion disease progression (8, 9, 26-29). It has also been reported that PrP-lipid interaction is primarily dependent on the nature of the lipid head-group e.g. anionic lipids impose significant conformational alterations compared to the neutral or cationic lipids (9). Apropos, a diverse set of endogenous or synthetic lipids, RNA, polyanions and other cofactors have been reported to influence the trans-conversion of recombinant PrP to the disease-causing form (30-33). Despite all the advancements, the underlying molecular mechanism of coupled conformational switch and aggregation that governs the pathogenesis still remains elusive.

Sodium dodecyl sulfate (SDS), a well-known anionic lipid mimetic, has been used to stimulate the prion conformational conversion in a manner similar to anionic lipids (34-40). A low (non-denaturing) sub-micellar concentration of SDS together with salt is believed to mimic the membrane environment and has been used to transform hamster PrP into infectious amyloid fibrils (37-39). Even low mM concentrations of SDS, utilized in the modified protein misfolding cyclic amplification protocol, could trigger the formation of infectious prions from recombinant PrP in lieu of the PrP isolated from brain extract (41). It is therefore imperative to understand the molecular mechanism of SDS-induced PrP misfolding and aggregation leading to amyloid formation *in vitro*. In this work, we have used recombinant human PrP 90-231 to elucidate the molecular mechanism of misfolding and aggregation by detecting and characterizing the unique structural and morphological features of the early key intermediates on the amyloid pathway in the presence of SDS.

2.2 EXPERIMENTAL SECTION

2.2.1 Materials

All the reagents used for different experiments were procured from Sigma (St. Louis, MO), unless otherwise mentioned and were used without further purification. All the solutions and buffers were prepared in Milli-Q water and the pH of the buffers was adjusted on a pH 827 lab meter from Metrohm.

2.2.2 Protein expression, purification and labeling

His-tagged recombinant human prion protein 90-231 gene cloned in pQE-30 was expressed in *E. Coli* strain SG13009[pREP4]. Culture was induced with 1 mM isopropyl-beta-D-thiogalacto-pyranoside (IPTG, Gold Biotechnology) and lysed by sonication in lysis buffer (pH 8) containing 50 mM Tris, 100 mM NaCl, 1 mM EDTA and 0.1% triton X - 100. The inclusion bodies pellet obtained after centrifugation was resuspended in denaturing buffer (100 mM NaH_2PO_4, 10 mM Tris, 8 M urea and 10 mM β-mercaptoethanol, pH 8) and purified on nickel-NTA chromatography as described previously (42). The double cysteine (A120C/S230C) mutant was made using QuikChange® site-directed mutagenesis kit (Stratagene). For FRET measurements, the dual cysteine mutant (A120C/S230C) was first labeled non-specifically with AlexaFluor 488 C_5-maleimide (Invitrogen) under denatured conditions (pH 7.2). The singly labeled protein was separated from unlabeled and double labeled species on the ion exchange column (CM Sepharose, pH 6.4). The mono-labeled (protein-A488 conjugate) was further reacted with AlexaFluor 647 C_5-maleimide (Invitrogen). The double labeled protein was refolded on the PD-10 column (GE Healthcare).

2.2.3 CD spectroscopy

The far-UV CD spectra were recorded on an Applied Photophysics Chirascan CD spectrometer at room temperature. Data were collected with 5 μM protein (native) and upon addition of 1 mM SDS with and without 250 mM NaCl. The spectra were averaged over three scans and were blank subtracted.

2.2.4 Fluorescence spectroscopy

Steady state fluorescence measurements were carried out on Fluoromax-4 (Horiba Jobin Yvon, NJ). Tryptophan fluorescence was monitored using 295 nm excitation wavelength. For Nile Red binding assay, 15 μM protein and dye were used in the presence of 1 mM SDS with and without 250 mM NaCl and the samples were excited at 488 nm. For FRET measurements, AlexaFluor 488 (donor) and AlexaFluor 647 (acceptor) doubly labeled protein sample (50 nM) was excited at 488 nm (slit width 2 nm) and the FRET efficiency (E) was estimated using the following relationship:

$$E = 1 - F_{DA} / F_D \qquad \text{(Eq. 2.1)}$$

where, F_{DA} and F_D are the fluorescence of the donor in presence and absence of acceptor (43).

The steady state fluorescence anisotropy (r_{ss}) of Trp was estimated using the following relationship:

$$r_{ss} = (I_{II} - I_{\perp} G) / (I_{II} - 2I_{\perp} G) \qquad \text{(Eq. 2.2)}$$

where, I_{II} and $I_{\perp}$ are fluorescence intensities collected using parallel and perpendicular geometry of the polarizer, respectively and the perpendicular components were corrected using a G-factor (43).

2.2.5 Cross-linking assay

Oligomers were analyzed on SDS-PAGE by glutaraldehyde cross-linking assay. After incubating the protein with 1 mM SDS and 1 mM SDS + 250 mM NaCl for ~ 3 hours, it was treated with 0.05 % of glutaraldehyde for 15 minutes at room temperature. Reaction was quenched by adding 0.05 M sodium borohydride and again incubating for 15 minutes before running the samples on denaturing SDS-PAGE and was visualized by coomassie blue staining (44).

2.2.6 AFM imaging

The AFM imaging was performed on MultiView 2000^{TM} instrument (Nanonics Imaging Ltd., Jerusalem, Israel) operating in intermittent contact mode based on phase feedback. AFM scanning was done under ambient environmental conditions in sample scanning configuration on Quartz software (provided with the MultiView) using Cr-coated cantilevered glass probe of diameter ~10 nm oscillating at a resonance frequency of 32.13 kHz. For AFM imaging of oligomers and fibrils, the reaction mixtures were deposited onto freshly cleaved muscovite mica (Grade V-4 mica from SPI, PA). After incubating for 30 minutes, samples were washed with filtered water and dried under nitrogen. AFM images of 256 x 256 pixels or 400 x 400 pixels were collected with sample a delay of 6 ms and 4 ms, respectively. The acquired AFM images were processed using WSxM version 4 develop 11.6 software provided with the AFM setup (45). To obtain the height profiles and distributions of oligomers the images were analyzed using Quartz and WSxM software and were plotted using Origin 8.5 software.

2.2.7 Proteinase-K digestion

Native PrP, β-oligomers and amyloid fibrils were treated with proteinase-K for 1 hour at 37 °C. The digestion reaction was stopped by addition of gel loading buffer and heating the samples at 95 °C for 15 minutes (36) and were analyzed on 15% SDS-PAGE after coomassie blue staining.

2.2.8 Raman spectroscopy

Raman spectra of the samples were recorded on an inVia Raman microscope with 180° scattering geometry (Renishaw, UK). The samples were prepared freshly using the 15 µM protein after overnight incubation samples were directly applied on glass slide covered with aluminum and subsequently air dried or dried under a stream of nitrogen. Approximately 350 mW of 785 nm from an NIR laser was used as excitation source and focused into the sample spot by a 20X objective lens (Nikon, Japan). The scattered light was collected with the same objective and passed through an edge filter (785 nm) in order to remove the Rayleigh scattering. A 1200 l/mm grating was used for the dispersion of the scattered light and the signal was finally detected with air-cooled CCD detector. The data were acquired using Wire 3.1 software provided with the spectrometer. All the data were corrected for tilt in the baseline using cubic spline interpolation method and smoothened in Wire 3.1 software. The baseline corrected and smoothened Raman spectra were finally plotted in Origin 8.5 software. The deconvolution of Raman spectra was done in Origin 8.5 software as described previously (46).

2.2.9 Cytotoxicity assay

HeLa cells were maintained in 75 cm^2 flasks in Dulbecco's modified Eagle's medium supplemented with 10% FBS, non-essential amino acids and penicillin/streptomycin, and were grown in an atmosphere of 5% CO_2 at 37 °C. For cell toxicity assay, cells were plated in 96-well plate at a seeding density of 10,000 cells per well in 100 µL media. SDS induced β-oligomers and SDS-NaCl induced amyloid fibrils were generated using 15 µM protein and used to treat cells after 1 day at a final concentration of ~ 1 µM. As control experiments, respective buffers 5 mM phosphate buffer with 1 mM SDS and phosphate buffer with 1 mM SDS and 250 mM NaCl (pH 7.2) were added to the cells. After 24 h of incubation, cells were washed and 0.5 mg/ml of 3-(4,5-dimethylthiazol-2-yl)-2,5-diphenyltetrazolium bromide (MTT) was added to each well and incubated further for 4 h at 37 °C. MTT is reduced by

mitochondrial enzymes to insoluble formazan that was solubilized in dimethylsulfoxide. For assessing cell survival the quantification of solubilized formazan was performed spectrophotometrically at 490 nm in a 96-well plate reader (iMark™ microplate, Bio-rad). The experiment was repeated 3 times in triplicates. For qualitative evaluation, 3 x 10^5 cells were seeded in 35 mm dish and treatment was done as above. Images were captured with AxioCam ERc 5s microscope camera after 40 h of treatment under inverted phase contrast microscope equipped with 40 X objective (Axio Vert.A1, Zeiss).

2.3 RESULTS AND DISCUSSION

First, we directed our efforts to dissect the effects of SDS and salt on human PrP using circular dichroism and fluorescence spectroscopy. Far-UV circular dichroism (CD) indicated that at the specific sub-micellar concentration of SDS, the native α-helix-rich state converts into a β-sheet-rich state (Figure 2.1, 2.2a). These results are in agreement with the studies on the hamster prion protein (37,38). In order to monitor the onset of PrP α → β conformational switch, the SDS concentration was varied (50 μM - 10 mM) while keeping the protein concentration constant at 5 μM. It was observed that 0.5 mM of SDS is the threshold concentration for the transition to a β-sheet-rich state that progressively accumulated till the addition of 2 mM of SDS (Figure 2.1). Further increase in the SDS concentration leads to complete unfolding of PrP. Hence, we chose 1 mM SDS as the optimal concentration in the present study. Upon addition of salt (250 mM NaCl), the β-rich state undergoes partial unfolding as indicated by a significant drop in the secondary structural contents. Under this

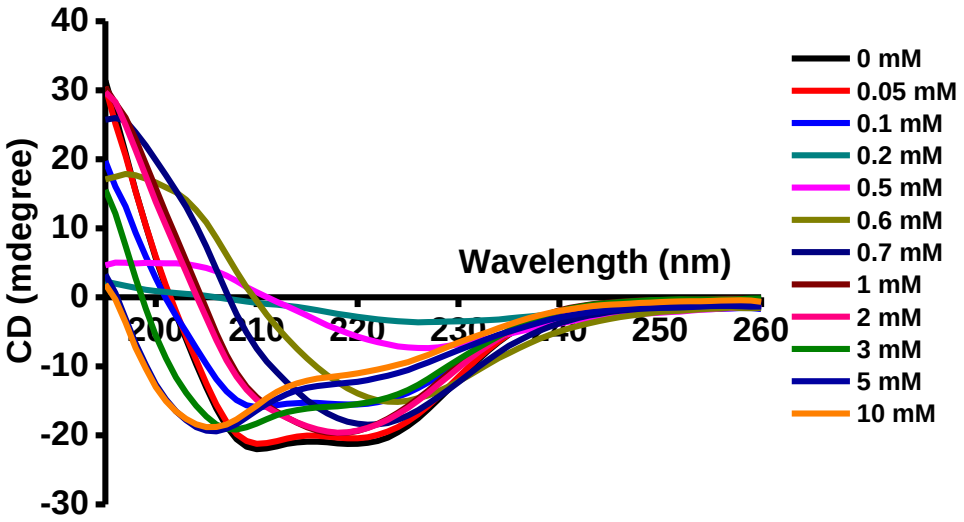

Figure 2.1 Far-UV CD spectra of human PrP 90-231 at varying concentrations of SDS (0-10 mM).

condition, PrP adopts a partially-disordered conformation comprising elements of helix and random-coil (Figure 2.2a). Since CD spectra provide information about the overall/global structural changes in a protein, we next monitored the local structural changes occurring predominantly in the N-terminal intrinsically disordered region of PrP (90-231) by utilizing the intrinsic tryptophan (Trp) fluorescence which is located at the residue position 99. It is well known that the Trp fluorescence emission spectrum is very sensitive to its local environment (43). The native PrP exhibited an emission maximum at 345 nm that is expected for a disordered region which is solvent-exposed and is plausibly significantly hydrated. In the presence of 1 mM SDS, the emission peak exhibited a 12 nm blue-shift indicating a structural ordering and compaction of the disordered N-terminal segment of PrP leading to a shielding of the Trp from the water molecules (Figure 2.2b). Next we carried out fluorescence anisotropy (43) measurements to further probe the alteration in the N-terminal segmental flexibility upon $\alpha \rightarrow \beta$ conformational switch. In the presence of 1 mM SDS, a sharp rise

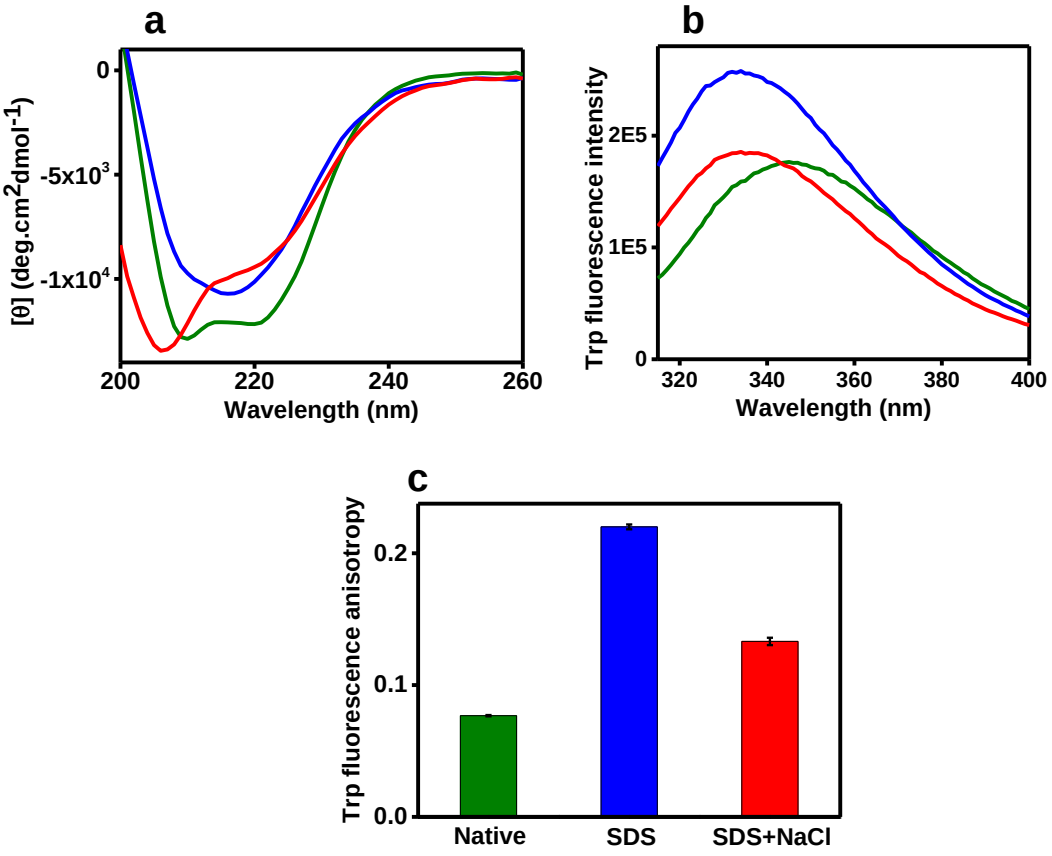

Figure 2.2 Far-UV CD spectra (a); Trp fluorescence emission spectra (b) and Trp fluorescence anisotropy (c) of 5 μM native wt-PrP (green) after treatment with 1 mM SDS (without NaCl) (blue) and with 250 mM NaCl (red).

in the Trp fluorescence anisotropy was observed indicating a structural compaction as a result of a disorder → order transition (Figure 2.2c) that corroborated the Trp spectral changes. Upon addition of salt, this region demonstrated lower anisotropy indicating enhanced flexibility compared to the β-rich state, but more rigid compared to the native state. Taken together, our CD and fluorescence results suggested that addition of salt and a sub-micellar concentration of SDS to PrP induces a structural transition from a predominantly α-helical to a partially-unstructured intermediate state comprising a significant proportion of disordered as well as helical components. We hypothesized that such chimeric conformers could serve as amyloidogenic precursors.

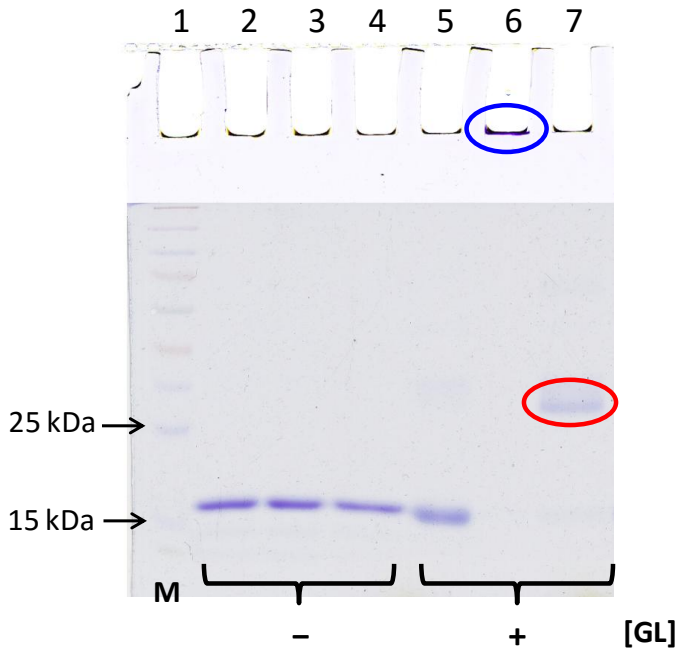

Figure 2.3 Glutaraldehyde cross-linking analysis of the SDS-β-oligomers and SDS-NaCl-induced PrP conformer. Native PrP (lane 2 and 5), SDS-β-oligomers (lane 3 and 6) and SDS-NaCl-induced PrP conformer (lane 4 and 7) (t = ~ 2 - 3 h) was treated with 0.05% glutaraldehyde (GL) and analyzed on SDS-PAGE (12.5%). The blue and red circles highlight formation of high molecular weight SDS-β-oligomers and SDS-NaCl-induced dimeric PrP conformer, respectively. 'M' on the left stands for molecular mass markers.

In order to investigate whether the SDS and SDS + salt-induced PrP conformers are aggregation-competent species, we carried out the glutaraldehyde cross-linking assay (Figure 2.3). The SDS-induced β-rich state exhibited high molecular weight species indicating the formation of large β-oligomers, whereas, in the presence of both the SDS and salt, partially-disordered conformer of PrP assembled predominantly into a dimeric species. Upon

prolonged incubation, this partially-disordered dimeric species converted into protease-resistant higher order aggregates as indicated by limited proteinase-K digestion assay (Figure 2.4c) and is consistent with a previous report on hamster PrP (36). However, the large β-oligomers remained unaltered and were susceptible to the digestion. . We also observed that both oligomeric isoforms exhibit differences in PK digestion pattern at low PK/PrP molar ratios (Figure 2.4a, b). Next, we used an amyloid-specific fluorescent dye namely Nile Red that has been shown to be more selective to amyloids compared to the commonly used amyloid markers such as Congo Red and thioflavin-T (47). Large β-oligomers exhibited

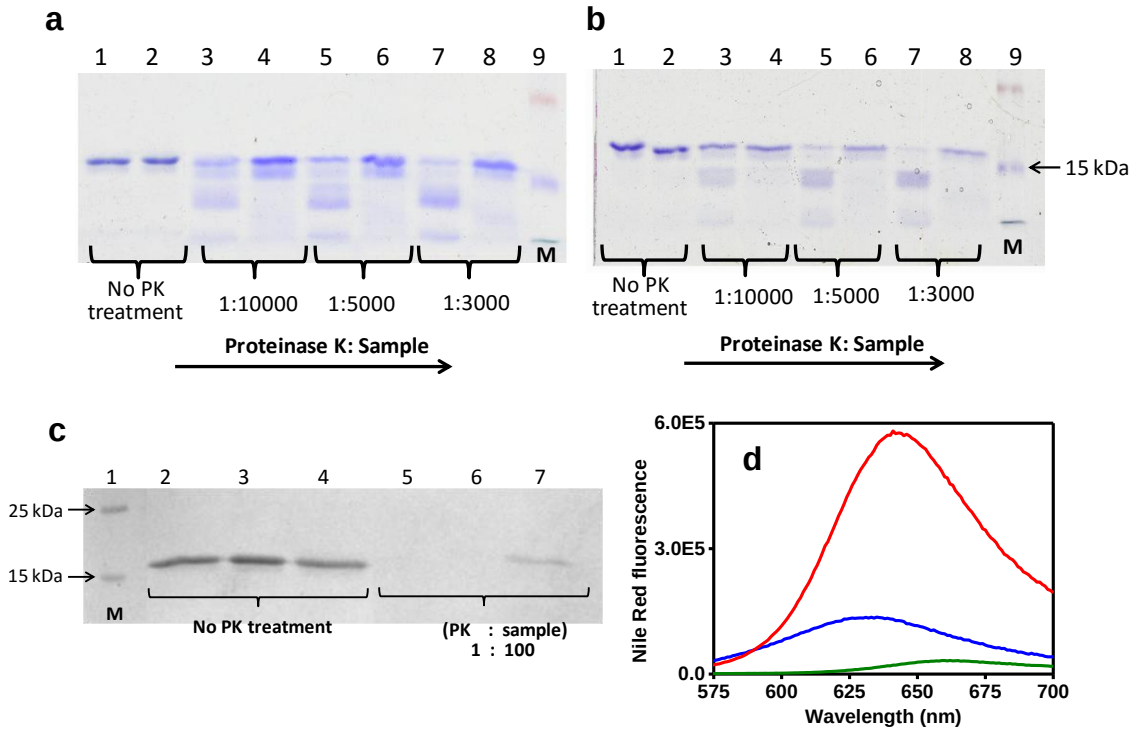

Figure 2.4 Proteinase K digestion of SDS-β-oligomers (a) and SDS-NaCl induced oligomers (b) at t = ~ 2 - 3 h. a) Lanes 1, 3, 5 and 7 shows the Native PrP shown as control and lanes 2, 4, 6 and 8 shows the SDS-β-oligomers treated with different concentrations of PK. b) Lanes 1, 3, 5 and 7 shows the Native PrP shown as control and lanes 2, 4, 6 and 8 shows the SDS-NaCl-oligomers treated with different concentrations of PK. PK treatment was done for 1 h at 37° C for all the isoforms of PrP. (c) Proteinase K (PK) digestion assay demonstrate the PK-resistant nature of SDS/NaCl-induced amyloid fibrils (~ 6 months old) (lane 7) whereas the SDS-induced β-oligomers (~ 2 months old) (lane 6) and native PrP (lane 5) were completely digested by PK treatment. Lane 2, 3 and 4 shows the native PrP, β-oligomers and fibrils, respectively, in the absence of PK treatment. 'M' on the left stands for molecular mass markers. (d) Changes in Nile red fluorescence emission spectra during amyloid formation. The red solid line represents evolution of Nile red fluorescence upon binding to SDS-NaCl-induced amyloid fibrils. The blue and green solid lines are for SDS-induced β-oligomers and native PrP, respectively.

much weaker increase in the Nile Red fluorescence as compared to the aggregates formed in the presence of SDS and salt (Figure 2.4d). These preliminary results indicate that the partially-unstructured dimeric state of PrP is the on-pathway species to amyloid assembly whereas the large β-oligomers are off-pathway species that did not convert into amyloidogenic species upon prolonged incubation. We next asked the question: What are the monomeric precursors to (off-pathway) β-oligomers and (on-pathway) amyloid-competent oligomers and whether they are structurally-distinguishable?

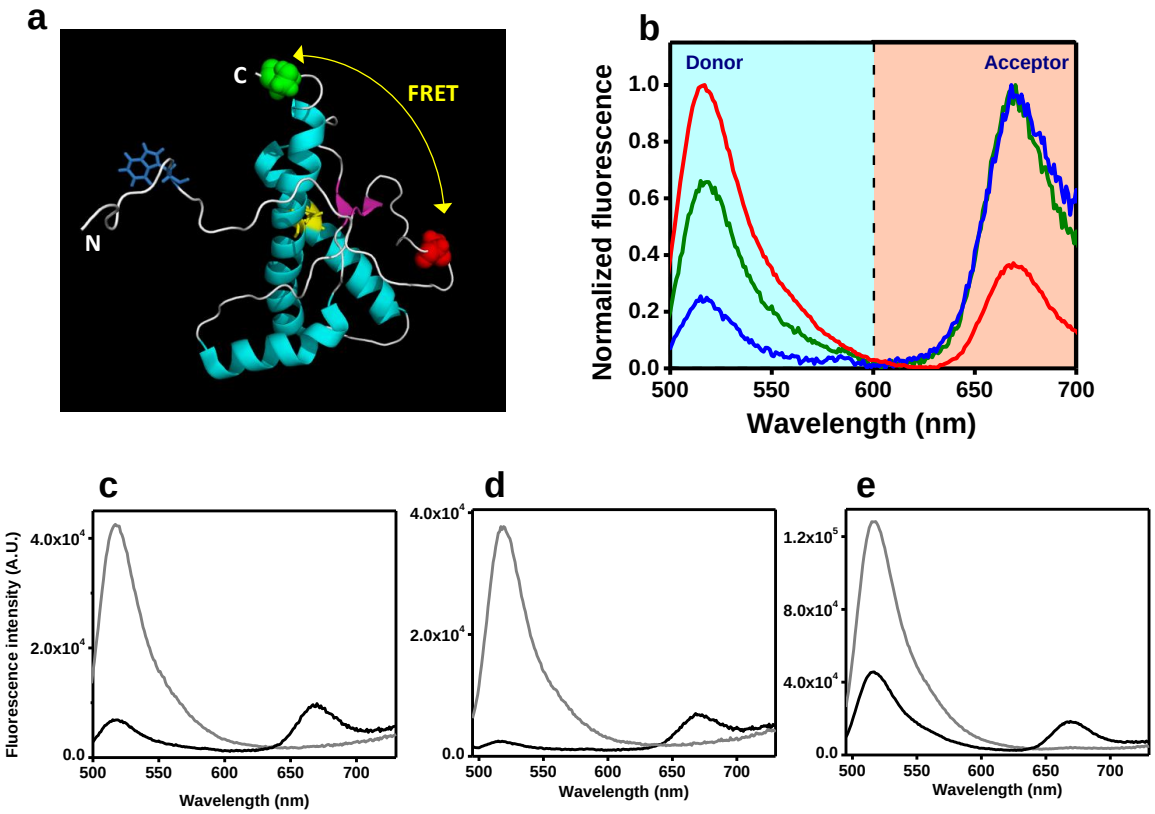

Figure 2.5 (a) The NMR structure of human PrP (90-231) (PDB ID: 2LSB) generated using PyMol (DeLano Scientific, CA). The single Trp and the disulfide are shown in blue and yellow, respectively. The red and green indicate the position of dual Cys mutations (A120C and S230C) that were labeled with AlexaFluor 488 (donor) and AlexaFluor 647 (acceptor) for FRET experiments. (b) Normalized FRET spectra of dual labeled PrP (50 nM) showing energy transfer in native PrP (green), immediately after treatment with SDS (blue) and SDS-NaCl (red) by exciting the donor. (c,d,e) Steady-state fluorescence emission spectra of FRET pair (AlexaFluor 488 (donor) and AlexaFluor 647 (acceptor) maleimides) labeled PrP, used to calculate the FRET efficiency under different conditions Native PrP (c), just after treatment with SDS without (d) and with NaCl (e). Spectra were acquired by exciting the donor (λ_{ex} = 488 nm). a-c) The grey solid line represent the spectra for donor only species and black solid line denotes the spectra of donor-acceptor dual labeled species (50 nM) under the respective conditions. FRET efficiency was estimated by the extent of donor fluorescence quenching in the presence of acceptor (Eq. 2.1).

In order to characterize the monomeric conformational states of PrP under oligomerization condition, we employed fluorescence resonance energy transfer (FRET). For carrying out FRET experiments, we generated a double cysteine (Cys) mutant of PrP (A120C/S230C) encompassing primarily the structured globular region of the protein (Figure 2.5a). After establishing that this dual Cys variant refolds into the native structure similar to the wild-type protein, we labeled Cys using bright thiol-active fluorescent AlexaFluor dyes that allowed us to monitor FRET at low sub-μM down to nM concentration to minimize the effect of protein aggregation. We labeled dual-Cys PrP using AlexaFluor 488 (donor) and AlexaFluor 647 (acceptor) maleimides and extensively purified to obtain the FRET construct. The FRET spectra were obtained by exciting the donor (AlexaFluor 488) and recording both donor and acceptor fluorescence (Figure 2.5b) and the FRET efficiencies were estimated using the extent of donor quenching in the presence of the acceptor (Figure 2.5). In the native state, PrP demonstrated high FRET efficiency (~80%) that is expected for an average intramolecular distance of ~35 Å (Figure 2.5). The FRET efficiency increased in the SDS-induced β-rich state (~94%) indicating more ordering leading to structural compaction. On the contrary, SDS and salt treatment yielded a low-FRET state (~60%) that provides a compelling evidence of conformational disorder in the early amyloidogenic intermediates. We conjecture that these early expanded and presumably short-lived monomeric amyloid-competent species slowly assemble and conformationally convert during the cascade of aggregation events. We next embarked upon studies aimed at characterizing the nanoscale morphology of the oligomeric, prefibrillar and fibrillar species during the course of PrP aggregation.

In order to watch the morphological transitions under aggregating conditions we utilized atomic force microscopy (AFM) that offers a sensitive and high-resolution tool to characterize the intriguing nanoscopic features at different stages of protein aggregation (48-51). Figure 2.6a and b show the AFM image and the size-distribution of the SDS-induced β-oligomers (in 5 μM wt-PrP), respectively suggesting that the average diameter of these spherical oligomers is ~9 nm. The size distribution remained unaltered even after prolonged incubation over 7 months reaffirming that these are off-pathway entities (Figure 2.6c). In a sharp contrast, the SDS + salt-induced partially-disordered PrP conformer at 5 μM concentration assembled into much smaller oligomers with an average height of ~3.5 nm (Figure 2.7a and b). These small oligomers are likely to be PrP-dimers as indicated by the glutaraldehyde cross-linking assay. Recently, single-molecule force spectroscopy has also revealed PrP dimerization as the initial event during PrP misfolding (20). These small

oligomers appear to be short-lived species and coalesce to form either higher-order oligomers or fibrils since longer incubation over 3-5 days afforded a population of larger oligomers with a variable size-distribution between 30 nm and 60 nm (Figure 2.7c). In addition, we observed the coexistence of short curly nascent protofibrils of height ~ 6 nm along with the spherical

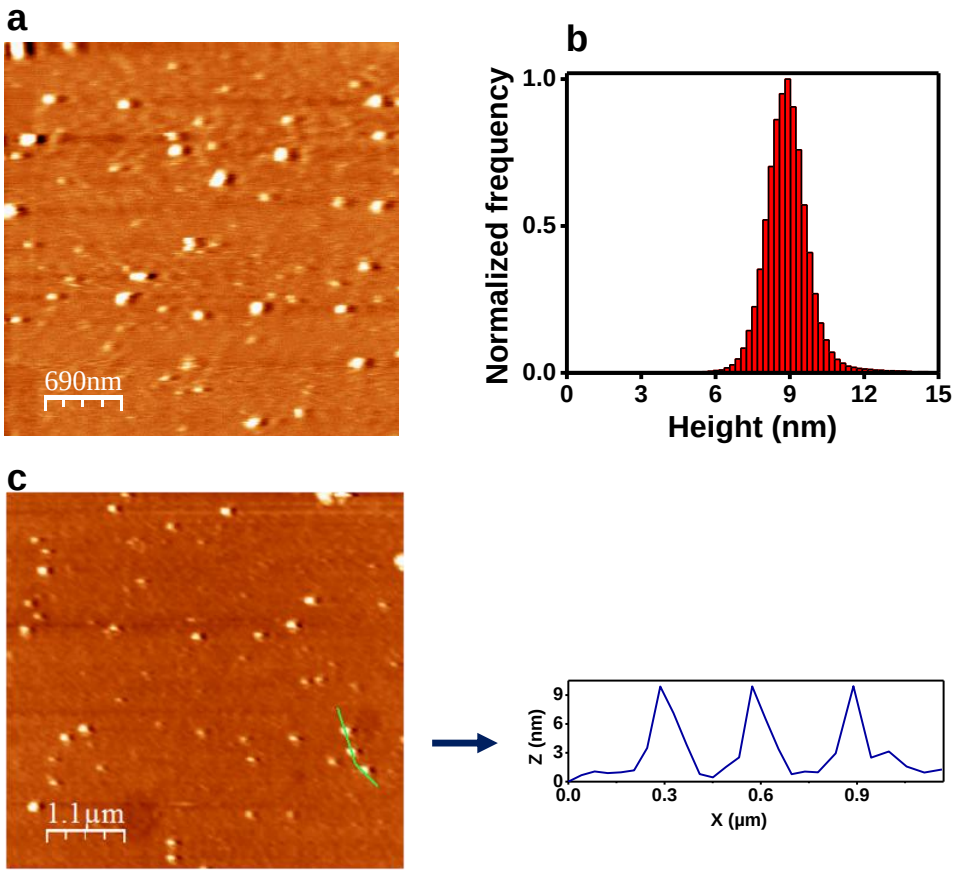

Figure 2.6 AFM images and the respective height distributions of SDS-induced large β-oligomers imaged immediately after mixing (a,b) and after 7 months (c). The height profile is shown in blue along the green lines. ([PrP] = 5 μM).

oligomers (Figure 2.7d). After establishing the existence of a heterogeneous population distribution of oligomers, we next steered our efforts to monitor the time-dependent evolution of morphologies over longer timescales. These experiments revealed the development of diverse nanoscale morphologies of amyloid fibrils over several days to weeks. The appearance of fibrils was spotted after 1 day along with the spherical oligomers. These fibrils were long, unbranched and wavy with a height of ~6 nm (Figure 2.8a). Fibrils obtained after 5 days were ~100 nm in height and displayed well-defined, thick, branched rod-like ultrastructure (Figure 2.8b), while those observed after an incubation period of 50 days lacked well-defined rod-like structure. Instead, these fibrils were arranged in a complex

mesh-like network with an average height of 10 nm (Figure 2.8c,d). Plausibly these fibrils were formed after the fragmentation of the larger aggregates observed at earlier times which resulted in the generation of secondary nucleation sites that yielded a mesh-like feature. At higher protein concentration (15 μM), the aggregation proceeded much faster and visual aggregates were seen within an hour. Imaging of the supernatant revealed the presence of long, unbranched, straight fibrils of ~40 nm in height that revealed a twisting pattern in the 3D image (Figure 2.8e). Overall, we were able to discern an extraordinary diversity in the nanostructural organization and morphology of PrP amyloids produced from small disordered oligomeric intermediates. We speculate that the generic differences between the tertiary packing of oligomers give rise to polymorphic nanofibrils. It is likely that the structurally

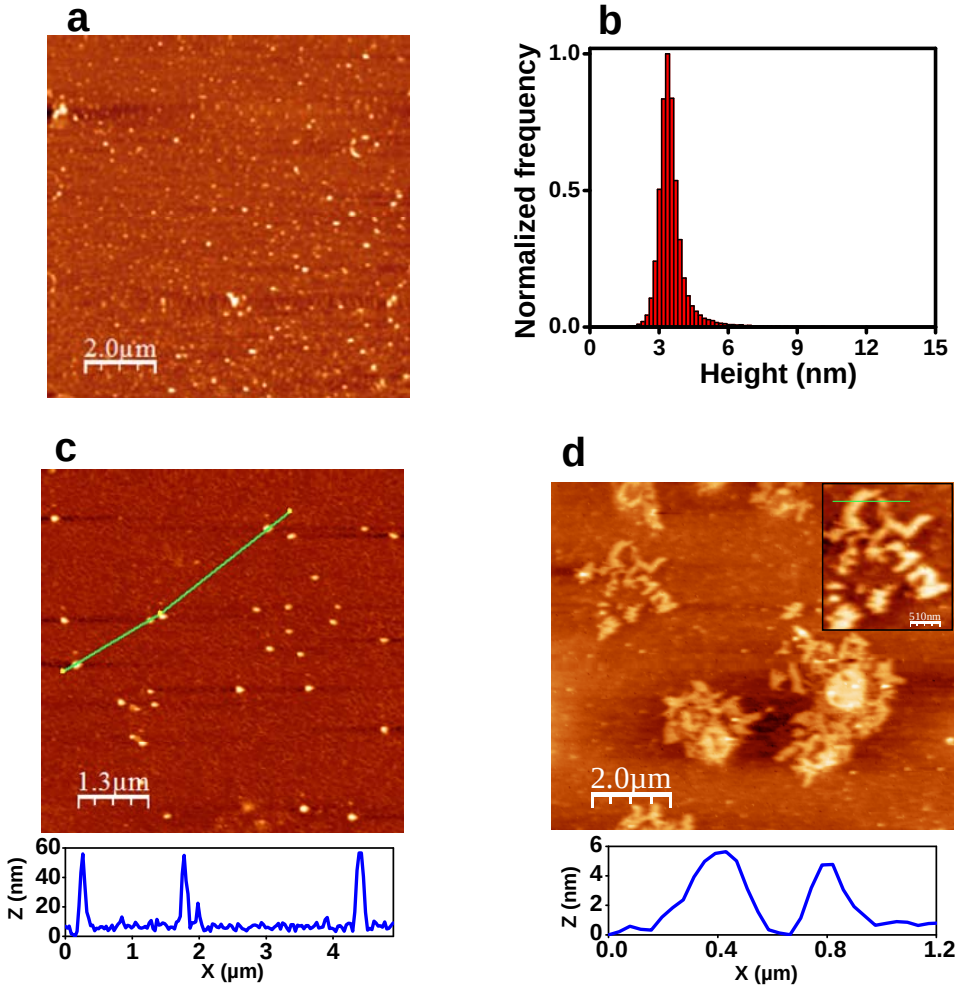

Figure 2.7 AFM images and the respective height distributions of SDS and salt induced small oligomers imaged immediately after mixing (a,b). SDS and salt induced smaller oligomers assorted into larger oligomers (5 days) (c) and the coexistence of short curly protofibrils (1 day) (d). The inset represents the magnified image. The height profile along the green lines is shown in blue ([PrP] = 5 μM).

labile oligomers formed at early stages can promote the association in a widely different fashion due to the inherent conformational plasticity of the polypeptide chain under

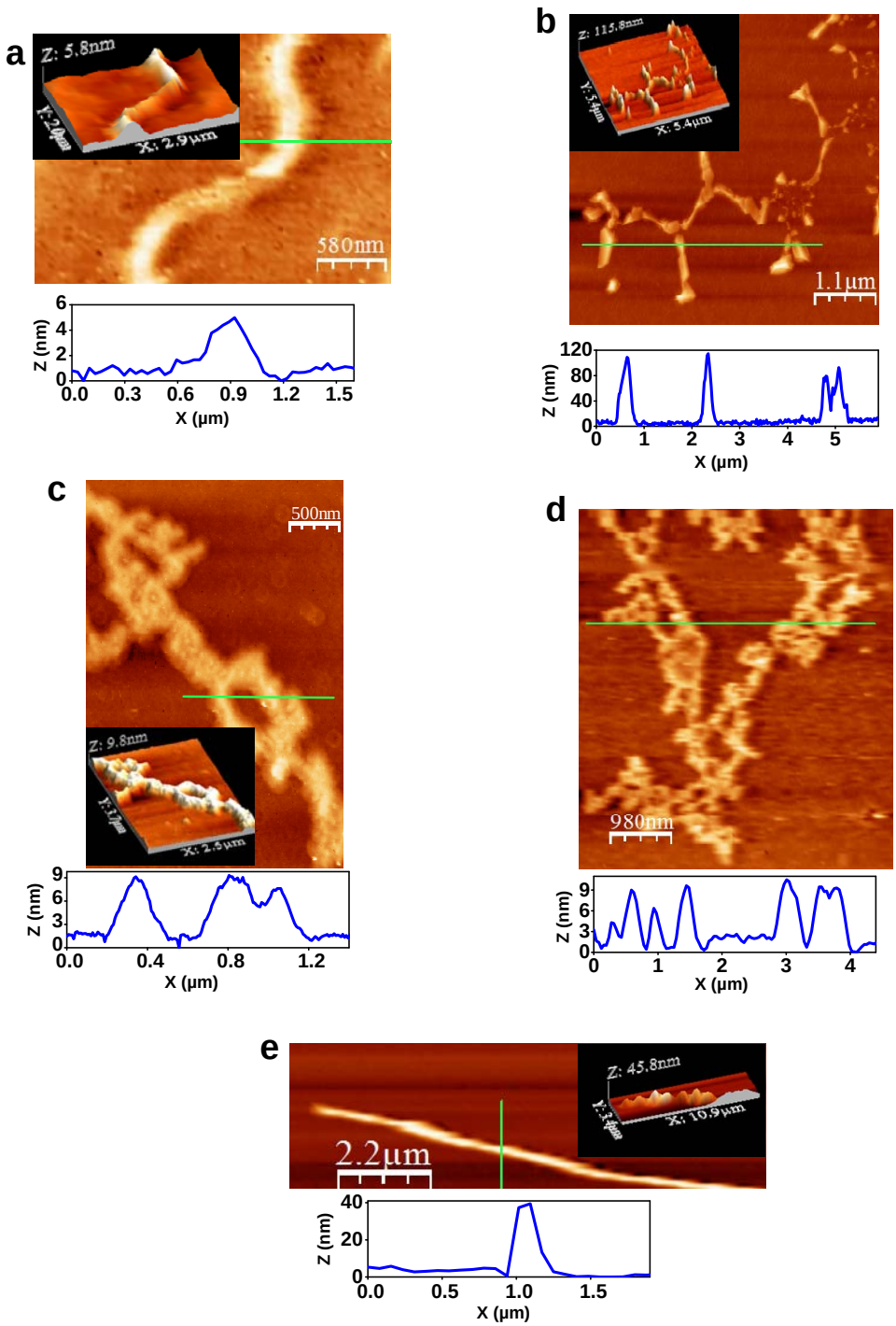

Figure 2.8 The topographic features of human PrP polymorphic amyloid nanostructures. AFM images reveal diversity in amyloid fibrillar morphologies on different days during the aggregation reaction (a: 1 day; b: 5 days ; (c, d): 50 days; (e:) 12 days at 15 µM PrP). The insets represent the 3D topography. The height profile is shown in blue along the green lines.

the amyloidogenic condition. On the contrary, well-structured and stable higher order β-oligomers lack the conformational plasticity to attain the propagating amyloidogenic form and therefore never matured to amyloid fibrils. These results underscore the importance of conformationally flexible critical oligomers as the (on-pathway) obligatory intermediate in the amyloid formation process. We next aimed at elucidating the structural organization of PrP within the oligomeric and fibrillar states.

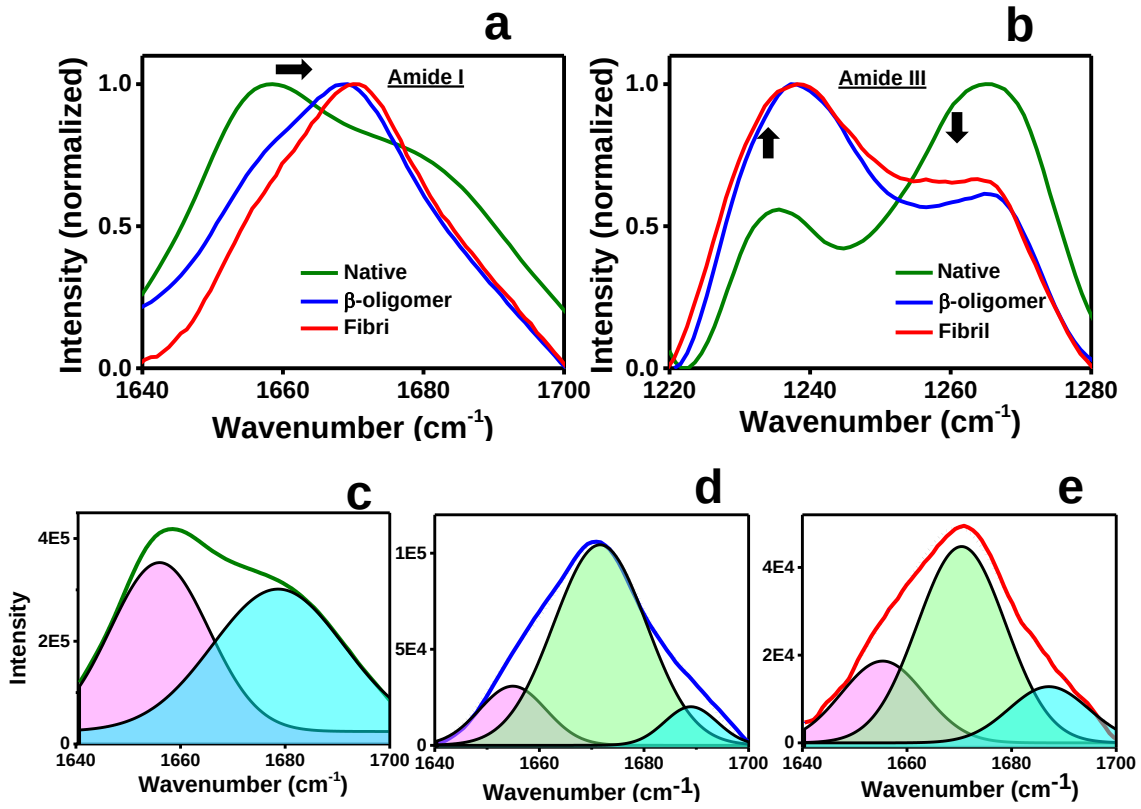

Figure 2.9 (a,b) Raman spectra of native PrP (green), β-oligomers (blue) and fibrils (red) showing the amide I (1640-1700 cm^{-1}) and amide III (1220-1280 cm^{-1}) regions. Both amide I and III indicate the transitions from α-helical to β-rich structure shown by arrows. (c-e) Deconvolution of amide I region indicates that predominantly α and random-coil (c: ~ 50% each in native) converts into β-rich states (d: 76% in β-oligomers; e: 56% in fibrils). The areas under the curves are indicated by magenta, green and cyan for α, β and random coils, respectively.

In order to decipher the protein conformational differences between the native PrP, β-oligomers and amyloid fibrils at the molecular level, we utilized vibrational Raman spectroscopy (46, 52-56). The changes in the backbone amides viz. amide I (1640-1700 cm^{-1}) and amide III (1220-1300 cm^{-1}) regions followed by their deconvolution allowed us to

estimate the contribution of various structural elements such as α-helix, β-sheet and random coils (Figure 2.9). Additionally, the changes in the side chains of several amino acids were monitored. The amide I peak at ~1658 cm^{-1} for native PrP shifted to ~1670 cm^{-1} during aggregation suggesting the structural transition from a predominantly α-helical to β-sheet-rich conformation (Figure 2.9a, c-e). The amyloid state has some elements of α-helix and random coil in addition to β-sheet. The peak at 1670 cm^{-1} is the hallmark of amyloid fold and is in good agreement with the amide I peak observed for PrP^{Sc}-enriched blood membrane fraction (53). Careful analysis of the amide III region depicted two major peaks at ~1236 cm^{-1} and ~1265 cm^{-1} that correspond to β-sheet and α-helix, respectively. For native PrP, a prominent peak at 1265 cm^{-1} was observed which dropped with a concomitant rise in the peak at 1236 cm^{-1} during amyloid assembly which is suggestive of an increase in β-sheet content at the expense of α-helices (Figure 2.9b). Also, the peak at 1236 cm^{-1} is likely to correspond to the hydrated β-sheet structure (55). Using an empirical relationship, we estimated the Ramachandran ψ dihedral angle based on the amide III peak observed at 1236 cm^{-1}(54). Assuming that the β-sheets are hydrated and might be involved in hydrogen bonding with water molecules in the vicinity, the value of amide III ψ dihedral angle recovered was ~ +134° which is suggestive of an antiparallel β-sheet structure (46). This value of dihedral angle agrees well with the results obtained for amyloid fibrils formed by Syrian hamster full length prion protein using deep ultraviolet resonance Raman spectroscopy (55). Additionally, a higher ratio of the Fermi doublet for tyrosines (850 cm^{-1}/830 cm^{-1}) (46) indicated enhanced hydrogen bonding in the amyloid state and is consistent with a recent Raman spectroscopic study on PrP^{Sc} (56).

We next asked the question: Do these PrP aggregates exhibit toxicity to mammalian cells? In order to investigate the cytotoxic effect, we carried out the MTT assay that is one of the most widely used assays to evaluate the cytotoxic effect and to determine the cell viability (57). HeLa cells were exogenously challenged with the PrP aggregates. Both β-oligomers and early (on-pathway) unstructured oligomers did not exhibit any major cytotoxic effects. On the other hand, protease-resistant amyloid fibrils were highly toxic to cells (Figure 2.10). The addition of amyloids resulted in death of ~ 65% cells (cell survival only ~35%; Figure 2.10a). The decrease in cell viability was also associated with a substantial alteration of cellular morphology such as cell shrinkage and increased cellular granularity and other hallmarks of cell death e.g. rounding of cells (Figure 2.10c). This set of studies indicated that the off-

pathway β-oligomers appear to be innocuous, whereas, PrP aggregates comprising the amyloid fold exhibit profound toxicity.

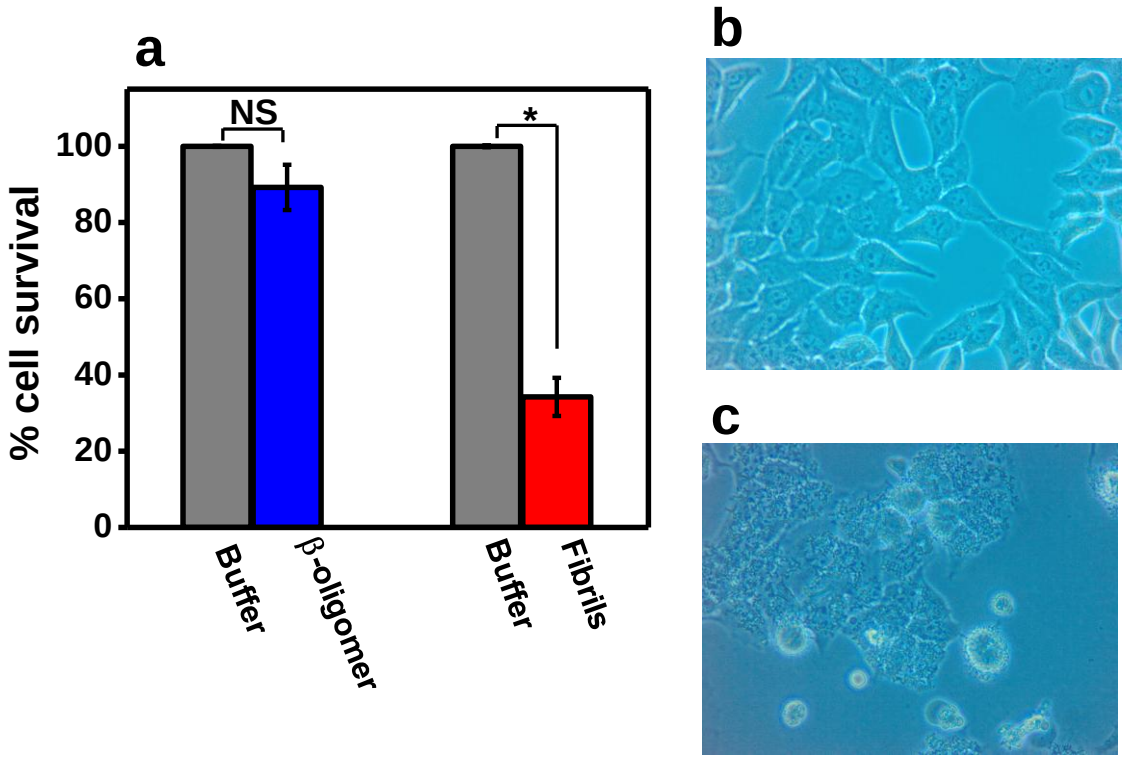

Figure 2.10 The toxic effect of PrP amyloids on HeLa cells. (a): MTT assay showing significant reduction in the cell viability upon treatment of cells with amyloids. Bars indicate mean ± SD and NS indicates non-significant difference in MTT reduction between treated cells with β-oligomers and control buffer. For amyloid sample: $*P < 0.0005$ (Student's t-test). (b,c): The phase contrast microscopy images (40x) demonstrate significant alteration of cellular morphology and cell death in the presence of PrP amyloids (c) compared to the control untreated cells (b).

2.4 CONCLUSION

Taken together, our results indicate the existence of two distinct pathways of human PrP misfolding and aggregation in the presence of anionic detergent that mimics the environment of anionic lipid membranes. A model depicted in Figure 2.11 summarizes the observations made from our experiments. We propose that PrP undergoes a profound conformational transition in the presence of SDS to form a compact β-rich state that readily assembles into

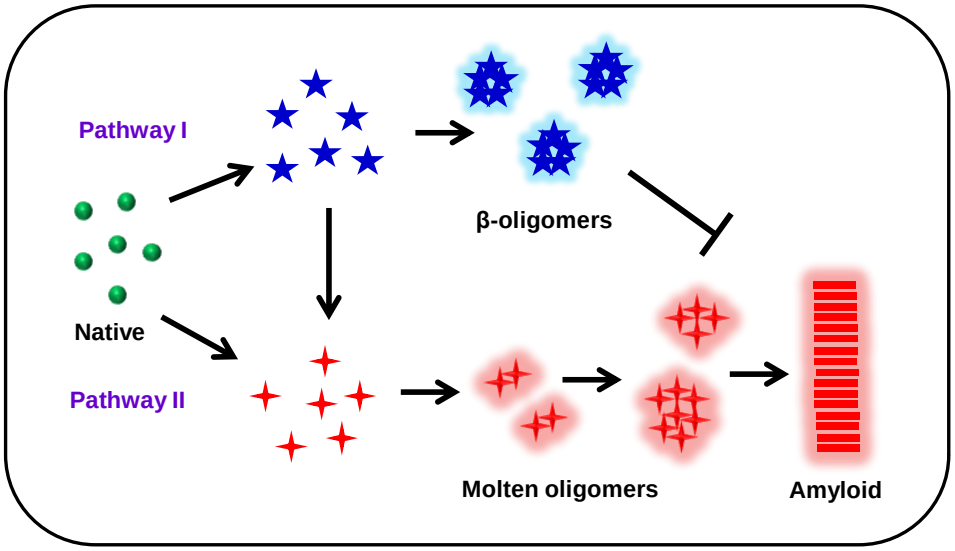

Figure 2.11 The proposed schematic model for PrP aggregation. SDS induces the formation of large, soluble, off-pathway β-oligomers (Pathway I). But, SDS in presence of salt leads to the formation of distinct ordered amyloid nanofibrils via a structurally-labile disordered oligomeric intermediate (Pathway II).

highly ordered β-oligomers. These oligomers, however, do not convert into amyloids and therefore represent an off-pathway intermediate. The occurrence of similar off-pathway, β-rich, fibril-incompetent oligomers had been reported under mild denaturing and low pH environment (27). However, in the presence of detergent and salt, PrP adopts a partially disordered state that associates into small (labile) molten oligomers, which eventually associate and conformationally mature into amyloids presumably *via* nucleated conformational conversion mechanism indicating the sequestration of amyloid folds in the context of oligomers (58-61) (Figure 2.12). These amyloids exhibit nanoscale polymorphism and we speculate that the varied fibril architecture is attributed to the heterogeneous ensemble of early obligatory oligomers. The morphological diversity of amyloids observed *in vitro* can have potential implications involving the existence of various PrP^{Sc} isoforms *in vivo* in the form of multiple prion strains at the intra-species level.

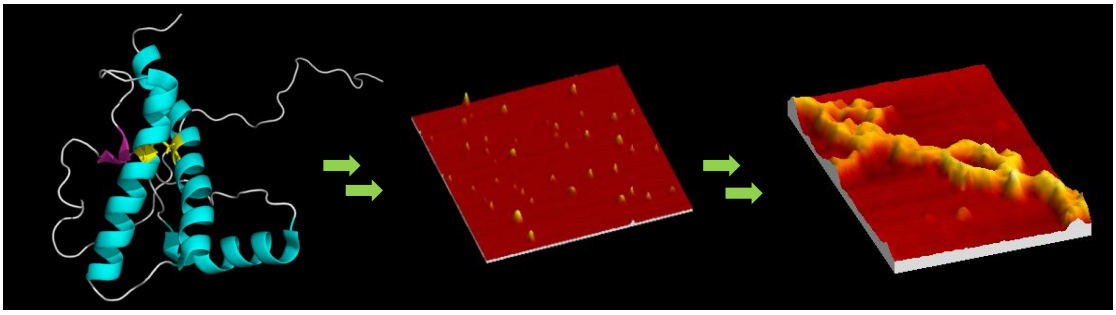

Figure 2.12 Conformational switching of PrP into protease resistant amyloid fibrils *via* oligomeric intermediates.

2.5 REFERENCES

1. Prusiner, S. B. (2004) *Prion biology and diseases*, Cold Spring Harbor Laboratory, Cold Spring Harbor, NY
2. Collinge, J. (2001) Prion diseases of humans and animals: their causes and molecular basis. *Annu. Rev. Neurosci.* **24,** 519-550
3. Cobb, N. J., Surewicz, W. K. (2009) Prion diseases and their biochemical mechanisms. *Biochemistry* **48**, 2574-85
4. Abid, K., and Soto, C. (2006) The intriguing prion disorders. *Cell Mol. Life Sc.* **63,** 2342-2351
5. Dearmond, S. J., McKinley, M. P., Barry, R. A., Braunfeld, M. B., McColloch, J. R., and Prusiner, S. B. (1985) Identification of prion amyloid filaments in scrapie-infected brain. *Cell* **41,** 221-235
6. Breydo, L., and Uversky, V. N. (2014) Molecular Mechanisms of Protein Misfolding. in *Bio-nanoimaging*, Academic Press, Boston. pp 1-14
7. Goedert, M. (2015) Alzheimer's and Parkinson's diseases: The prion concept in relation to assembled Abeta, tau, and alpha-synuclein. *Science* **349,** 1255555-1255559
8. Wang, F., Wang, X., Yuan, C.-G., and Ma, J. (2010) Generating a prion with bacterially expressed recombinant prion protein. *Science* **327,** 1132-1135
9. Wang, F., Yang, F., Hu, Y., Wang, X., Wang, X., Jin, C., and Ma, J. (2007) Lipid interaction converts prion protein to a PrPSc-like proteinase K-resistant conformation under physiological conditions. *Biochemistry* **46,** 7045-7053

10. Kocisko, D. A., Come, J. H., Priola, S. A., Chesebro, B., Raymond, G. J., Lansbury, P. T., and Caughey, B. (1994) Cell-free formation of protease-resistant prion protein. *Nature* **370,** 471-474
11. Kelly, J. W. (1998) The environmental dependency of protein folding best explains prion and amyloid diseases. *Proc. Natl. Acad. Sci. U.S.A.* **95,** 930-932
12. Diaz-Espinoza, R., Mukherjee, A., and Soto, C. (2012) Kosmotropic anions promote conversion of recombinant prion protein into a PrPSc-like misfolded form. *PLoS One* **7,** e31678
13. Breydo, L., and Uversky, V. N. (2015) Structural, morphological, and functional diversity of amyloid oligomers. *FEBS Lett*. 10.1016/j.febslet.2015.07.013
14. Singh, J., and Udgaonkar, J. B. (2015) Molecular Mechanism of the Misfolding and Oligomerization of the Prion Protein: Current Understanding and Its Implications. *Biochemistry* **54,** 4431-4442
15. Nystrom, S., and Hammarstrom, P. (2015) Generic amyloidogenicity of mammalian prion proteins from species susceptible and resistant to prions. *Sci. Rep.* **5,** 10101
16. Baskakov, I. V. (2004) Autocatalytic conversion of recombinant prion proteins displays a species barrier. *J. Biol. Chem.* **279,** 7671-7677
17. Frankenfield, K. N., Powers, E. T., and Kelly, J. W. (2005) Influence of the N-terminal domain on the aggregation properties of the prion protein. *Protein Sci.* **14,** 2154-2166
18. Khan, M. Q., Sweeting, B., Mulligan, V. K., Arslan, P. E., Cashman, N. R., Pai, E. F., and Chakrabartty, A. (2010) Prion disease susceptibility is affected by beta-structure folding propensity and local side-chain interactions in PrP. *Proc. Natl. Acad. Sci. U.S.A.* **107,** 19808-19813
19. Baskakov, I. V., Legname, G., Baldwin, M. A., Prusiner, S. B., and Cohen, F. E. (2002) Pathway complexity of prion protein assembly into amyloid. *J. Biol. Chem.* **277,** 21140-21148
20. Yu, H., Dee, D. R., Liu, X., Brigley, A. M., Sosova, I., and Woodside, M. T. (2015) Protein misfolding occurs by slow diffusion across multiple barriers in a rough energy landscape. *Proc. Natl. Acad. Sci. U.S.A.* **112,** 8308-8313
21. Zahn, R., Liu, A., Lührs, T., Riek, R., von Schroetter, C., López García, F., Billeter, M., Calzolai, L., Wider, G., and Wüthrich, K. (2000) NMR solution structure of the human prion protein. *Proc. Natl. Acad. Sci. U.S.A.* **97,** 145-150

22. Biljan, I., Giachin, G., Ilc, G., Zhukov, I., Plavec, J., and Legname, G. (2012) Structural basis for the protective effect of the human prion protein carrying the dominant-negative E219K polymorphism. *Biochem. J.* **446,** 243-251
23. Wille, H., Michelitsch, M. D., Guenebaut, V., Supattapone, S., Serban, A., Cohen, F. E., Agard, D. A., and Prusiner, S. B. (2002) Structural studies of the scrapie prion protein by electron crystallography. *Proc. Natl. Acad. Sci. U.S.A.* **99,** 3563-3568
24. Riesner, D. (2003) Biochemistry and structure of PrPC and PrPSc. *Br. Med. Bull.* **66,** 21-33
25. Sarnataro, D., Campana, V., Paladino, S., Stornaiuolo, M., Nitsch, L., and Zurzolo, C. (2004) PrP(C) association with lipid rafts in the early secretory pathway stabilizes its cellular conformation. *Mol. Biol. Cell.* **15,** 4031-4042
26. Morillas, M., Swietnicki, W., Gambetti, P., and Surewicz, W. K. (1999) Membrane environment alters the conformational structure of the recombinant human prion protein. *J. Biol. Chem.* **274,** 36859–36865
27. Caughey, B., Baron, G. S., Chesebro, B., and Jeffrey, M. (2009) Getting a grip on prions: oligomers, amyloids, and pathological membrane interactions. *Ann. Rev. Biochem.* **78,** 177-204
28. Lewis, V., and Hooper, N. M. (2011) The role of lipid rafts in prion protein biology. *Front. Biosci.* **16,** 151-168
29. Pinheiro, T. J. T. (2006) The role of rafts in the fibrillization and aggregation of prions. *Chem. Phys. Lipids.* **141,** 66-71
30. Deleault, N. R., Lucassen, R. W., an d Supattapone, S. (2003) RNA molecules stimulate prion protein conversion. *Nature* **425,** 717-720
31. Supattapone, S, (2014) Elucidating the role of cofactors in mammalian prion propagation. *Prion* **8,** 100-105
32. Ma, J. (2012) The role of cofactors in prion propagation and infectivity. *PLoS Pathog.* **8,** e1002589
33. Noble, G. P., Walsh, D. J., Miller, M. B., Jackson, W. S., and Supattapone, S. (2015) Requirements for mutant and wild-type prion protein misfolding in vitro. *Biochemistry* **54,** 1180-1187
34. Xiong, L.-w., Raymond, L.D., Hayes, S.F., Raymond. G.J., & Caughey, B. (2001) Conformational change, aggregation and fibril formation induced by detergent treatments of cellular prion protein. *J. Neurochem.* **79,** 669-678

35. Jansen, K., Schäfer, O., Birkmann, E., Post, K., Serban, H., Prusiner, S. B., and Riesner, D. (2001) Structural intermediates in the putative pathway from the cellular prion protein to the pathogenic form. *Biol. Chem.* **382,** 683-691

36. Stöhr, J., Weinmann, N., Wille, H., Kaimann, T., Nagel-Steger, L., Birkmann, E., Panza, G., Prusiner, S. B., Eigen, M., and Riesner, D. (2008) Mechanisms of prion protein assembly into amyloid. *Proc. Natl. Acad. Sci. U.S.A.* **105,** 2409-2414

37. Leffers, K.-W., Schell, J., Jansen, K., Lucassen, R., Kaimann, T., Nagel-Steger, L., Tatzelt, J., and Riesner, D. (2004) The structural transition of the prion protein into its pathogenic conformation is induced by unmasking hydrophobic sites. *J. Mol. Biol* **344,** 839-853

38. Leffers, K.-W., Wille, H., Stöhr, J., Junger, E., Prusiner, S. B., and Riesner, D. (2005) Assembly of natural and recombinant prion protein into fibrils. *Biol. Chem.* **386,** 569-580

39. Post, K., Pitschke, M., Schäfer, O., Wille, H., Appel, T. R., Kirsch, D., Mehlhorn, I., Serban, H., Prusiner, S. B., and Riesner, D. (1998) Rapid acquisition of beta-sheet structure in the prion protein prior to multimer formation. *Biol. Chem.* **379,** 1307-1317

40. Luers, L., Bannach, O., Stöhr, J., Wördehoff, M. M., Wolff, M., Nagel-Steger, L., Riesner, D., Willbold, D., and Birkmann, E. (2013) Seeded fibrillation as molecular basis of the species barrier in human prion diseases. *PLoS One* **8,** e72623

41. Atarashi, R., Moore, R. A., Sim, V. L., Hughson, A. G., Dorward, D. W., Onwubiko, H. A., Priola, S. A., and Caughey, B. (2007) Simplified ultrasensitive prion detection by recombinant PrP conversion with shaking. *Nat. Methods* **5,** 211-212

42. Mehlhorn, I., Groth, D., Stöckel, J., Moffat, B., Reilly, D., Yansura, D., Willett, W. S., Baldwin, M., Fletterick, R., Cohen, F. E., Vandlen, R., Henner, D., and Prusiner, S. B. (1996) High-level expression and characterization of a purified 142-residue polypeptide of the prion protein. *Biochemistry* **35,** 5528-5537

43. Lakowicz, J. (2006) Introduction to Fluorescence. *Principles of Fluorescence Spectroscopy*, Springer, US

44. Lindgren, M., Sorgjerd, K., and Hammarstrom, P. (2005) Detection and characterization of aggregates, prefibrillar amyloidogenic oligomers, and protofibrils using fluorescence spectroscopy. *Biophys. J.* **88,** 4200-4212

45. Horcas, I., Fernández, R., Gómez-Rodríguez, J. M., Colchero, J., Gómez-Herrero, J., and Baro, A. M. (2007) WSXM: a software for scanning probe microscopy and a tool for nanotechnology. *Review. Sci. Instrum.* **78,** 013705-013708

46. Bhattacharya, M., Jain, N., Dogra, P., Samai, S., and Mukhopadhyay, S. (2013) Nanoscopic Amyloid Pores Formed via Stepwise Protein Assembly. *J. Phys. Chem. Lett.* **4,** 480-485
47. Mishra, R., Sjolander, D., and Hammarstrom, P. (2011) Spectroscopic characterization of diverse amyloid fibrils in vitro by the fluorescent dye Nile red. *Mol. Biosyst.* **7,** 1232-1240
48. Adamcik, J., and Mezzenga, R. (2012) Study of amyloid fibrils via atomic force microscopy. *Curr. Opin. Colloid Interface Sci.* **17,** 369-376
49. Gosal, W. S., Myers, S. L., Radford, S. E., and Thomson, N. H. (2006) Amyloid under the atomic force microscope. *Protein Pept. Lett.* **13,** 61-270
50. Volpatti, L. R., Vendruscolo, M., Dobson, C. M., and Knowles, T. P. (2013) A clear view of polymorphism, twist, and chirality in amyloid fibril formation. *ACS Nano* **7,** 10443-10448
51. Ruggeri, F. S., Adamcik, J., Jeong, J. S., Lashuel, H. A., Mezzenga, R., and Dietler, G. (2015) Influence of the beta-sheet content on the mechanical properties of aggregates during amyloid fibrillization. *Angew. Chem. Int. Ed.* **54,** 2462-2466
52. Tuma, R. (2005) Raman spectroscopy of proteins: from peptides to large assemblies. *J. Raman Spectrosc.* **36,** 307-319
53. Carmona, P., Monleón, E., Monzón, M., Badiola, J. J., and Monreal, J. (2004) Raman analysis of prion protein in blood cell membranes from naturally affected scrapie sheep. *Chem. Biol.* **11,** 759-764
54. Mikhonin, A. V., Bykov, S. V., Myshakina, N. S., and Asher, S. A. (2006) Peptide secondary structure folding reaction coordinate: correlation between uv raman amide III frequency, Psi Ramachandran angle, and hydrogen bonding. *J. Phys. Chem. B* **110,** 1928-1943
55. Shashilov, V., Xu, M., Makarava, N., Savtchenko, R., Baskakov, I. V., and Lednev, I. K. (2012) Dissecting structure of prion amyloid fibrils by hydrogen-deuterium exchange ultraviolet Raman spectroscopy. *J. Phys. Chem. B* **116,** 7926-7930
56. Noble, G. P., Wang, D. W., Walsh, D. J., Barone, J. R., Miller, M. B., Nishina, K. A., Li, S., and Supattapone, S. (2015) A Structural and Functional Comparison Between Infectious and Non-Infectious Autocatalytic Recombinant PrP Conformers. *PLoS Pathog.* **11,** e1005017
57. Reixach, N., Deechongkit, S., Jiang, X., Kelly, J. W., and Buxbaum, J. N. (2004) Tissue damage in the amyloidoses: Transthyretin monomers and nonnative oligomers

are the major cytotoxic species in tissue culture. *Proc. Natl. Acad. Sci. U.S.A.* **101,** 2817-2822

58. Serio, T. R., Cashikar, A. G., Kowal, A. S., Sawicki, G. J., Moslehi, J. J., Serpell, L., Arnsdorf, M. F., and Lindquist, S. L. (2000) Nucleated conformational conversion and the replication of conformational information by a prion determinant. *Science* **289,** 1317-1321
59. Pappu, R. V., Wang, X., Vitalis, A., and Crick, S. L. (2008) A polymer physics perspective on driving forces and mechanisms for protein aggregation. *Arch. Biochem. Biophys.* **469,** 132-141
60. Vitalis, A., and Pappu, R. V. (2011) Assessing the contribution of heterogeneous distributions of oligomers to aggregation mechanisms of polyglutamine peptides. *Biophys. Chem.* **159,** 14-23
61. Lee, J., Culyba, E. K., Powers, E. T., and Kelly, J. W. (2011) Amyloid-beta forms fibrils by nucleated conformational conversion of oligomers. *Nat. Chem. Biol.* **7,** 602-609

Chapter 3

Investigation of Ordered Water within the Oligomers of the Human Prion Protein

3.1 INTRODUCTION

Prions are proteinaceous infectious agents that cause invariably fatal neurodegenerative disorders in humans and animals (1-3). This class of diseases is classified as transmissible spongiform encephalopathies (TSE) that include Kuru, fatal familial insomnia and Creutzfeldt-Jakob disease in humans, bovine spongiform encephalopathies, chronic wasting disease in deer and elk and scrapie in sheep and goat (4). These pathologies are manifested in genetic, infectious and sporadic manner (5). The etiology of the disease is explained by the protein-only hypothesis according to which the conformational conversion of cellular normal prion protein (PrP^{C}) into the disease causing scrapie isoform (PrP^{Sc}) signals the onset of the pathology (6,7).

PrP^{C} is a glycoprotein anchored to the cell-surface via phosphoinositol glycosyl (GPI) anchor and particularly expressed by neuronal cells (8,9). Its structured domain (residues 126 to 231) is comprised of three α-helices and two short antiparallel β-sheets (10,11) (Figure 3.1a). The conformational transition event results in profound changes not only in the structural and biochemical characteristics but also in the physiological properties of the prion protein. PrP^{C} is α-helical, monomeric, protease sensitive and detergent soluble. While, PrP^{Sc} is β-sheet, aggregated, detergent insoluble and has a protease-resistant core (12). Proteinase-K (PK) treatment of PrP^{Sc} leads to the generation of a protease-resistant fragment termed as PrP27-30 comprising residues 90-231. This fragment is considered as the major infective unit that recapitulates all the features of PrP^{Sc} (13).

Bacterially expressed recombinant PrP (rPrP) has been widely used to investigate the structural conversion event under varied *in vitro* formulated conditions e.g. mild denaturants (urea/guanidinium chloride), high temperature or pressure and low pH (14-20). Since, PrP is cell membrane-anchored, lipids and various lipid mimetic surfactants e.g. sodium dodecyl sulfate (SDS) are known to play a pivotal role in inducing the formation of PK resistant pathogenic conformation (rPrP-res) that is considered analogous to PrP^{Sc} (21-28). Despite of extensive research, the definitive cause behind the conformational switching and origin of PrP^{Sc} is poorly understood. As proteins structure and function have evolved in water 'the milieu of life'. The water molecules encapsulating the protein surface make up the hydration shell and termed as biological water (29,30). A myriad of studies have indicated that water cannot be treated as an inert solvent and firmly states the importance of biological water and its coupling with protein motions effect there conformational and functional dynamics (31). Molecular dynamics (MD) simulation analysis point out the unique hydration properties of

the PrP^C (32-34). Among all the soluble proteins in the PDB, PrP^C has the largest number of defectively wrapped backbone hydrogen bonds vulnerable to water interaction and thus represent the structurally labile regions with a propensity of unfolding and aggregation. Moreover, these studies also emphasize that underdehydrated hydrogen bonds i.e. the regions poorly defended against water attack by flanking nonpolar residues (helix 1, helix 2-helix 3 loop, helix 3 C terminus) are pervasive reactive sites for interaction with lipid membranes (33,34). The sensitivity and destabilization of native PrP structure to temperature, pressure and pH also purports the fundamental role of hydration in the misfolding and aggregation. In compliance, high pressure perturbation calorimetry studies have shown the differences in hydration pattern of the β-rPrP aggregates and native PrP (17).

The key aspect of prion aggregation is the evolution of oligomers from monomeric PrP and the growing body of evidences considers early oligomers as the prime agent initiating the neurodegeneration (35). The fluctuations of water molecules in the hydration layer of proteins mediate several vital functions like biomolecular recognition, protein-protein interaction and self assembly into aggregates (36,37). Thus, it is of great importance to comprehend the elusive role of water in prion aggregation. We have investigated the conformational conversion and oligomerization of the human prion protein (90-231) under previously defined membrane mimetic physiological conditions. Pertinent to above observations, we aim to understand the role of solvation dynamics in the interfacial hydration layer encapsulating the PrP in the oligomeric assemblies. Our experimental results bring forward the various conformational and hydration aspects of prion misfolding and dissect out the role of solvation dynamics in the oligomers at the molecular level. Along with this, we will also discuss the key salient features distinguishing the structural packing of off-pathway β-oligomers and structurally labile disordered on-pathway oligomers. We propose that in contrast to off-pathway β-oligomers, the formation of disordered on-pathway oligomers is energetically favored and stabilized by the preferential site specific hydration.

3.2 EXPERIMENTAL SECTION

3.2.1 Materials

All the reagents used for different preparations were purchased from Sigma (St. Louis, MO), unless otherwise mentioned and were of the highest purity grade. 5-((((2-iodoacetyl)amino)ethyl)amino) naphthalene-1-sulfonic acid (IAEDANS) and 6-Acryloyl-2 (dimethylamino) naphthalene (acrylodan) were obtained from Molecular Probes, Invitrogen. The pH of the buffers was adjusted on a Metrohm 827 lab pH meter at room temperature.

3.2.2 Protein expression, purification and labeling

The expression and purification of recombinant human prion protein 90-231 was carried out as described earlier. The single cysteine mutants of human prion protein, S230C and A120C, were generated using QuikChange® site-directed mutagenesis kit (Stratagene). The purity of the protein was checked by sodium dodecyl sulfate-polyacrylamide gel electrophoresis. The cysteine variants (S230C and A120C) were labeled with IAEDANS under denaturing conditions at pH 8 using 14-fold excess of the dye. Acrylodan labeling of S230C variant was carried out at pH 7.2 using 17-fold excess of dye. The fluorescent dyes were added in aliquots and the reaction was carried out at room temperature for 4 hours. PD-10 column (GE Healthcare) was used for removal of the free dye and for refolding of the protein.

3.2.3 Oligomer preparation

For all the experiments, the stock solution of the protein was prepared fresh and diluted to the final protein concentration of 5 μM in 5mM phosphate buffer (pH 7.2). Off-pathway β-rich oligomers were generated immediately after treating the protein with 1 mM sodium dodecyl sulfate (SDS). Whereas, on-pathway disordered oligomers were generated immediately after treating the protein with 1 mM SDS and 250 mM sodium chloride (NaCl).

3.2.4 Steady state fluorescence measurements

Steady state fluorescence measurements were performed on Fluoromax-4 (Horiba Jobin Yvon, NJ). The tryptophan fluorescence quenching experiment was performed using acrylamide as a quencher. The Trp fluorescence intensity was recorded as a function of acrylamide concentration under different conditions viz. native, off-pathway SDS-induced oligomers and on-pathway SDS NaCl-induced disordered oligomers. The quenching graphs

were plotted and fitted to estimate the Stern-Volmer constant (K_{sv}) that was further used to determine the bimolecular quenching rate constant (k_q) using the following relationship:

$$F_0/F = 1 + K_{sv}[Q] \quad (3.1a)$$

$$K_{sv} = \tau_o\, k_q \quad (3.1b)$$

where, F_0 and F represent the fluorescence intensity in absence and presence of quencher, τ_o is the Trp fluorescence lifetime in the absence of quencher and [Q] stand for the molar concentration of the quencher. AEDANS fluorescence was monitored using 375 nm excitation wavelength keeping excitation slit width at 0.5 nm and λ_{em} (range) = 400 nm – 550 nm and λ_{em} slit width was 2 nm. For 1,8-anilinonaphthalene-sulfonic acid-ammonium salt (ANS) fluorescence the parameters were adjusted to: λ_{ex} = 350 nm, λ_{ex} slit width = 1 nm and λ_{em} (range) = 430 nm – 620 nm with λ_{em} slit width = 6 nm. And the acrylodan fluorescence was collected using: λ_{ex} = 375 nm, λ_{ex} slit width = 1 nm and λ_{em} (range) = 440 nm – 600 nm with λ_{em} slit width = 2 nm. The presented fluorescence spectra were collected at 0.5 s integration time and averaged over three accumulations. Steady state fluorescence anisotropy (r_{ss}) was estimated for ANS and AEDANS using the following relationship:

$$r_{ss} = (I_{||} - I_{\perp} G) / (I_{||} - 2\, I_{\perp} G) \quad (3.2)$$

where, $I_{||}$ and $I_{\perp}$ are fluorescence intensities collected using parallel and perpendicular geometry of the polarizer, respectively and the perpendicular components were corrected using a G-factor ([55]). For ANS and AEDANS fluorescence anisotropy following parameters were adjusted: λ_{ex} (ANS) = 350 nm and λ_{em} = 480 nm, λ excitation and emission slit widths were 5.5 nm and 8 nm, respectively. λ_{ex} (AEDANS) = 350 nm and λ_{em} = 490 nm and λ excitation and emission slit widths were 3 nm and 5 nm, respectively.

3.2.5 Time-resolved fluorescence measurements

The time-resolved measurements were performed using time-correlated single photon counting (TCSPC) setup (Fluorocube, Horiba Jobin Yvon, NJ). The peak count was fixed to 10000 for fluorescence lifetime with excitation and emission polarizer orientation at magic angle (54.7°). For fluorescence anisotropy decay, the peak difference was 10000 counts and the orientation of emission polarizer was toggled between 0° and 90° with respect to the excitation polarizer (0°) for parallel fluorescence intensities ($I_{\parallel}$) and perpendicular fluorescence intensities ($I_{\perp}$), respectively. The instrument response function (IRF) was

collected using Ludox (colloidal silica). For AEDANS, 375 nm laser diode (LD) was used as the excitation source and 500 nm as emission wavelength. The bandpass was 6 nm for lifetime and 8 nm for anisotropy. The width (FWHM) of IRF was ~ 275 ps. The fluorescence intensity decay plots were analyzed taking the IRF into account using $I(t) = \sum_i \alpha_i e^{-t/\tau i}$, where α_i and τ_i represent the amplitude and lifetime of the different lifetime components, respectively. The parameters obtained from lifetime data analysis were then used as input for the anisotropy decay analysis. The analysis of anisotropy decay curves was done by globally fitting the $I_{\parallel}(t)$ and $I_{\perp}(t)$ using the following equations:

$$I_{\parallel}(t) = I(t)[1+2\,r(t)]/3 \qquad (3.3a)$$

$$I_{\perp}(t) = I(t)[1-r(t)]/3 \qquad (3.3b)$$

where $I_{\parallel}(t)$ and $I_{\perp}(t)$ represent the parallel and perpendicular fluorescence intensities, respectively. $I(t)$ represents the fluorescence intensity at magic angle (54.7°) and $r(t)$ represents the anisotropy decay function. The perpendicular fluorescence intensities were always corrected for g-factor which was obtained by taking free dye in a non-viscous medium. The anisotropy decays were then analyzed using a biexponential anisotropy decay function that describes the fast and slow motion of a fluorophore.

$$r(t) = r(0)\,[\beta_{fast} \exp(-t/\phi_{fast}) + \beta_{slow} \exp(-t/\phi_{slow})] \qquad (4)$$

where $r(0)$ represents the intrinsic anisotropy of a fluorophore; ϕ_{fast} and ϕ_{slow} represent the fast and slow rotational correlation time, respectively with β_{fast} and β_{slow} as their respective amplitudes ([55]). For estimation of $r(0)$ for AEDANS, it was taken in 100% glycerol. The $r(0)$ obtained was used for analyzing the anisotropy data with a window of ~ ±0.005. The slow correlation time accounts for the global motion of a fluorophore and can be used for estimating the size of a molecule using Stokes-Einstein relationship given by,

$$\phi_{slow} = \eta V/kT \qquad (5a)$$

where η is the viscosity, k is the Boltzmann constant, T is the temperature which was kept as 25 °C for all the experiments and V is the molecular volume given by

$$V = 4/3\,\pi\,R_h^3 \qquad (5b)$$

where R_h is the hydrodynamic radius of the molecule.

For the time-resolved emission spectra (TRES) measurements S230C variant labeled with acrylodan was used. To construct the TRES spectra, the time-resolved fluorescence decays of the samples were collected at different emission wavelengths ranging from 440 nm to 600 nm at an interval of 10 nm and an emission bandpass of 8 nm. The intensity decays were deconvoluted using the IRF and analyzed with the help of DAS6 software provided with the TCSPC system. To obtain TRES, the fitting parameters were then normalized with respect to the steady-state fluorescence intensity that was obtained from the steady-state fluorescence spectrum. The resulting time-resolved spectra were then normalized and fitted with a Lognormal or Lorentz shape function to estimate the peak frequency ν(t) as a function of time. The solvation correlation function (C(t)) is calculated using the following relationship:

$$C(t) = [\nu(t) - \nu(\infty)]/ [\nu(0) - \nu(\infty)] \qquad (3.6a)$$

where ν(0), ν(t), and ν(∞) denote the emission peak frequencies at time 0, t, and infinity, respectively. The correlation function was then fitted using a single exponential function as following:

$$C(t) = \exp(-t/\tau_s) \qquad (3.6b)$$

where the time constant (τ_s) of the decay represents the solvation time.

3.2.6 Atomic force microscopy

The AFM imaging was carried out on MultiView 2000^{TM} instrument (Nanonics Imaging Ltd., Jerusalem, Israel) operating in intermittent contact mode based on phase feedback as described previously. In brief, for AFM imaging oligomers sample just was treatment of protein with SDS/SDS-NaCl was deposited onto freshly cleaved muscovite mica (Grade V-4 mica from SPI, PA) and incubated for 30 minutes. Following, mica was washed with filtered water and dried under nitrogen. AFM images of 256 x 256 pixels or 400 x 400 pixels were collected with sample a delay of 6 ms and 4 ms, respectively. The acquired AFM images were processed using WSxM version 4 develop 11.6 software provided with the AFM setup.

3.3 RESULTS AND DISCUSSION

In the previous chapter, we showed that in the presence of SDS, human PrP (90-231) aggregation occurs by two alternate pathways and is governed by the presence/absence of 250 mM sodium chloride. PrP is immediately transformed into off-pathway β-oligomers upon treatment with 1 mM SDS (no salt). On the contrary, in the presence of salt it adopts a

partially disordered (alpha helical + random coil) state (Figure 3.1b inset) that repersents the structurally labile on-pathway oligomers which matures into polymorphic amyloid fibrils. In the present study, we have addressed a key issue: what are the conformational and physical factors that lead to two heterologous oligomeric species in the presence of SDS? We have approached this problem in a stepwise probe-dependent manner and monitored the various striking conformational features that distinguished the off-/on-pathway oligomers. In conjunction, we have also discerned the hydration properties of these divergent oligomers.

3.3.1 Spectroscopic analysis of conformational differences between β-oligomers and disordered oligomers

Human PrP (90 - 231) contains single tryptophan in the N-terminus unstructured region at residue position 99 (Figure 3.1a). Given the fact that, Trp fluorescence properties are highly dependent on its local environment, it is the most convenient intrinsic spectroscopic probe to follow the protein structural changes (38). Taking the advantage of the only Trp we carried out fluorescence quenching experiments and probed the surface accessibility of Trp using acrylamide as a quencher. In the native PrP Trp positioned in the unstructured region, is exposed to the solvent and thus, accessible to the quencher; it was easily quenched resulting in the highest value of bimolecular quenching rate constant ($k_q \sim 5.12 \times 10^9$ $M^{-1}s^{-1}$). The extent of quenching of a fluorophore is given by the value of bimolecular quenching rate constant (k_q) which that reflects the sensitivity of Trp to the quencher, higher k_q means Trp is on the surface and lower k_q values indicate Trp is inaccessible and buried. In the SDS-induced β-oligomers Trp quenching efficiency was lower ($k_q \sim 1.36 \times 10^9$ $M^{-1}s^{-1}$) indicating that Trp is more protected from solvent accessibility. However, in the SDS-NaCl induced disordered on-pathway oligomers quencher could penetrate easily and exhibit intermediate quenching of Trp ($k_q \sim 3.30 \times 10^9$ $M^{-1}s^{-1}$) (Figure 3.1b). Thus, in the disordered oligomers the Trp is only minimally protected compared to the native PrP. Next, to follow the local structural changes occurring in other unstructured flexible regions of PrP, we have selectively engineered two single cysteine mutants, A120C and S230C. These two mutations encompass the structured domain of PrP that extends from residue 126 till 228 (Figure 3.1a). Cys were labeled with a small, microenvironment sensitive dansyl based fluorophore, 5-((((2-iodoacetyl)amino)-

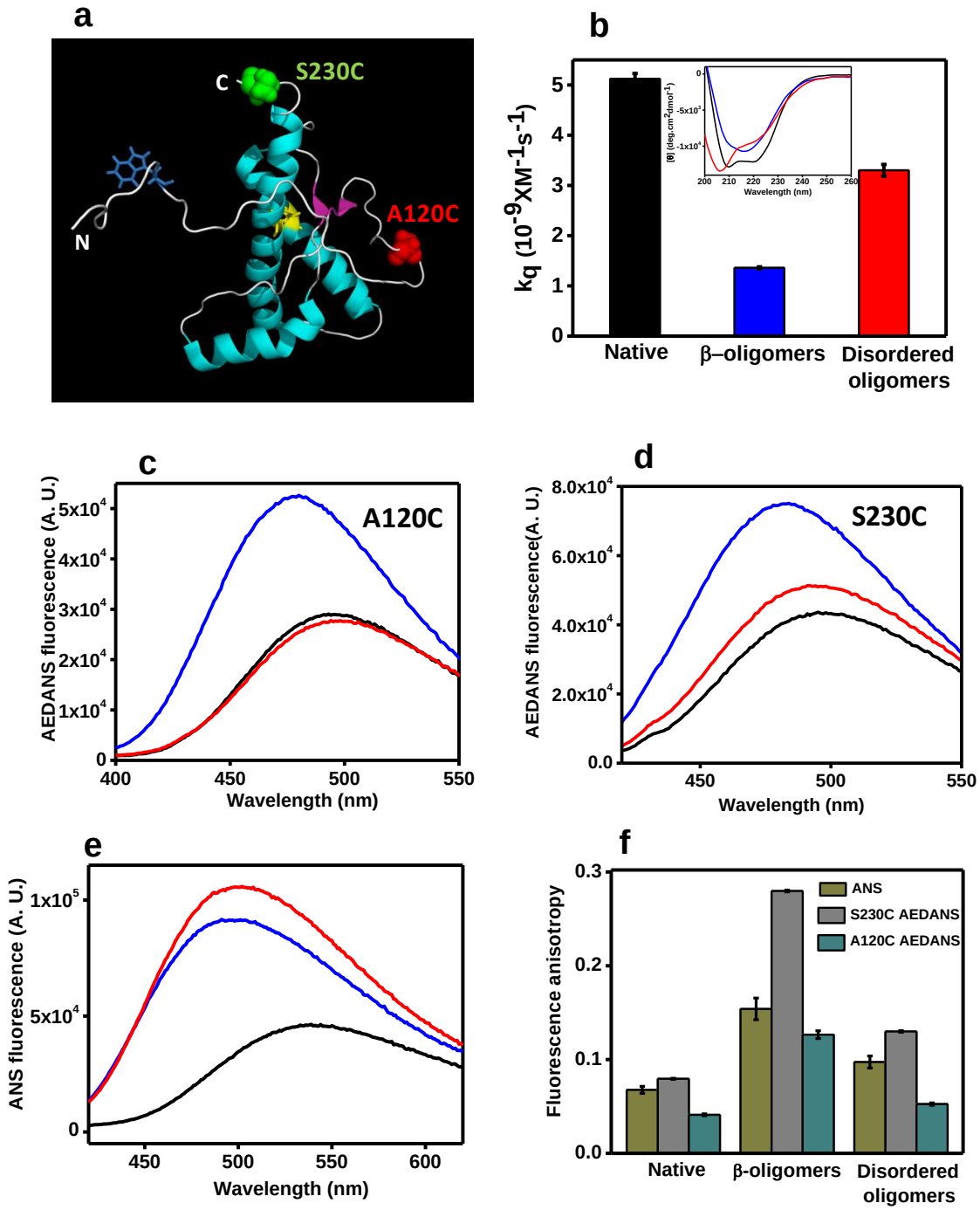

Figure 3.1 a) The NMR structure of human PrP (90-231) (PDB ID: 2LSB) generated using PyMol (DeLano Scientific, LLC, CA). The single Trp is shown in blue and and the disulfide in yellow. The red and green spheres indicate the position of Cys mutations (A120C and S230C). b) Bimolecular quenching rate constant of Trp with acrylamide determined its accessibility under different conditions. The inset shows the far-UV CD spectra. Changes in the fluorescence emission spectra of (c) AEDANS-labeled A120C and (d) AEDANS labeled S230C variants of human prion protein and (e) ANS in the native PrP (black), SDS-induced β-off-pathway oligomers (blue) and SDS NaCl-induced on-pathway oligomers (red). f) Comparison of the changes in the ANS and AEDANS fluorescence anisotropy under studied conditions.

ethyl)amino)naphtalene-1-sulfonic acid (IAEDANS) to probe provincial changes in polarity. IAEDANS has high quantum yield in nonpolar hydrophobic environment and decreased fluorescence intensity in polar solvent (38). For both labeled positions, the native PrP and the disordered oligomers displayed lower AEDANS fluorescence with emission at 495 nm. This is estimated for the probe that is exposed to water environment. On the contrary, β-oligomers, at both labeled sites, AEDANS demonstrated increase in fluorescence intensity with a significant blue shift (~ 16 nm) that is attributed to the placement of AEDANS in more hydrophobic protein interior (Figure 3.1c,d). These observations suggest pronounced structural changes with formation of some local structures in the flexible N- and C-terminal segments in β-oligomers. Whereas, SDS-NaCl-induced on pathway disordered oligomers preserves the indigenous flexibility of these unstructured regions. Further, we investigated changes in hydrophobicity using ANS, an extrinsic molecular probe that has been extensively used to characterize aggregation -prone misfolded intermediates and partially-unfolded states with exposed hydrophobic patches of globular proteins (39). Moreover, alterations in the ANS fluorescence have been found to be associated with cytotoxicity of protein aggregates (40). Free ANS is weakly fluorescent in water but it fluoresces in the hydrophobic environment. ANS binding to the disordered oligomers was distinguished with a substantial increase in the fluorescence quantum yield and a concurrent blue shift (from 540 nm to 498 nm) in the emission wavelength. Similar emission profile was also observed for the β-oligomers. However, the increase in ANS fluorescence was higher for the disordered oligomers indicating the presence of ANS in exposed hydrophobic patches. In contrast, the native protein as expected did not show any evidence of ANS binding (Figure 3.1e). Thus the fine differences observed in the various spectroscopic measurements reveal the divergent conformational changes occurring in the β- and disordered oligomers under the influence of SDS and SDS-NaCl. After following the spectral conformational changes, next we used steady-state fluorescence anisotropy, a readout of rotational mobility of fluorophore and report the changes in size of the biomolecule (38). The fluorescence anisotropy of ANS and AEDANS (at both the positions A120C and S230C) was measured. β-oligomers exhibit the maximum anisotropy for both probes. Whereas, the disordered oligomers demonstrated the slight increase in the anisotropy of ANS and AEDANS compared to the native PrP (Figure 3.1f). Increase in the steady state fluorescence anisotropy evident the overall increase in the size accompanying the conformational changes due to oligomerization. However, it was not possible to discern the conformational dynamics of the misfolded PrP oligomers using

steady-state anisotropy measurements. Therefore we next, carried out time-resolved fluorescence anisotropy measurements.

3.3.2 Probing conformational dynamics, internal motional fluctuations and size change using time-resolved fluorescence

In order to delineate the PrP chain dynamics in the off-pathway SDS-β-oligomers and on-pathway SDS-NaCl-induced disordered oligomers, we used time-resolved fluorescence anisotropy that offers information of both local and global dynamical changes happening in the protein structure (38). Timescales associated with the local (ϕ_{fast}) and the global motion (ϕ_{slow}) of fluorophore provide an excellent method to characterize the conformational flexibility, surroundings and an average size (hydrodynamic radii) of protein/protein

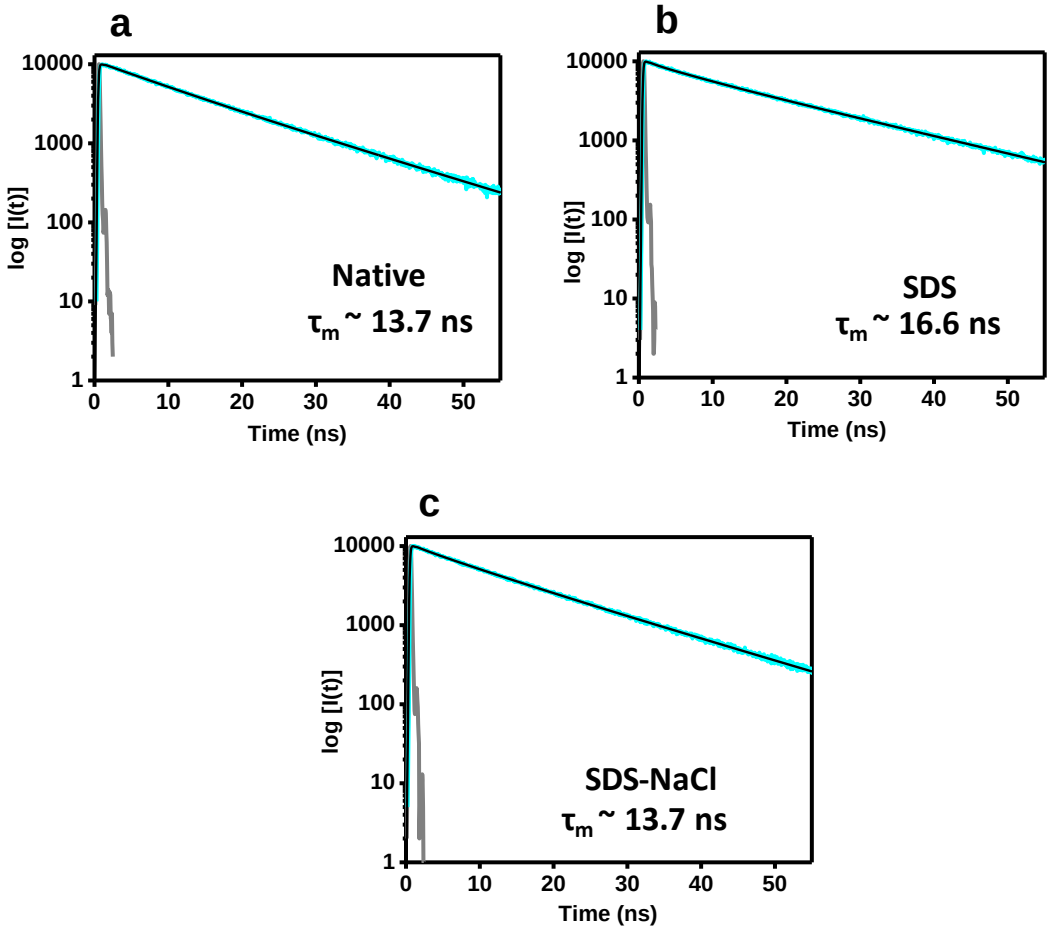

Figure 3.2 Time-resolved fluorescence intensity decay curves of AEDANS-labeled PrP under different forms (a) native state (τ_m ~ 13.7 ns) (b) β-off-pathway oligomers (τ_m ~ 16.6 ns) and (c) on-pathway disordered oligomers (τ_m ~ 13.7 ns). The instrument response function is shown in gray line. The cyan and the black line denote the actual data and the fit, respectively. τ_m stands for the mean fluorescence lifetime of AEDANS.

assemblies, respectively (38). For doing these experiments, we have used the C – terminus Cys mutant (S230C) labeled with IAEDANS. Besides being small and environment sensitive, IAEDANS have a long fluorescence lifetime that is best suited for depolarization measurements to resolve the rotational correlation times and size determination (41). Before embarking on the anisotropy measurements we estimated the changes in the mean fluorescence lifetime under all three states (native, β-oligomers and disordered oligomers) (Figure 3.2). The AEDANS lifetime data was fitted and three lifetimes were recovered (Table 3.1).

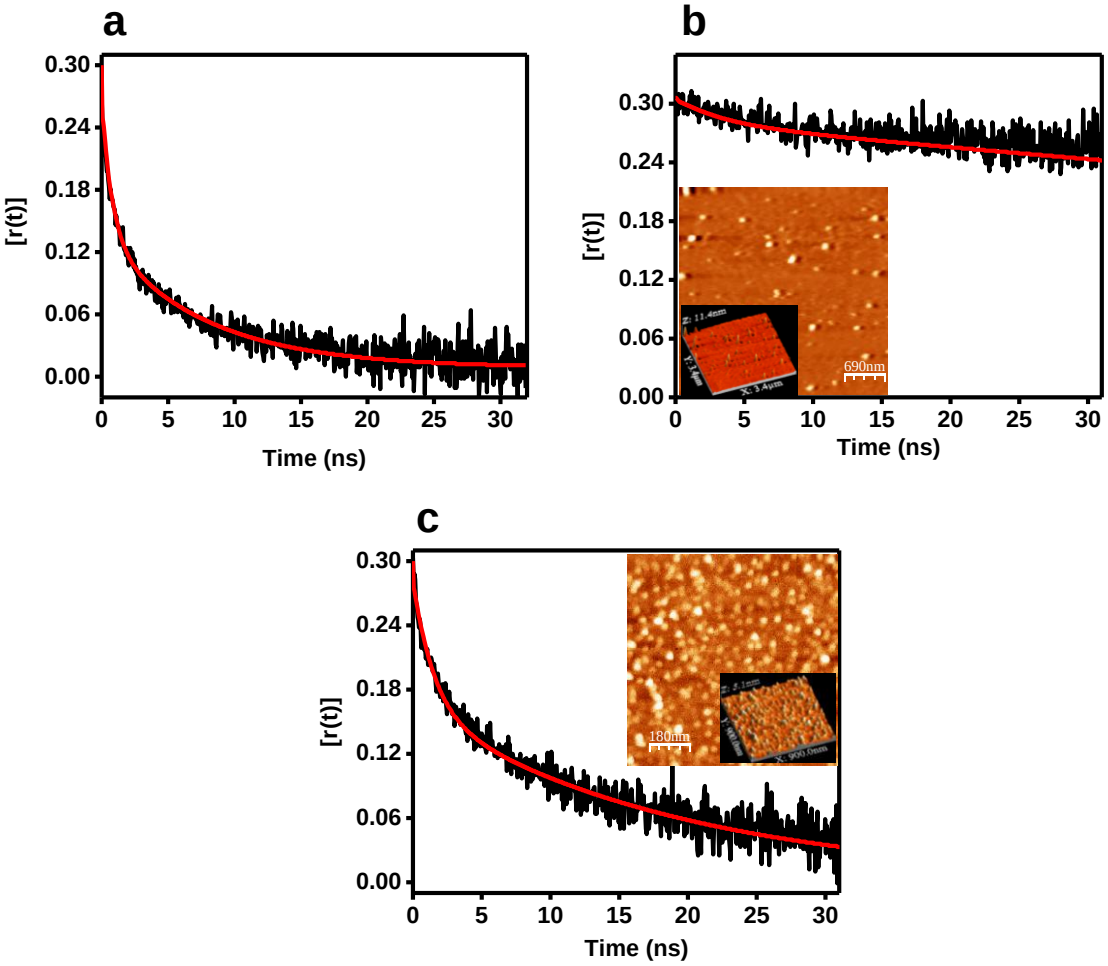

Figure 3.3 Time-resolved fluorescence anisotropy decay curves of AEDANS-labeled PrP under following conditions (a) native state, (b) β-off-pathway oligomers and (c) on-pathway disordered oligomers. The smooth red lines represent the biexponential fit that was used to recover the rotational correlation times listed in Table 1. The insets show the AFM height images along with the 3D projections of off-pathway oligomers (b) and on-pathway oligomers (c).

In the native PrP and disordered oligomers the mean lifetime was found to be constant (~ 13.7 ns). But, it increased to ~ 16.6 ns in the β-oligomers. Moreover, this observation also corroborated the steady state fluorescence intensity spectra. Next, we followed rotational motion of AEDANS using fluorescence anisotropy decay (Figure 3.3). The analysis of decay kinetics yielded fast (ϕ_{fast}) and slow (ϕ_{slow}) rotational correlation times and their respective amplitudes. The comparison of slow rotational correlation times of disordered oligomers (~ 19.2 ns) and native PrP (~ 7.7 ns) suggest an increase in conformational flexibility accompanied with slight increase in molecular expansion indicative of extended conformation in the SDS-NaCl-induced disordered oligomers (Table 3.1) and the mean hydrodynamic diameter was determined to be ~ 5 nm. Whereas, the very long rotational correlation time (ϕ_{slow}) (~ 210 ns) in the β-oligomers indicated dramatic slow tumbling caused by the significant conformational expansion that was clearly evident from the significant increase in the mean hydrodynamic diameter (~ 12 nm) and the molecular volume (Table 3.1). However, owing to the longer correlation time than the fluorescence lifetime of AEDANS in the β-oligomers the time-resolved anisotropy did not decay to zero. Thus, the size estimation from ϕ_{slow} is erroneous. But, it provides a limiting value indicative that the size of β- oligomers is definitely greater than the calculated value. The amplitude associated

Table 3.1 Typical recovered parameters associated with time-resolved fluorescence intensity and anisotropy decays of AEDANS-labeled S230C variant of PrP under different conditions. Estimated hydrodynamic volumes are as follows: ~ 35.44 nm^3 (native); > 970.34 nm^3 (SDS-β-oligomers); ~ 88.72 nm^3 (SDS-NaCl-disordered oligomers)

Protein sample	fluorescence lifetime in ns (amplitude)			mean lifetime (ns)	χ^2	rotational correlation times in ns (amplitude)		r_0	r_{ss}	χ^2
	τ_1 (α_1)	τ_2 (α_2)	τ_3 (α_3)	τ_m		ϕ_1 (β_1)	ϕ_2 (β_2)			
Native	16.2 (0.60)	9.9 (0.39)	1 (0.01)	13.7	1.16	7.7 (0.4)	0.77 (0.6)	0.30	0.06	1.4
β-oligomers	19.8 (0.79)	6.5 (0.16)	0.85 (0.05)	16.6	1.12	> 210 (0.9)	3.3 (0.1)	0.32	0.27	1.5
Disordered oligomers	16.1 (0.71)	8.8 (0.25)	1.61 (0.04)	13.7	1.08	19.2 (0.55)	1.5 (0.45)	0.30	0.11	1.5

with the fast rotational correlation time is the structural parameter that gives information about the flexibility of the fluorophore and the internal structural organization (41). Interestingly, the comparison between the β-oligomers and disordered oligomers revealed large variation in the amplitudes (β_2) of the fast component (Table 3.1). It indicates that due to structural rigidification AEDANS rotational motion is highly restricted in the β-oligomers. On contrary, in the disordered oligomers AEDANS is exposed and has local motional flexibility. This also highlights that C-terminal region gains structure and becomes ordered in the SDS-β-oligomers. However, in the SDS-NaCl-induced disordered oligomers this region remained unstructured and retained conformational flexibility of the native protein. The significantly different structural packing indicated by time-resolved fluorescence depolarization suggests that the local conformational dynamics experienced by AEDANS around it is vastly different in the β-oligomers and disordered oligomers and the overall expansion of molecular volume was several folds higher in the β-oligomers (Table 3.1). Further, we also probed the formation of oligomers using atomic force microscopy (AFM) (Figure 3.3 insets). AFM imaging is widely used to characterize the nanoscale structural/morphological features of protein assemblies (42). As described in the last chapter, the SDS-induced β-oligomers and disordered oligomers have an average height distribution of ~ 9 nm and ~ 4 nm, respectively. It was worth notable that the average size of oligomers as estimated from the height profile corroborated the mean hydrodynamic diameter estimated using the rotational correlation times. Thus, AFM results reinforced the interpretations made from anisotropy decay measurements. Additionally, the findings from time-resolved experiments set the stage for investigating the physicochemical basis of structural transition and oligomerization with respect to hydration dynamics.

3.3.3 Insights into the restrained water dynamics around the on-pathway disordered oligomers

Next, we asked the question: Is there any difference in the nature of water molecules in vicinity of the on-pathway disordered oligomers compared to the native PrP? And, what could be the role of interfacial hydration in the on-pathway oligomers of the PrP? In order to gain insights into the hydration properties we carried out solvent relaxation measurements using time-resolved emission spectra (TRES) (43-48). TRES is very sensitive to changes in micro-polarity and micro-viscosity of the fluorophore microenvironment, therefore,

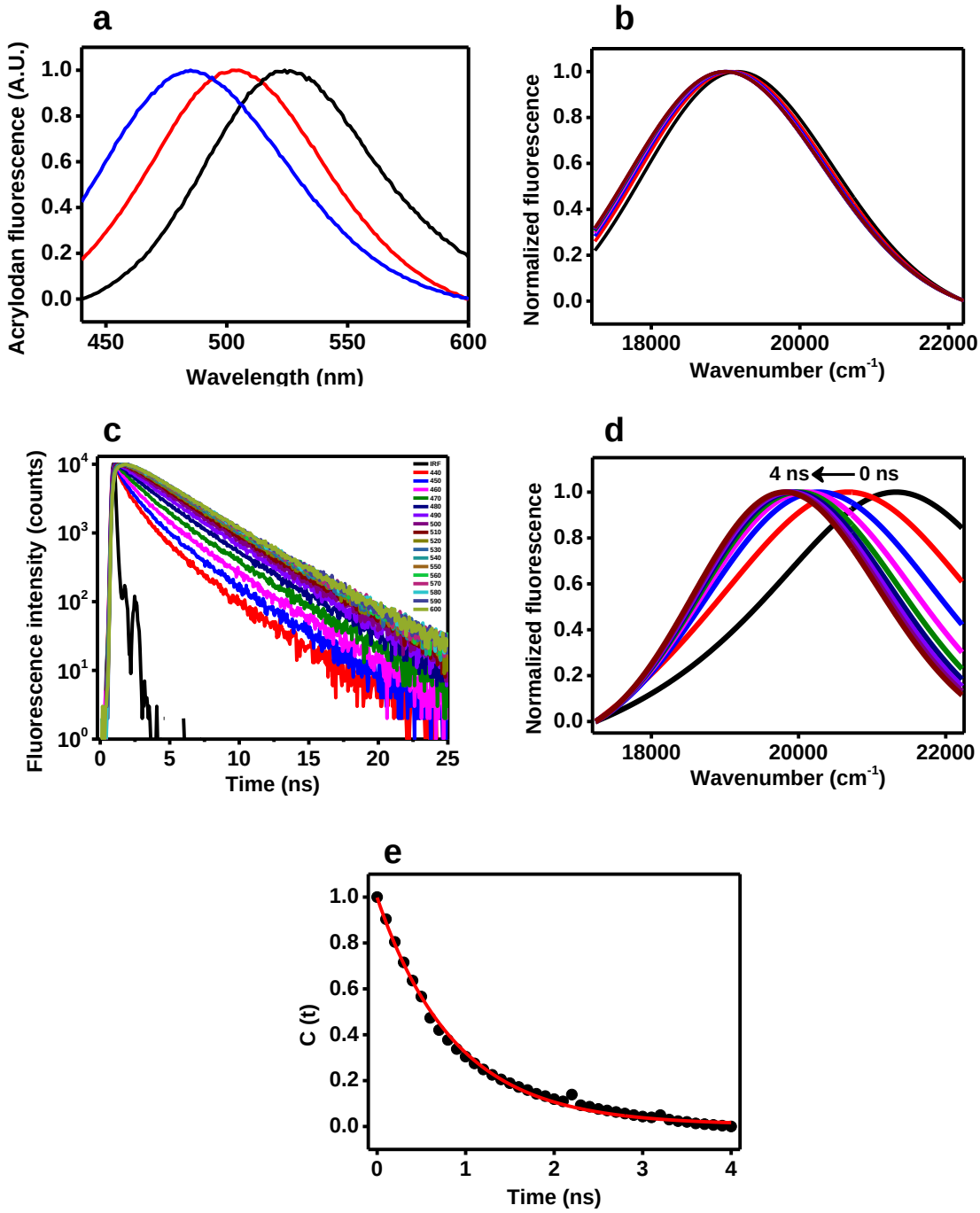

Figure 3.4 a) Normalized steady-state fluorescence spectra of acrylodan-labeled native PrP (black), SDS-induced β-off-pathway oligomers (blue) and SDS NaCl-induced on-pathway oligomers (red). b) Time-resolved emission spectra (TRES) on nanosecond timescale for the acrylodan labeled S230C variant of PrP in the native state. c) The nanosecond time-resolved fluorescence decays of acrylodan-labeled S230C variant of PrP in the disordered on-pathway oligomers showing progressive rise in decays and increase in the lifetime as a function of emission wavelength. d) Time-resolved emission spectra constructed from the time-resolved intensity decays showing gradual Stokes shift with the total frequency shift ($\Delta\nu$) = 1562 ± 73 cm^{-1}. e) Decay kinetics of the solvation correlation function. Filled circles represent the actual values of solvation correlation function and the solid red line denotes the single exponential fit to estimate the solvation time.

serves as a reliable approach to study hydration dynamics at the protein surface. The hydration dynamics around the protein surface is believed to be heterogeneous and very site selective (49). To assess the site-specific role of surface hydration in the PrP misfolding and formation of on-pathway oligomers we have selected an interesting position towards the end of helix 3 (32). Helix 3 is the putative binding site for auxiliary cofactor protein-X and interaction with which is believed to play a crucial role in prion replication (2). To scrutinize the dynamics of water molecules we used the above described Cys mutant of PrP (S230C) covalently labeled with acrylodan. Acrylodan is a small, environment sensitive fluorescent probe that has been widely used for solvation studies in a variety of proteins (45,46,48). Prior to the solvation dynamics measurements, we first monitored the spectral properties of the acrylodan under different states of the PrP viz. native, SDS-β-oligomers and disordered oligomers (Figure 3.4a). In the native PrP, since the C-terminus segment harboring residue 230 is unstructured (Figure 3.1a) the acrylodan exhibit a red-shifted fluorescence peak at ~ 525 nm. The β-oligomers demonstrate a significant blue shift in fluorescence emission (~ 480 nm) indicating that acrylodan is buried and well protected from water. Whereas, in disordered oligomers, the acrylodan display moderate blue shift with the fluorescence maximum at ~ 505 nm suggesting that acrylodan is still exposed in water. These observations also corroborate the IAEDANS spectral fluorescence results obtained for this mutant position (Figure 3.1d). We would like to again highlight that for on-pathway disordered oligomers internal dynamics probed using time-resolved fluorescence anisotropy experiments has already established the significant degree of local motional flexibility and exposure that is comparable to the native PrP. Following these observations, next, we aim to characterize the time scale of solvation process using TRES measurements that monitors and analyze the time dependent response of water molecules recorded in form of time-dependent fluorescence Stokes shift (TDFSS). First, we collected the time-resolved fluorescence decays of acrylodan labeled S230C mutant PrP at a series of emission wavelengths covering the range of its steady state fluorescence spectra i.e. from 440 nm to 600 nm. The on-pathway disordered oligomers displayed a progressive rise in fluorescence decays with an increase in average fluorescence lifetime which is a clear hallmark of slow (ns) solvent relaxation (Figure 3.4c). The information from fluorescence decay analysis was used to construct TRES (Figure 3.4d). The time-resolved spectra of the disordered oligomers depicts the total dynamic solvent shift of 1562 ± 73 cm^{-1} in 4 ns due to the relaxation process around acrylodan caused by the reorientation of the water molecules. On the contrary, it is important to notice that the native

PrP did not display signature of solvation (Figure 3.4b). Next, we estimated the time scale of water reorientation by monitoring the decay of hydration correlation function *C(t)*. By fitting the *C(t)* trace, our experiments captured a monophasic slow hydration dynamics of 0.80 ± 0.06 ns that is nearly three orders of magnitude slower than bulk water relaxation (~1 ps) (Figure 3.4e). It is possible that we might have missed the ultrafast solvation component due to bulk water relaxation. This impeded timescale of water reorientation matches with the long relaxation times suggested by solvation dynamics studies for the constrained water in several chemical and biochemical molecular systems (37,43). Since, MD calculations point out that C-terminus of helix 3 has significant proportion of underwrapped back bone hydrogen bonds that are very susceptible to water attack and reorganization (33,34). Therefore, such a site specific retarded solvation rate could be ascribed to the engagement of water molecules in hydrogen bonding with the protein surface that in turn stabilizes the on-pathway disordered oligomers and thus, favors the conformational rearrangement from native to disordered oligomers.

3.4 CONCLUSION

A line of evidences have firmly established that conversion of native PrP (PrP) into protease resistant scrapie isoform (PrPres) involves the obligatory partial unfolding of monomeric native structure and oligomerization (PrP*) (20). Oligomers constitute the key intermediates that entail the hierarchical assembly of amyloid fibrils. Given that the fluctuations in the motion of water molecules in the hydration shell influence the protein stability and structure (31). Thus, physical characterization of hydration dynamics is important to investigate its role in the PrP conformational and topological reformation. Our results provide a comprehensive description of the structural and conformational differences between the disordered on-pathway oligomers and the structured off-pathway oligomers. The loss of secondary structure, exposure of hydrophobic sites and increase in hydrodynamic volume indicates a molten globule like nature of the SDS-NaCl-induced on-pathway disordered oligomers. The large amplitude (β_2) of fast motion (ϕ_2) recovered from the time-resolved fluorescence depolarization measurements highlighted the conformational flexibility of C-terminus in the disordered oligomers, similar to the native PrP, whereas in the SDS-induced off-pathway β-oligomers this region is buried. This observation is significant in context of previous report that indentified an exposed epitope region at the C-terminal end region (225 to 231) in both PrP^{C} and PrP^{Sc} (16). By surface probing the C-terminus end of PrP we have for the first time

experimentally addressed the site specific structural and dynamical role of water molecules in the on-pathway disordered oligomers. In our experiments, we observed approximately a nanosecond relaxation of interfacial water that means its motion is impeded by ~ 3 orders of magnitude compared to the bulk water that relaxes in the time range between 100s of femtoseconds to a picosecond (29). Nevertheless, different experimental techniques e.g. nuclear magnetic resonance, dielectric relaxation, quasi elastic neutron scattering and solvation dynamics using TDFSS of fluorescent probe have surmised varying relaxation times for hydration layer dynamics on the protein surface. This anomaly might arise because these experimental approaches differ in their principle and thus probe different physical attributes of the water molecules (37). In our experiments we probed the solvation dynamics around the end unstructured region by covalent-labeling the C-terminal end of the protein thus, it negates the effects of protein residues motion on TDFSS. We have chosen the helix 3 C-terminus end position for probing the solvation dynamics for the following reasons. It is the binding site for protein-X (1) and is believed to be exposed in the PrP^{C} and scrapie isoforms (50). Also, we confirmed the flexibility of the C-terminus end in the disordered

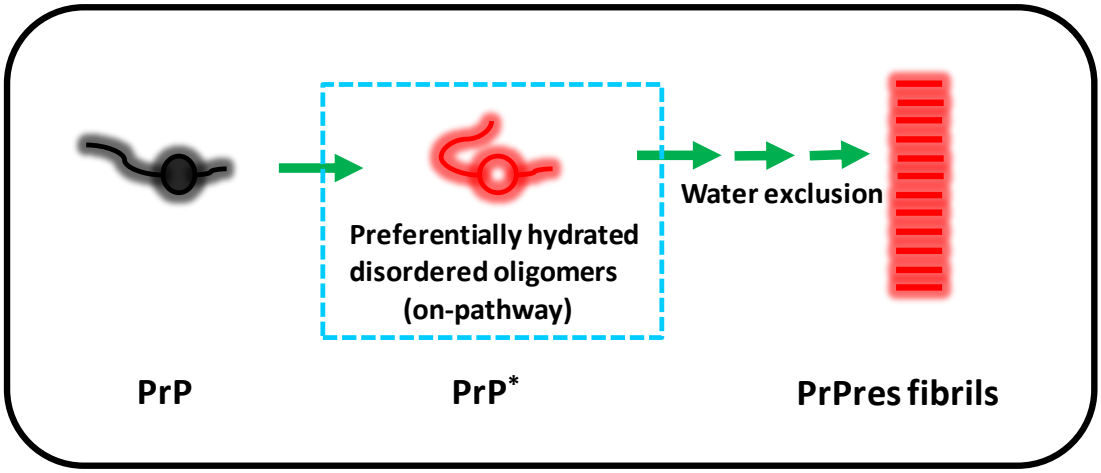

Figure 3.6 The proposed schematic model for the role of ordered water molecules in PrP oligomerization and amyloid fibrils.

oligomers by the anisotropy decay experiments. Additionally, there are significant numbers of underwrapped weak backbone hydrogen bonds saturated in the helix 3 C-terminus (32). These backbone hydrogen bonds are prone to water attack and thus might be involved in the PrP conformational switching to the partial unfolded disordered oligomers.

Our results infer a correspondence between the under-protected back bone hydrogen bonds and the possible restructuring of the biological water hydrogen bond network during PrP misfolding and in the on-pathway oligomers. The slowed water dynamics reveal intercoupling of protein motion with the water molecules probably by hydrogen bonding that energetically favor the formation of disordered oligomers. We anticipate that this interfacial hydration layer could act as scaffolding element that exquisitely mediate the intermolecular interactions between oligomers and entropically favor the formation of amyloid fibrils by exclusion of ordered water molecules (Figure 3.6). On the contrary, in the off-pathway β-oligomers C-terminus end segment is buried and could not interact with water molecules. Taken together, our results shed light into the previously unexplored aspect of structured water molecules in the PrP oligomers and indicate that the on-pathway disordered oligomers are stabilized by preferential hydration. Moreover, the study also present a new dimension of research to comprehend the physicochemical force behind the phenomenon of conformational transition and oligomerization in proteins implicated in variety of neurodegenerative disorders like Alzheimer's disease and Parkinson's disease.

3.5 REFERENCES

1. Prusiner, S. B. (2004) *Prion biology and diseases*, Cold Spring Harbor Laboratory Press
2. Prusiner, S. B. (1998) Prions. *Proc Natl Acad Sci U S A* **95**, 13363-13383
3. Prusiner, S. B. (1982) Novel proteinaceous infectious particles cause scrapie. *Science (New York, N.Y.)* **216**, 136-144
4. Collinge, J. (2001) Prion diseases of humans and animals: their causes and molecular basis. *Annual review of neuroscience* **24**, 519-550
5. Prusiner, S. B. (1997) Prion Diseases and the BSE Crisis. *Science* **278**, 245-251
6. Ma, J., and Wang, F. (2014) Prion disease and the 'protein-only hypothesis'. *Essays Biochem* **56**, 181-191
7. Horiuchi, M., and Caughey, B. (1999) Prion protein interconversions and the transmissible spongiform encephalopathies. *Structure (London, England : 1993)* **7**, R231-240
8. Stahl, N. (1987) Scrapie prion protein contains a phosphatidylinositol glycolipid. *Cell* **51**, 229-240

9. Kretzschmar, H. A., Prusiner, S. B., Stowring, L. E., and DeArmond, S. J. (1986) Scrapie prion proteins are synthesized in neurons. *Am J Pathol* **122**, 1-5
10. Zahn, R., Liu, A., Lührs, T., Riek, R., von Schroetter, C., López García, F., Billeter, M., Calzolai, L., Wider, G., and Wüthrich, K. (2000) NMR solution structure of the human prion protein. *Proceedings of the National Academy of Sciences of the United States of America* **97**, 145-150
11. Biljan, I., Giachin, G., Ilc, G., Zhukov, I., Plavec, J., and Legname, G. (2012) Structural basis for the protective effect of the human prion protein carrying the dominant-negative E219K polymorphism. *The Biochemical journal* **446**, 243-251
12. Pan, K. M., Baldwin, M., Nguyen, J., Gasset, M., Serban, A., Groth, D., Mehlhorn, I., Huang, Z., Fletterick, R. J., and Cohen, F. E. (1993) Conversion of alpha-helices into beta-sheets features in the formation of the scrapie prion proteins. *Proceedings of the National Academy of Sciences of the United States of America* **90**, 10962-10966
13. Dearmond, S. J., McKinley, M. P., Barry, R. A., Braunfeld, M. B., McColloch, J. R., and Prusinert, S. B. (1985) Identification of prion amyloid filaments in scrapie-infected brain. *Cell* **41**, 221-235
14. Kelly, J. W. (1998) The environmental dependency of protein folding best explains prion and amyloid diseases. *Proceedings of the National Academy of Sciences* **95**, 930-932
15. Kirby, L. (2003) In vitro cell-free conversion of bacterial recombinant PrP to PrPres as a model for conversion. *Journal of General Virology* **84**, 1013-1020
16. Baskakov, I. V., Legname, G., Baldwin, M. a., Prusiner, S. B., and Cohen, F. E. (2002) Pathway complexity of prion protein assembly into amyloid. *The Journal of biological chemistry* **277**, 21140-21148
17. Cordeiro, Y., Kraineva, J., Ravindra, R., Lima, L. M., Gomes, M. P., Foguel, D., Winter, R., and Silva, J. L. (2004) Hydration and packing effects on prion folding and beta-sheet conversion. High pressure spectroscopy and pressure perturbation calorimetry studies. *J Biol Chem* **279**, 32354-32359
18. Singh, J., and Udgaonkar, J. B. (2015) Molecular Mechanism of the Misfolding and Oligomerization of the Prion Protein: Current Understanding and Its Implications. *Biochemistry* **54**, 4431-4442
19. Breydo, L., and Uversky, V. N. (2015) Structural, morphological, and functional diversity of amyloid oligomers. *FEBS Lett* **589**, 2640-2648

20. DeMarco, M. L., and Daggett, V. (2004) From conversion to aggregation: protofibril formation of the prion protein. *Proc Natl Acad Sci U S A* **101**, 2293-2298
21. Morillas, M., Swietnicki, W., Gambetti, P., and Surewicz, W. K. (1999) Membrane Environment Alters the Conformational Structure of the Recombinant Human Prion Protein. *Journal of Biological Chemistry* **274**, 36859-36865
22. Wang, F., Yang, F., Hu, Y., Wang, X., Wang, X., Jin, C., and Ma, J. (2007) Lipid interaction converts prion protein to a PrPSc-like proteinase K-resistant conformation under physiological conditions. *Biochemistry* **46**, 7045-7053
23. Wang, F., Wang, X., Yuan, C.-G., and Ma, J. (2010) Generating a prion with bacterially expressed recombinant prion protein. *Science (New York, N.Y.)* **327**, 1132-1135
24. Caughey, B., Baron, G. S., Chesebro, B., and Jeffrey, M. (2009) Getting a grip on prions: oligomers, amyloids, and pathological membrane interactions. *Annual review of biochemistry* **78**, 177-204
25. Supattapone, S. (2014) Elucidating the role of cofactors in mammalian prion propagation. *Prion* **8**, 100-105
26. Xiong, L.-w., Raymond, L. D., Hayes, S. F., Raymond, G. J., and Caughey, B. (2001) Conformational change , aggregation and fibril formation induced by detergent treatments of cellular prion protein. *Journal of Neurochemistry* **79,** 669-678
27. Leffers, K.-W., Wille, H., Stöhr, J., Junger, E., Prusiner, S. B., and Riesner, D. (2005) Assembly of natural and recombinant prion protein into fibrils. *Biological chemistry* **386**, 569-580
28. Stöhr, J., Weinmann, N., Wille, H., Kaimann, T., Nagel-Steger, L., Birkmann, E., Panza, G., Prusiner, S. B., Eigen, M., and Riesner, D. (2008) Mechanisms of prion protein assembly into amyloid. *Proceedings of the National Academy of Sciences of the United States of America* **105**, 2409-2414
29. Pal, S. K., Peon, J., and Zewail, A. H. (2002) Biological water at the protein surface: dynamical solvation probed directly with femtosecond resolution. *Proc Natl Acad Sci U S A* **99**, 1763-1768
30. Nandi, N., and Bagchi, B. (1997) Dielectric relaxation of biological water. *The Journal of Physical Chemistry B* **101**, 10954-10961

31. Frauenfelder, H., Chen, G., Berendzen, J., Fenimore, P. W., Jansson, H., McMahon, B. H., Stroe, I. R., Swenson, J., and Young, R. D. (2009) A unified model of protein dynamics. *Proc Natl Acad Sci U S A* **106**, 5129-5134
32. Fernandez, A. (2002) Insufficient hydrogen-bond desolvation and prion-related disease. *Eur J Biochem* **269**, 4165-4168
33. Fernandez, A., and Scheraga, H. A. (2003) Insufficiently dehydrated hydrogen bonds as determinants of protein interactions. *Proc Natl Acad Sci U S A* **100**, 113-118
34. De Simone, A., Dodson, G. G., Verma, C. S., Zagari, A., and Fraternali, F. (2005) Prion and water: tight and dynamical hydration sites have a key role in structural stability. *Proc Natl Acad Sci U S A* **102**, 7535-7540
35. Choi, Y. P., Groner, A., Ironside, J. W., and Head, M. W. (2011) Correlation of polydispersed prion protein and characteristic pathology in the thalamus in variant Creutzfeldt-Jakob disease: implication of small oligomeric species. *Brain Pathol* **21**, 298-307
36. Pal, S. K., and Zewail, A. H. (2004) Dynamics of water in biological recognition. *Chem Rev* **104**, 2099-2123
37. Bagchi, B. (2005) Water dynamics in the hydration layer around proteins and micelles. *Chem Rev* **105**, 3197-3219
38. Lakowicz, J. R. (1999) Introduction to fluorescence. in *Principles of fluorescence spectroscopy*, Springer. pp 1-23
39. Semisotnov, G. V., Rodionova, N. A., Razgulyaev, O. I., Uversky, V. N., Gripas', A. F., and Gilmanshin, R. I. (1991) Study of the "molten globule" intermediate state in protein folding by a hydrophobic fluorescent probe. *Biopolymers* **31**, 119-128
40. Bolognesi, B., Kumita, J. R., Barros, T. P., Esbjorner, E. K., Luheshi, L. M., Crowther, D. C., Wilson, M. R., Dobson, C. M., Favrin, G., and Yerbury, J. J. (2010) ANS binding reveals common features of cytotoxic amyloid species. *ACS Chem Biol* **5**, 735-740
41. Mukhopadhyay, S., Nayak, P. K., Udgaonkar, J. B., and Krishnamoorthy, G. (2006) Characterization of the formation of amyloid protofibrils from barstar by mapping residue-specific fluorescence dynamics. *J Mol Biol* **358**, 935-942
42. Adamcik, J., and Mezzenga, R. (2012) Study of amyloid fibrils via atomic force microscopy. *Current Opinion in Colloid & Interface Science* **17**, 369-376

43. Bhattacharyya, K., and Bagchi, B. (2000) Slow dynamics of constrained water in complex geometries. *The Journal of Physical Chemistry A* **104**, 10603-10613
44. Samaddar, S., Mandal, A. K., Mondal, S. K., Sahu, K., Bhattacharyya, K., and Roy, S. (2006) Solvation dynamics of a protein in the pre molten globule state. *J Phys Chem B* **110**, 21210-21215
45. Jha, A., Ishii, K., Udgaonkar, J. B., Tahara, T., and Krishnamoorthy, G. (2010) Exploration of the correlation between solvation dynamics and internal dynamics of a protein. *Biochemistry* **50**, 397-408
46. Batabyal, S., Mondol, T., and Pal, S. K. (2013) Picosecond-resolved solvent reorganization and energy transfer in biological and model cavities. *Biochimie* **95**, 1127-1135
47. Balasubramanian, S., and Bagchi, B. (2001) Slow solvation dynamics near an aqueous micellar surface. *The Journal of Physical Chemistry B* **105**, 12529-12533
48. Arya, S., and Mukhopadhyay, S. (2014) Ordered water within the collapsed globules of an amyloidogenic intrinsically disordered protein. *J Phys Chem B* **118**, 9191-9198
49. Zhong, D., Pal, S. K., and Zewail, A. H. (2011) Biological water: A critique. *Chemical Physics Letters* **503**, 1-11
50. Peretz, D., Williamson, R. A., Matsunaga, Y., Serban, H., Pinilla, C., Bastidas, R. B., Rozenshteyn, R., James, T. L., Houghten, R. A., Cohen, F. E., Prusiner, S. B., and Burton, D. R. (1997) A conformational transition at the N terminus of the prion protein features in formation of the scrapie isoform. *Journal of molecular biology* **273**, 614-622

Chapter 4

Trafficking of Cellular Prion Protein and its Disease Related Mutants

4.1 INTRODUCTION

The cellular prion protein (PrP^C) is a glycoprotein tethered to the cell surface by its C-terminal glycosyl-phosphatidylinositol (GPI) anchor (1). It is constitutively expressed by variety of cells but particularly abundant expression is found in neuronal and glial cells (2). The physiological function of PrP^C is largely uncertain, but owing to its surface localization in lipid rafts various studies have implicated its role in transmembrane signaling, cell adhesion, protection from oxidative stress, ligand uptake, immunomodulation, copper/zinc metabolism, synaptic transmission and apoptosis (3). Under normal physiological conditions, PrP^C is α-helical, detergent soluble and protease sensitive (4). The conformational transition of PrP^C to β-rich, protease resistant, detergent insoluble state leads to the generation of an unconventional proteinaceous infectious agent known as scrapie PrP (PrP^{Sc}) (5). PrP^{Sc} is known to be the major causative agent responsible for transmissible spongiform encephalopathies (TSE) in humans and other mammals (6). Prion diseases (TSE) have unique etiology being infectious, genetic or sporadic in origin. The details of $PrP^C \rightarrow PrP^{Sc}$ transconversion event are still elusive. But, PrP^C act as an absolute substrate required for PrP^{Sc} replication and disease progression (7).

A body of experiments has revealed that elimination of surface PrP^C by phosphatidylinositol-specific phospholipase C (PIPLC) or by inhibiting trafficking to cell surface prevented the generation of PrP^{Sc} and therefore, indicate the involvement of PrP^C subcellular trafficking in interaction with scrapie isoform (8,9). Moreover, several mutations in the PrP^C related to hereditary prion diseases are known to cause aberrant PrP^C metabolism (10-12). However, endocytosis and subcellular trafficking of PrP^C is poorly understood (8,13). The precise knowledge of its intracellular trafficking and endocytic pathways might also help in explaining how a single protein performs plethora of functions. Diverse results from different research groups have proposed multiple internalization pathways for PrP^C (13,14). The immunoelectron microscopy studies on primary sensory neurons and other experiments on different neural cell lines have shown that PrP^C leaves the raft, endocytosed by clathrin-coated pits and constitutively recycles between the cell membrane and endocytic compartments (15,16). The blockade of PrP^C internalization in the cells treated with hypertonic medium and in presence of dynamin I mutant (K44A) provide evidence in favor of clathrin-mediated endocytosis (17,18). Although, PrP^C is devoid of the cytoplasmic tail to interact with adapter proteins and endocytosis is speculated to involve an unknown PrP^C receptor transmembrane protein that binds to the N-terminal segment of PrP^C (16,19-21). In

another finding the transmembrane LPR1 has been identified as a co-receptor that mediates the endocytosis of PrP^C (14). However, given the GPI-anchor, an archetypal raft-localization signal, PrP^C has been found enriched in lipid rafts, detergent resistant heterologous membrane structures, and was localized to caveolae or caveolae-like domains in murine neuronal N2a and Chinese Hamster Ovary cells (22-25). In these experiments, endocytosis was found to be sensitive for cholesterol depletion (26). Therefore, these results speculate caveolae-mediated mechanism of PrP endocytosis. But, there are other reports that question the existence of caveolae in the most mature neuronal cells (16,27,28). Moreover, depending upon the endocytic pathway the organelles involved in PrP^C trafficking would also vary.

The endocytosis of GPI-anchored proteins is a perplexing cellular affair. Unlike other raft proteins e.g. Thy-1, the GPI anchor is not solely required for targeting of PrP^C to raft. The N-terminus unstructured domain has been demonstrated to confer the association with lipid rafts (14,21,29,30). Analysis of endocytosis of different GPI-anchored protein revealed diverse internalization mechanisms. The minimum GPI-anchored protein [GPI-GFP (green fluorescent protein)] recycles between plasma membrane and Golgi complex via clathrin-independent manner and folate receptor is trafficked to plasma membrane through recycling endosomes (31,32). On the contrary, the GPI-anchored proteins in trypanosome and anthrax toxin receptor has been shown to partition in rafts and internalized in a clathrin-dependent fashion (33,34). Thus, there might be several mechanisms responsible for endocytosis of GPI-anchored proteins.

To delineate the transconversion mechanism and to understand, the function of PrP^C it is important to unravel the exact mechanism of PrP^C endocytosis and to define the cellular organelles involved in this process. We are interested in examining the endocytic mechanisms for PrP^C and the role of exosomes in the exocytosis of disease related pathogenic mutants of PrP. We have embarked on these studies, starting with the preliminary investigations targeting the intracellular localization of wild-type (wt) PrP^C and its mutants involved in familial prion disorders.

4.2 EXPERIMENTAL SECTION

4.2.1 Plasmids

The EGFP-mouse PrP^C expression construct in pcDNA3.1/Hygro(+) (Invitrogen) was a kind gift from Prof. Roberto Chiesa. (Department of Neuroscience, IRCCS-Mario Negri Institute for Pharmacological Research, Milan, Italy). The D177N and E199K mutants of EGFP-mouse PrP were generated using QuickChange site-directed mutagenesis kit (Agilent). Arl8b with C-terminal HA tag expression vector was a kind gift from Dr. Mahak Sharma (IISER, Mohali).

4.2.2 Cell culture

The HeLa and HEK-293T cells were cultured and maintained in 75-cm^2 culture flasks in Dulbecco's modified Eagle's medium (Life Technologies) supplemented with 10% fetal bovine serum (FBS), non-essential amino acids and penicillin/streptomycin (Life Technologies), in an atmosphere of 5% CO_2 at 37 °C. For transient transfections, cells grown on glass coverslips and transfection was performed by liposome-mediated method using LipofectAMINE 2000 (Invitrogen) for 12 h.

4.2.3 Antibodies

The following antibodies were used in this study: anti-giantin, anti-LAMP1, anti-EEA1 (BD Biosciences), anti-M6PR, anti-CD63 and anti-HA (Covance). Alexa fluoro-conjugated secondary goat anti-rabbit and goat anti-mouse antibodies were purchased from Life technologies.

4.2.4 Immunofluorescence

To visualize surface staining, transiently transfected cells grown on glass coverslips were washed with phosphate-buffered saline (PBS) and fixed with 4% paraformaldehyde. For intracellular staining, after fixation, blocking was carried out with 5% FBS and 0.2% saponin in PHEM buffer for 30 min. Following, cells were washed thrice with PBS and reacted with primary antibodies diluted in blocking solution for 45 min. Subsequently, cells were washed thrice with PBS and processed for indirect immunofluorescence using specific antibodies. Coverslips were mounted on glass slides and staining was visualized with a Zeiss 710

Confocal Laser Scanning Microscope using a Plan-Apochromat 63×/1.4 NA oil objective with appropriate filters. The Zeiss Zen software was used for data acquisition.

4.3 RESULTS AND DISCUSSION

For our experiments, we have used EGFP-tagged mouse PrP^{C} that has been previously shown to behave normally as PrP^{C} and is correctly targeted to the cell surface (12,35,36). We have compared the intracellular localization of wt PrP^{C} with two different diseased mutations responsible for genetic prion pathologies. The familial prion diseases are caused by the germline mutations in the *Prnp* gene encoding PrP^{C}. Several hotspots have been identified in the *Prnp* gene; mutations in these regions e.g. P101L, D177N, E199K, Y145stop and Q217R induce the conformational conversion to the scrapie isoform (37). Localization studies are important to in order to characterize the intra-cellular organelles that harbor PrP during its transit to plasma membrane. In our study, we have used two different mutants, D177N and E199K, associated with familial prion disorders, fatal familial insomnia and Creutzfeldt-Jakob disease, respectively. These mutations are known to destabilize the native PrP^{C} conformation (37). To get preliminary insights in the steady-state distribution of wt PrP^{C} and mutants we visualized their localization in the cultured HeLa cells and HEK 293T cells using fluorescence microscopy after paraformaldehyde fixation. The cells transfected with wt-PrP exhibited a bright staining over the entire cell surface. Whereas, PrP^{E199K} demonstrated decreased membrane staining and for PrP^{D177N} insignificant cell-surface staining was observed. In addition, both mutants revealed a quite different internal distribution pattern and appeared to be clustered in form of foci (Figure 4.1).

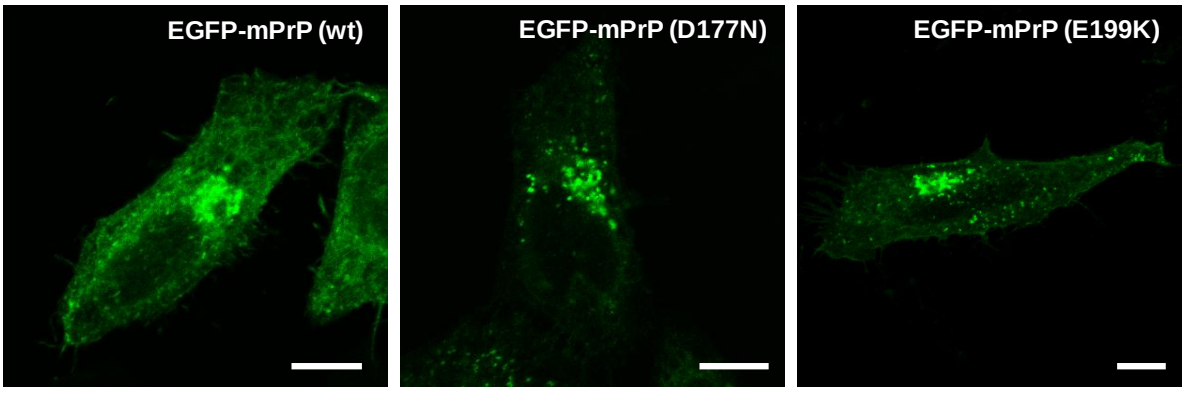

Figure 4.1 Effect of E199K and D177N mutations on PrP localization and surface staining. HeLa cells were transiently transfected with GFP-PrP-wild-type/-D177N/-E199K constructs. Confocal scanning fluorescence imaging of paraformaldehyde-fixed HeLa cells expressing different GFP-PrP isoforms. Scale bar = 10 µm.

Next, we analyzed that both wt and mutant prion proteins colocalized with giantin, the Golgi complex marker (Figure 4.2, 4.3). These results suggest that mutant isoforms of PrP^{C} exhibit an impaired transportation to the cell surface and accumulate in form of unusual punctate structures in the cytoplasm. Moreover, the same results were obtained in both the cell types, HeLa and HEK 293T, therefore we opted HeLa cells for other experiments (Figure 4.2).

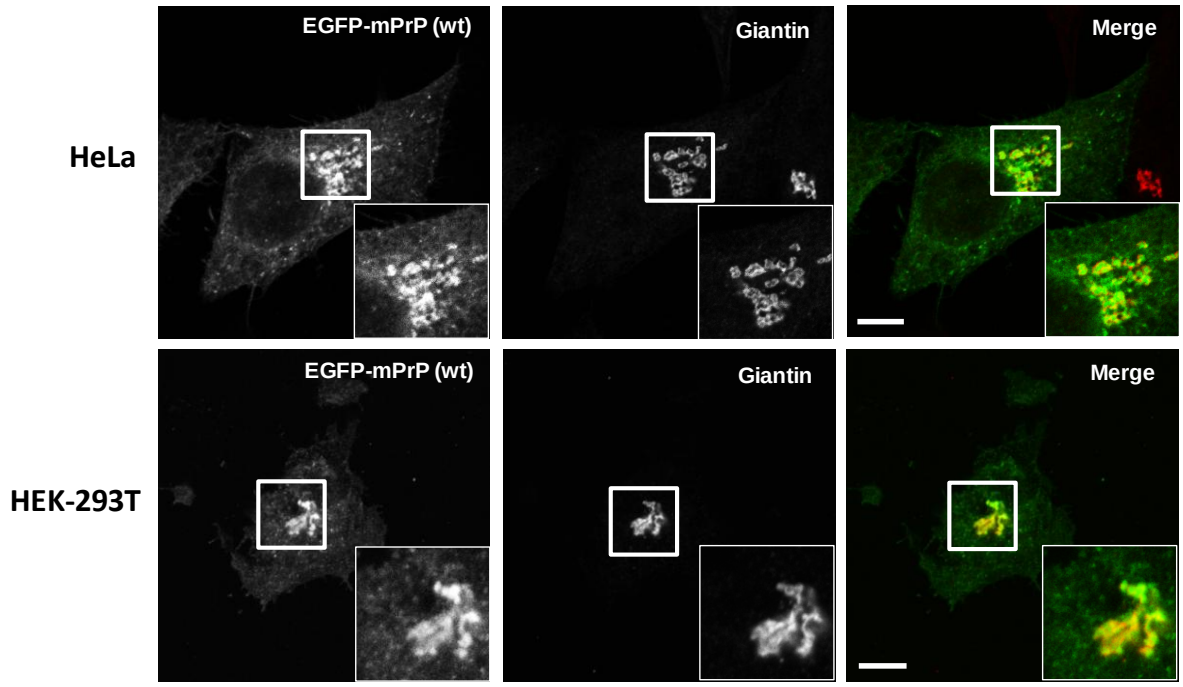

Figure 4.2 Immunofluorescence microscopy depicting the colocalization of EGFP-PrP-wild-type with Golgi body marker giantin in the fixed HeLa cells and HEK-293T cells. Co-localized pixels are shown in the inset. Scale bar = 10 µm.

Further, we investigated the sub-cellular identification of the punctate structures accumulated in the cytoplasm of the cells transfected with PrP^{D177N} and PrP^{E199K}. We checked for the colocalization of these foci with different well-defined organelles that act as trafficking vehicles using antibodies specific for different organelle markers (Figure 4.4, 4.5). For example, we looked at the endo-lysosomal pathway using lysosomal-associated membrane protein 1 (LAMP-1) marker for lysosome, early endosome-associated protein 1 (EEA1) that is associated with Rab5 and early endosomes, and mannose-6-phosphate receptor (M6PR) is engaged in the transport of lysosomal enzymes from the Golgi and cell surface to the lysosomes and is also identified in exosomes in certain cells.

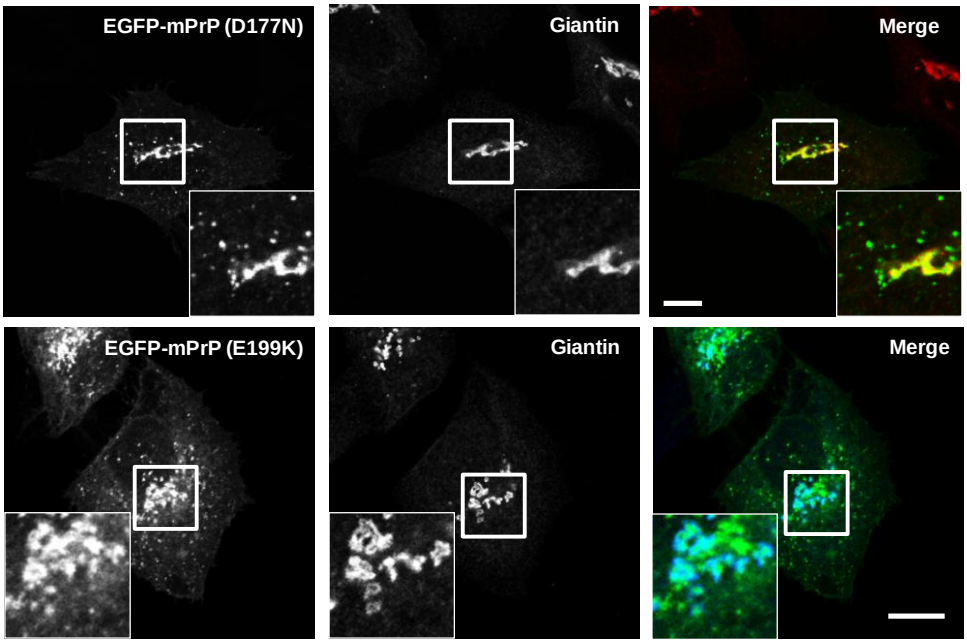

Figure 4.3 Immunofluorescence microscopy depicted the colocalization of EGFP-mutant PrP isoforms (PrP^{D177N} or PrP^{E199K}) with Golgi body marker giantin in the fixed HeLa cells. Co-localized pixels are shown in the inset. Scale bar = 10 µm.

Strikingly, we did not find colocalization with any of the endo-lysosomal pathway compartments. We also analyzed that PrP^{D177N} did not localize with small GTP-binding protein Arl8, a member of Arl (Arf-like) family of small GTPases that is involved in regulating lysosomal trafficking (38). Further, we investigated if there is any association of mutant prion proteins with exosomes. Exosomes are exocytic intraluminal vesicles that are suspected to entail dissemination of prions and abnormal PrP. We did not find colocalization with exosomal markers like CD63.

4.4 CONCLUSION

Our preliminary findings are in contrast to the previous studies that report colocalization of the mutant PrP isoforms with endosomal or lysosomal compartments (31). The discordant results might arise either due to use of different cell types or it point to non-clathrin/ caveolae driven internalization mechanisms, which reroutes the PrP from endosomal/lysosomal

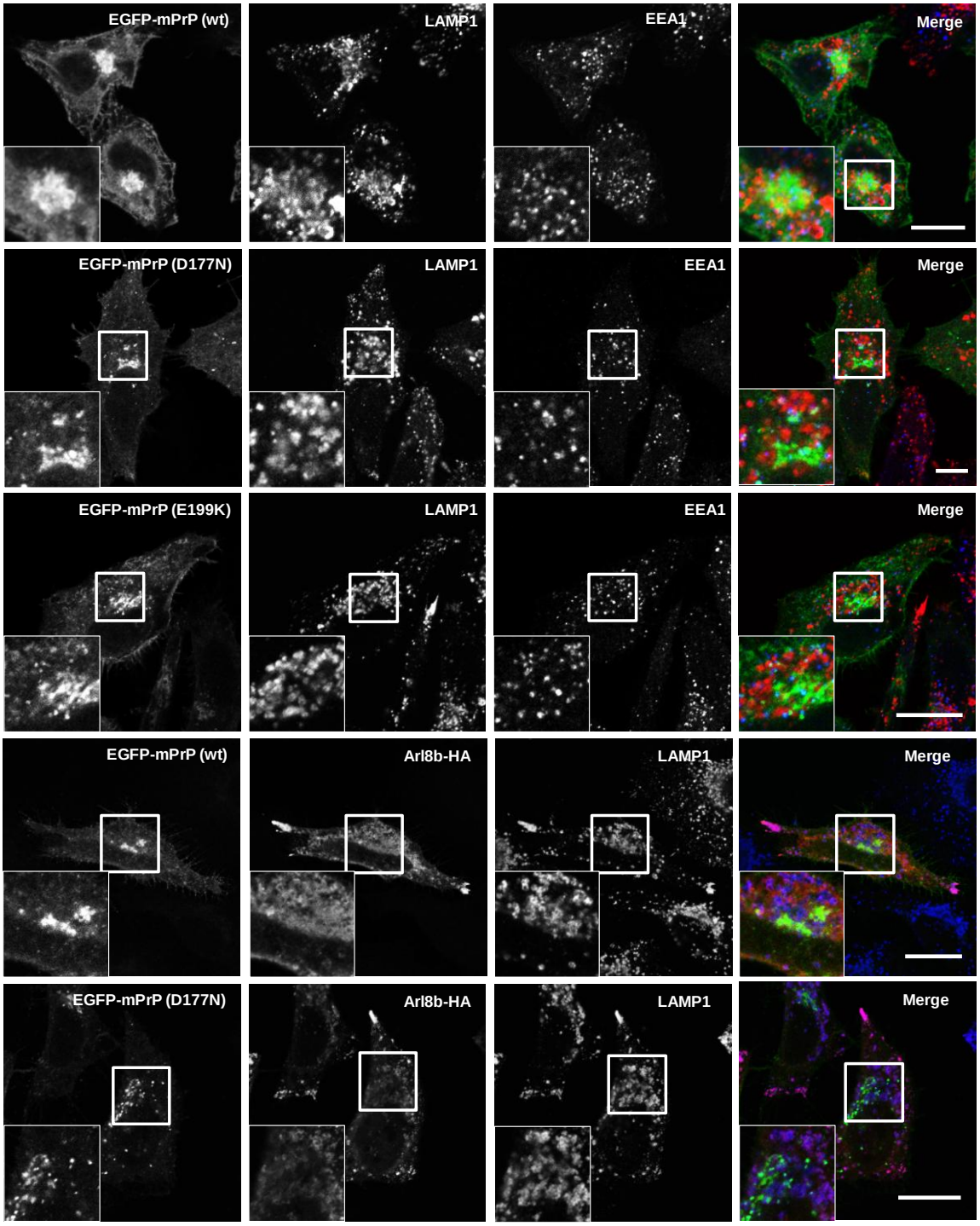

Figure 4.4 HeLa cells transfected with GFP-PrP-wild-type/-D177N/-E199K were analyzed for lysosomal/endosomal localization with confocal immunofluorescence microscopy. Scale bar = 10 µm.

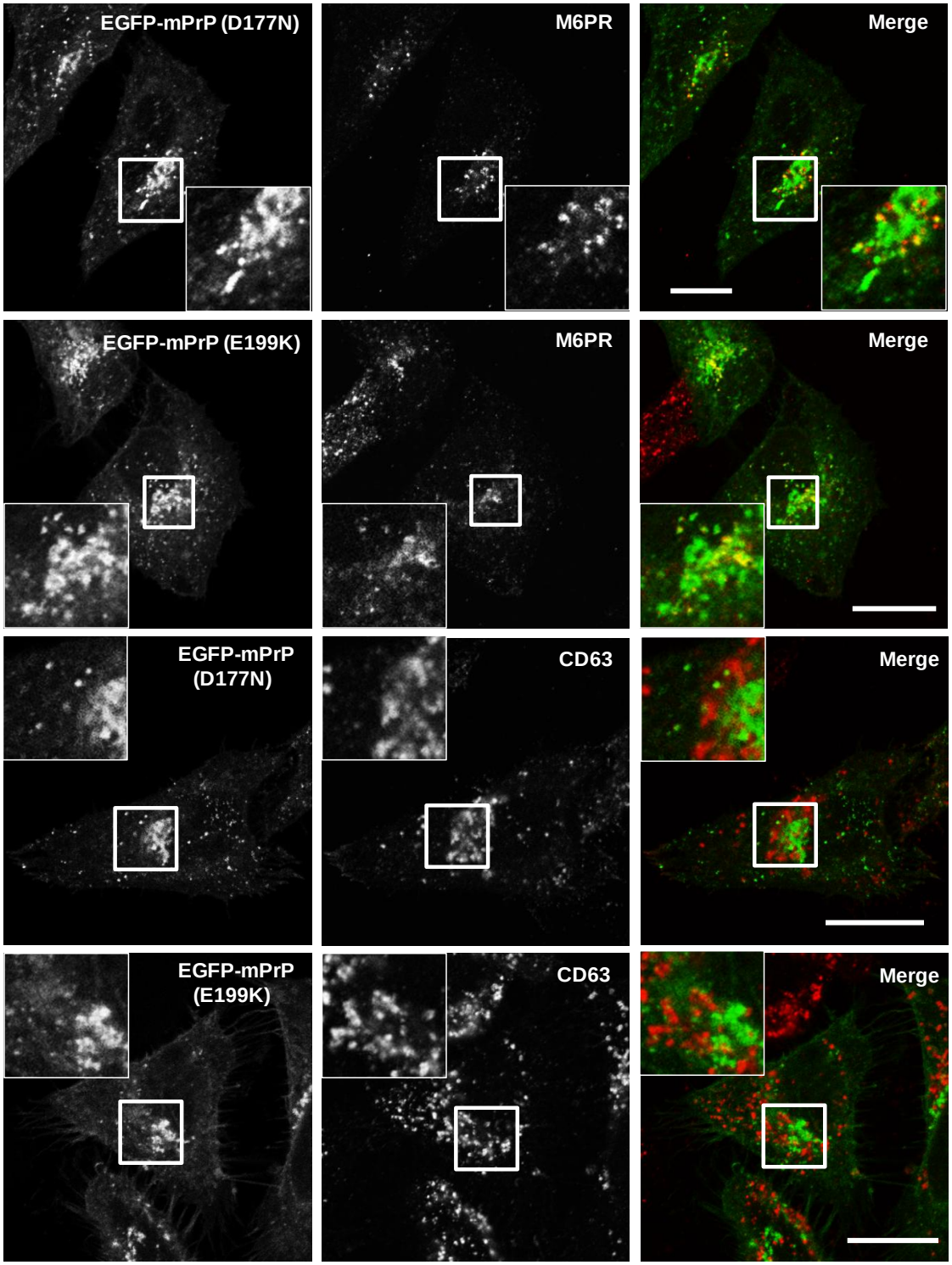

Figure 4.5 HeLa cells transfected with GFP-PrP-wild-type/-D177N/-E199K were analyzed for lysosomal/endosomal localization with confocal immunofluorescence microscopy. Scale bar = 10 µm.

system in HeLa cells (39). We envisage that the observed retention of PrP mutant isoforms in the cytoplasm in form of foci could be the aggregates of mutant PrP due to the retrotransloctaion of misfolded PrP from ER and might result into the compromised activity of proteasome. The altered localization of PrP^{D177N} and PrP^{E199K} could arise due to the aberrant intracellular trafficking of these mutants and might be accountable for ER stress induced by proteasome dysfunction and neural dysfunction.

4.5 FUTURE DIRECTION

Deciphering the conversion of cellular prion protein into scrapie isoform in the cell culture system is preferred because it preserve the necessary post-translation modification e.g. glycosylation and GPI-anchor that been shown to modify the conversion efficiency. Also, it offers the benefit of molecular crowding by providing the molecular cofactors and organelles that are believed to influence the transconversion (9). Since, PrP is abundantly expressed in neurons, the future experiments will be carried out in mouse neuroblastoma cell line (N2a) and primary neuronal cells. These preliminary results will act as prelude for our future research that includes decoding the exact mechanism of PrP endocytosis and the intracellular localization of various PrP mutants involved in familial disorders and the role of cytoplasmic chaperones. We would investigate the intracellular site for PrP^{C} and PrP^{Sc} interaction and role of exosomes in scrapie transmission to neighboring cells. We will also direct our efforts to identify the misfolded intermediates during the conformational conversion process and the involvement of endocytic compartments, as the low pH in these organelles might have considerable impact on structural transition of PrP (31) and it would also complement the *in vitro* experiments that have previously shown the ability of recombinant PrP to form protease resistant fibrils at low pH (40).

4.6 REFERENCES

1. Stahl, N., Borchelt, D. R., Hsiao, K., and Prusiner, S. B. (1987) Scrapie prion protein contains a phosphatidylinositol glycolipid. *Cell* **51**, 229-240
2. Ford, M. J., Burton, L. J., Li, H., Graham, C. H., Frobert, Y., Grassi, J., Hall, S. M., and Morris, R. J. (2002) A marked disparity between the expression of prion protein and its message by neurones of the CNS. *Neuroscience* **111**, 533-551

3. Chiesa, R., and Harris, D. a. (2009) Fishing for prion protein function. *PLoS Biology* **7**, 0439-0443
4. Prusiner, S. B. (1998) Prions. *Proc Natl Acad Sci U S A* **95**, 13363-13383
5. Prusiner, S. B. (1982) Novel proteinaceous infectious particles cause scrapie. *Science (New York, N.Y.)* **216**, 136-144
6. Prusiner, S. B. (1994) Biology and genetics of prion diseases. *Annu Rev Microbiol* **48**, 655-686
7. Aguzzi, A., Sigurdson, C., and Heikenwaelder, M. (2008) Molecular mechanisms of prion pathogenesis. *Annu Rev Pathol* **3**, 11-40
8. Campana, V., Sarnataro, D., and Zurzolo, C. (2005) The highways and byways of prion protein trafficking. *Trends in cell biology* **15**, 102-111
9. Harris, D. a. (1999) Cell biological studies of the prion protein. *Current issues in molecular biology* **1**, 65-75
10. Lehmann, S., and Harris, D. a. (1996) Two mutant prion proteins expressed in cultured cells acquire biochemical properties reminiscent of the scrapie isoform. *Proceedings of the National Academy of Sciences of the United States of America* **93**, 5610-5614
11. Ma, J., and Lindquist, S. (2001) Wild-type PrP and a mutant associated with prion disease are subject to retrograde transport and proteasome degradation. *Proceedings of the National Academy of Sciences* **98**, 14955-14960
12. Ivanova, L., Barmada, S., Kummer, T., and Harris, D. a. (2001) Mutant prion proteins are partially retained in the endoplasmic reticulum. *The Journal of biological chemistry* **276**, 42409-42421
13. Prado, M. A., Alves-Silva, J., Magalhaes, A. C., Prado, V. F., Linden, R., Martins, V. R., and Brentani, R. R. (2004) PrPc on the road: trafficking of the cellular prion protein. *J Neurochem* **88**, 769-781
14. Taylor, D. R., and Hooper, N. M. (2007) The low-density lipoprotein receptor-related protein 1 (LRP1) mediates the endocytosis of the cellular prion protein. *Biochem J* **402**, 17-23
15. Shyng, S. L., Huber, M. T., and Harris, D. A. (1993) A prion protein cycles between the cell surface and an endocytic compartment in cultured neuroblastoma cells. *J Biol Chem* **268**, 15922-15928

16. Shyng, S. L., Heuser, J. E., and Harris, D. A. (1994) A glycolipid-anchored prion protein is endocytosed via clathrin-coated pits. *J Cell Biol* **125**, 1239-1250
17. Madore, N., Smith, K. L., Graham, C. H., Jen, A., Brady, K., Hall, S., and Morris, R. (1999) Functionally different GPI proteins are organized in different domains on the neuronal surface. *EMBO J* **18**, 6917-6926
18. Laine, J., Marc, M. E., Sy, M. S., and Axelrad, H. (2001) Cellular and subcellular morphological localization of normal prion protein in rodent cerebellum. *Eur J Neurosci* **14**, 47-56
19. Shyng, S. L., Moulder, K. L., Lesko, A., and Harris, D. A. (1995) The N-terminal domain of a glycolipid-anchored prion protein is essential for its endocytosis via clathrin-coated pits. *J Biol Chem* **270**, 14793-14800
20. Lee, K. S., Magalhaes, A. C., Zanata, S. M., Brentani, R. R., Martins, V. R., and Prado, M. A. (2001) Internalization of mammalian fluorescent cellular prion protein and N-terminal deletion mutants in living cells. *J Neurochem* **79**, 79-87
21. Nunziante, M., Gilch, S., and Schatzl, H. M. (2003) Essential role of the prion protein N terminus in subcellular trafficking and half-life of cellular prion protein. *J Biol Chem* **278**, 3726-3734
22. Vey, M., Pilkuhn, S., Wille, H., Nixon, R., DeArmond, S. J., Smart, E. J., Anderson, R. G., Taraboulos, A., and Prusiner, S. B. (1996) Subcellular colocalization of the cellular and scrapie prion proteins in caveolae-like membranous domains. *Proceedings of the National Academy of Sciences* **93**, 14945-14949
23. Harmey, J., Doyle, D., Brown, V., and Rogers, M. (1995) The cellular isoform of the prion protein, PrPc, is associated with caveolae in mouse neuroblastoma (N2a) cells. *Biochemical and biophysical research communications* **210**, 753-759
24. Kaneko, K., Vey, M., Scott, M., Pilkuhn, S., Cohen, F. E., and Prusiner, S. B. (1997) COOH-terminal sequence of the cellular prion protein directs subcellular trafficking and controls conversion into the scrapie isoform. *Proceedings of the National Academy of Sciences* **94**, 2333-2338
25. Peters, P. J., Mironov, A., Peretz, D., van Donselaar, E., Leclerc, E., Erpel, S., DeArmond, S. J., Burton, D. R., Williamson, R. A., and Vey, M. (2003) Trafficking of prion proteins through a caveolae-mediated endosomal pathway. *The Journal of cell biology* **162**, 703-717

26. Marella, M., Lehmann, S., Grassi, J., and Chabry, J. (2002) Filipin prevents pathological prion protein accumulation by reducing endocytosis and inducing cellular PrP release. *Journal of Biological Chemistry* **277**, 25457-25464
27. Gorodinsky, A., and Harris, D. A. (1995) Glycolipid-anchored proteins in neuroblastoma cells form detergent-resistant complexes without caveolin. *The Journal of cell biology* **129**, 619-627
28. Parkin, E. T., Hussain, I., Turner, A. J., and Hooper, N. M. (1997) The Amyloid Precursor Protein Is Not Enriched in Caveolae-Like, Detergent-Insoluble Membrane Microdomains. *Journal of neurochemistry* **69**, 2179-2188
29. Sunyach, C., Jen, A., Deng, J., Fitzgerald, K. T., Frobert, Y., Grassi, J., McCaffrey, M. W., and Morris, R. (2003) The mechanism of internalization of glycosylphosphatidylinositol-anchored prion protein. *The EMBO journal* **22**, 3591-3601
30. Walmsley, A. R., Zeng, F., and Hooper, N. M. (2003) The N-terminal region of the prion protein ectodomain contains a lipid raft targeting determinant. *The Journal of biological chemistry* **278**, 37241-37248
31. Magalhães, A. C., Silva, J. A., Lee, K. S., Martins, V. R., Prado, V. F., Ferguson, S. S., Gomez, M. V., Brentani, R. R., and Prado, M. A. (2002) Endocytic intermediates involved with the intracellular trafficking of a fluorescent cellular prion protein. *Journal of Biological Chemistry* **277**, 33311-33318
32. Nichols, B. J., Kenworthy, A. K., Polishchuk, R. S., Lodge, R., Roberts, T. H., Hirschberg, K., Phair, R. D., and Lippincott-Schwartz, J. (2001) Rapid cycling of lipid raft markers between the cell surface and Golgi complex. *The Journal of cell biology* **153**, 529-542
33. Grünfelder, C. G., Engstler, M., Weise, F., Schwarz, H., Stierhof, Y.-D., Morgan, G. W., Field, M. C., and Overath, P. (2003) Endocytosis of a glycosylphosphatidylinositol-anchored protein via clathrin-coated vesicles, sorting by default in endosomes, and exocytosis via RAB11-positive carriers. *Molecular biology of the cell* **14**, 2029-2040
34. Abrami, L., Liu, S., Cosson, P., Leppla, S. H., and van der Goot, F. G. (2003) Anthrax toxin triggers endocytosis of its receptor via a lipid raft–mediated clathrin-dependent process. *The Journal of cell biology* **160**, 321-328

35. Lee, K. S., Magalhães, A. C., Zanata, S. M., Brentani, R. R., Martins, V. R., and Prado, M. A. (2001) Internalization of mammalian fluorescent cellular prion protein and N-terminal deletion mutants in living cells. *Journal of neurochemistry* **79**, 79-87
36. Lorenz, H., Windl, O., and Kretzschmar, H. A. (2002) Cellular phenotyping of secretory and nuclear prion proteins associated with inherited prion diseases. *Journal of Biological Chemistry* **277**, 8508-8516
37. Van der Kamp, M. W., and Daggett, V. (2009) The consequences of pathogenic mutations to the human prion protein. *Protein Engineering Design and Selection*, gzp039
38. Garg, S., Sharma, M., Ung, C., Tuli, A., Barral, D. C., Hava, D. L., Veerapen, N., Besra, G. S., Hacohen, N., and Brenner, M. B. (2011) Lysosomal trafficking, antigen presentation, and microbial killing are controlled by the Arf-like GTPase Arl8b. *Immunity* **35**, 182-193
39. Anderson, R. G. (1998) The caveolae membrane system. *Annual review of biochemistry* **67**, 199-225
40. Swietnicki, W., Petersen, R., Gambetti, P., and Surewicz, W. K. (1997) pH-dependent stability and conformation of the recombinant human prion protein PrP (90–231). *Journal of Biological Chemistry* **272**, 27517-27520

Chapter 5

Nanoscale Fluorescence Imaging of Single Amyloid Fibrils using Near-field Scanning Optical Microscopy

This work has been published in *Journal of Physical Chemistry Letters*.

V. Dalal, M. Bhattacharya, D. Narang, P.K. Sharma and S. Mukhopadhyay "Nanoscale Fluorescence Imaging of Single Amyloid Fibrils" ***J. Phys. Chem. Lett.*** 2012, *3*, 1783-1787.

5.1 INTRODUCTION

Amyloid fibril formation from variety of proteins is associated with a number of debilitating human diseases such as Alzheimer's, Parkinson's, Huntington's and numerous systemic amyloidosis (1-7). The salient enigmatic features of amyloids such as amyloid polymorphism and toxicity are believed to be encrypted in the supramolecular structure of amyloids. Recent discoveries have indicated that amyloids may also have beneficial functional roles in a variety of organisms including humans. This class of amyloids having biologically functional roles is termed as "functional amyloid" (8-10). The underlying molecular mechanisms by which amyloids and their precursors are involved in inducing functional consequences, cellular toxicity and membrane disruption eventually leading to cell death remain elusive. Our knowledge about infectious and functional amyloids is limited largely due to the fact that conventional optical microscopy does not allow us to directly monitor the related processes at a high spatial-resolution. The dimensions of amyloid aggregates fall in the nanoscopic regime and therefore conventional microscopy is inadequate in mapping the supramolecular architecture of the aggregates and their complexes with membrane and other cellular components. High resolution scanning probe microscopy (SPM)-based imaging technique such as atomic force microscopy (AFM) has been extremely useful in gaining in-depth insights into the nanoscale morphology of prions and various kinds of aggregates and fibrils that could be identified and characterized at various different stages of amyloid assembly (11-14). However, AFM imaging techniques do not allow us to access the wealth of structural insights that are obtainable from optical microscopy that has been extremely successful in unraveling a wide variety of biological assemblies, interactions, bindings and co-localizations down to single molecule resolution. The traditional (far-field) optical microscopy suffers from a major drawback because the far-field (lens-based) focusing creates a focal spot that is fundamentally limited by the optical diffraction-limit (usually $\geq$ 250 nm) and poses a bottleneck in the high resolution imaging to structurally characterize and to localize amyloid fibrils with respect to the cell membrane and other cellular components. Therefore, there is a pressing need to apply and adapt non-traditional optical imaging technologies that will have capabilities in simultaneously mapping fibrils at a high spatial resolution while retaining the wealth of optical (fluorescence) information. Such a methodology would improve our present understanding of prions and amyloids. One of the ways to perform such high resolution nanoscale imaging is to utilize SPM-based methods such as near-field scanning optical microscopy (NSOM) that breaks the far-field diffraction limit and allows both topographic

and optical mapping simultaneously (15-25). Near-field imaging using both fluorescence and infrared has been previously applied to many biologically relevant nanoscale systems including protein fibrils (18-25). Recently, direct stochastic optical reconstruction microscopy (dSTORM) has been applied to achieve a nanoscopic resolution in fluorescence imaging of β-amyloid fibrils (26).

In this work, we have adapted and developed super-resolution fluorescence imaging method to look into the amyloid architecture using near-field scanning optical microscopy with the future aim to investigate the basis of prion strains and prions species barrier. Here, we have used fluorescently stained amyloid fibrils derived from disease-associated human β_2-microglobulin to establish the potentials of the near-field scanning fluorescence microscopy.

5.2 EXPERIMENTAL SECTION

5.2.1 Expression and purification of human β_2-microglobulin

Escherichia coli BL21 (DE3) cells transformed with pET-23a plasmid containing N-terminal His_6-tagged human β_2-microglobulin were used for protein expression. The transformed cells were grown at 37 ^oC in Luria Bertini broth/ampicillin medium containing 0.1 mg/mL of ampicillin. At an OD_{600nm} = 0.6, protein expression was induced with 1 mM final concentration of isopropyl-β-D-thiogalactopyranoside (IPTG). After 5-6 hours of induction, cells were harvested by centrifugation and re-suspended in lysis buffer. The protein was expressed in inclusion bodies (IB). IB, solubilized in 0.1 M Na_2HPO4, 8 M urea and 10 mM Tris-HCl pH 8.0 buffer, were purified on a Ni-NTA (GE) column. The protein was refolded in 10 mM Tris-HCl pH 8.0 buffer by dialysis and purified further by fast protein liquid chromatography on an anion exchange (Q-sepharose from GE) column. The purity and identity of the protein were analyzed by SDS-PAGE and MALDI-TOF mass spectrometry. Accurate protein concentration was determined by measuring the absorbance at 280 nm using reported molar extinction coefficient of 19,850 M^{-1} cm^{-1}. The purified protein was stored in 10 mM Tris pH 8.0 buffer at -20 ^oC.

5.2.2 Preparation of amyloid fibrils *in vitro*

Conversion of monomeric human β_2-microglobulin into amyloid fibrils was brought by diluting the protein stock solution using Gly-HCl pH 2.5 buffer to which sodium chloride (NaCl) solution (2 M) was added and the pH of the resulting solution was adjusted to 2.5(±0.01). The final protein, buffer and salt concentrations were 50 µM, 20 mM and 200

mM, respectively in a total volume of 2 mL. The fibrillization was carried out at room temperature (25 ^{o}C) with moderate agitation on a magnetic stirrer. Mature fibrils were formed in 44 hours which were characterized using a fluorescent dye namely, Nile Red (Sigma).

5.2.3 Nile Red binding experiments

The formation of β_2m amyloid fibrils was established by an increase in the fluorescence intensity of an amyloid specific dye, Nile Red, upon binding to the amyloid fibrils. A stock solution of Nile Red, 10 mM, was prepared in dimethylsulfoxide (DMSO; Merck) and stored at 4 ^{o}C. For Nile Red binding experiments, the steady state fluorescence spectra were recorded at 25 ^{o}C on Chirascan spectrometer (Applied Photophysics, Leatherhead, United Kingdom) equipped with a high-gain visible photomultiplier tube. An aliquot from the aggregation mixture was withdrawn after 44 h to which an aliquot of Nile Red stock solution was added and the final concentration of Nile Red was 50 µM. The resulting solution was taken in a quartz cuvette of 10 mm path length and the Nile Red fluorescence emission spectra were collected from 520-700 nm using an excitation wavelength of 488 nm with excitation and emission band pass of 2 nm and 3 nm, respectively. The scan rate was 0.5 nm/s and the final spectrum was averaged over 8 scans. The steady state fluorescence anisotropy (r_{ss}) of Nile Red was estimated using the following relationship:

$$r_{ss} = (I_{||} - I_{\perp} G) / (I_{||} - 2I_{\perp} G) \quad \text{(Eq. 5.1)}$$

where, $I_{||}$ and $I_{\perp}$ are fluorescence intensities collected using parallel and perpendicular geometry of the polarizer, respectively and the perpendicular components were corrected using a G-factor. The graphs were plotted using commercially available Origin Pro Version 8 software.

5.2.4 Atomic force microscopy (AFM) imaging

The amyloid fibrils of β_2m were prepared as described above. Prior to AFM imaging, the aggregation buffer (20 mM Gly-HCl, pH 2.5) was filtered using 0.22 µm membrane filter procured from Millipore. An aliquot from the aggregation mixture was withdrawn after 44 h and diluted 200-fold using the filtered aggregation buffer. 10 µL of the diluted fibril sample was loaded on freshly cleaved, buffer-washed muscovite mica (Grade V-4 mica from SPI, PA, USA) and allowed to incubate for 15 minutes. Following incubation, the mica surface was washed once with 20 µL of the aggregation buffer and dried under a gentle stream of ultrapure nitrogen gas for 30 minutes. AFM images were obtained on a MultiView 2000

instrument (Nanonics Imaging Ltd., Jerusalem, Israel) operating in the non-contact mode and normal force tuning-fork, phase feedback technique. For fibril imaging, Cr-coated cantilevered glass probe of diameter ~10 nm oscillating at a resonance frequency of 31.9 kHz was used. Images were collected in sample scanning configuration on Quartz software (provided with the MultiView) in a scan area of 5x5 µm at a resolution of 400x400 pixels with a Z magnification of 1:15 and slope compensation. An external input gain of 200 was used and the individual gain parameters were adjusted in such a way so that the total gain was ~67. During the scans, the sample delay and line delay were kept at 3 ms and 10 ms, respectively with the number of substeps as 1. The images were further processed using WSxM software (for details, see 5.2.6).

5.2.5 Near-field scanning optical microscopy (NSOM) imaging

For NSOM imaging experiments, the sample was prepared as follows: An aliquot of Nile Red stock solution (10 mM) was added to 10 µL of the mature fibril mixture to a final Nile Red concentration of 50 µM and the fluorescent dye-stained solution was incubated for 10 minutes at 25 ^{o}C. Following incubation, the solution was diluted 200-fold with the filtered aggregation buffer (Gly-HCl pH 2.5, 20 mM), quickly deposited on freshly cleaved, buffer washed mica surface and allowed to incubate again for 15 minutes. After 15 minutes, the mica was washed once with 20 µL of filtered aggregation buffer and dried under a gentle stream of ultrapure nitrogen gas for 30 minutes. During the entire course of sample preparation followed by deposition on the mica and subsequent drying, utmost care was taken to protect the sample from light in order to prevent photobleaching of Nile Red. The AFM and correlated NSOM images were obtained simultaneously on a MultiView 2000 instrument (Nanonics Imaging Ltd., Jerusalem, Israel), operating in the non-contact mode and normal force tuning-fork, phase feedback technique. Cr and Au-coated cantilevered glass NSOM probe of aperture ~100 nm oscillating at a resonance frequency of 42.25 kHz was used in transmission mode for sample scans. The 488 nm line of a tunable Ar-ion laser (Modu-Laser) was coupled with the NSOM probe optical fiber to illuminate Nile Red during imaging. The emitted fluorescence was collected using far-field optics comprising a 50X long working distance objective (Nikon, Japan), mounted on a dual (upright and inverted) Olympus microscope (integrated with the MultiView), and an avalanche photodiode (APD). Appropriate optical filters, namely 488 nm notch and 550 nm long pass filters, were placed before the APD to block the scattered excitation light and allow the fluorescence emission to pass through. The AFM-NSOM correlated images were obtained on Quartz software in a

scan area of 10x10 µm at a resolution of 320x320 pixels with a Z magnification of 1:7 under offset sample scanning configuration. During the scans, the sample delay and line delay were kept at 4 ms and 10 ms, respectively with the number of substeps as 50. The images were further processed using WSxM software (for details, see 5.2.6).

5.2.6 Image analysis

All the AFM and AFM-NSOM correlated images, collected on Quartz software, were imported and processed further using WSxM 4.0 Develop 11.6 image software provided with the instrument. The AFM images were processed using parabola flatten and small contrast stretch following which the respective height profiles were obtained. The AFM-NSOM correlated images, collected simultaneously, were processed using offset flattened and smoothened using Gaussian smooth kernel 2. For NSOM images, extra rain color palette with a brightness and contrast of 1.998 and 0.9386, respectively were used for better visualization. The AFM-NSOM 3D-collages were obtained by overlaying the processed AFM image on the respective NSOM image and vice-versa. Further image analysis was carried out for individual fibrils that are well separated from each other. Simultaneous (multiple) profiling of AFM-NSOM correlated images was employed to obtain the height (from AFM) and fluorescence (from NSOM) profiles from individual fibrils. Multiple line profiling yielded peaks corresponding to both height and fluorescence across the width of an individual fibril. These peaks were integrated to obtain the total cross-sectional area and the total fluorescence along the profile line across the width of the fibril. The brightness per unit area (kHz/nm^2) was estimated from the plots. The mean fluorescence brightness and standard deviations associated with NSOM image analysis of well-separated individual fibrils are given in Table 1. Several multiple profiling was carried out by traversing along the length of a single fibril. The number of events (or occurrence) for a given fibril was calculated using a binning size of 1 kHz/nm^2 to build the histograms. And this process was repeated for several individual fibrils. Additionally, we have calculated the ratio of the fluorescence maxima over the height maxima expressed in kHz/nm. In this case, the binning size was 0.25 kHz/nm to build the histograms (Figure 5.5). The histograms were plotted using Origin Pro Version 8.

5.3 RESULTS AND DISCUSSION

We used human β_2-microglobulin as a model amyloid-forming protein that has been implicated in dialysis-related amyloidosis (27-29). β_2-microglobulin is a β-rich protein in its native state (Figure 5.1a) and forms amyloid fibrils under destabilizing conditions such as at low pH (27-29). The reasons for choosing β_2-microglobulin are as follows: (i) It is an amyloid disease-related protein; (ii) Amyloid fibrils formed *in vitro* from the recombinantly expressed protein in *Escherichia coli* resemble those found in patients suffering from amyloidosis; (iii) Amyloid formation from this protein is very well characterized by various biophysical tools; (iv) The formation of amyloid fibrils of desired nanoscale morphology is quite reproducible under given conditions.

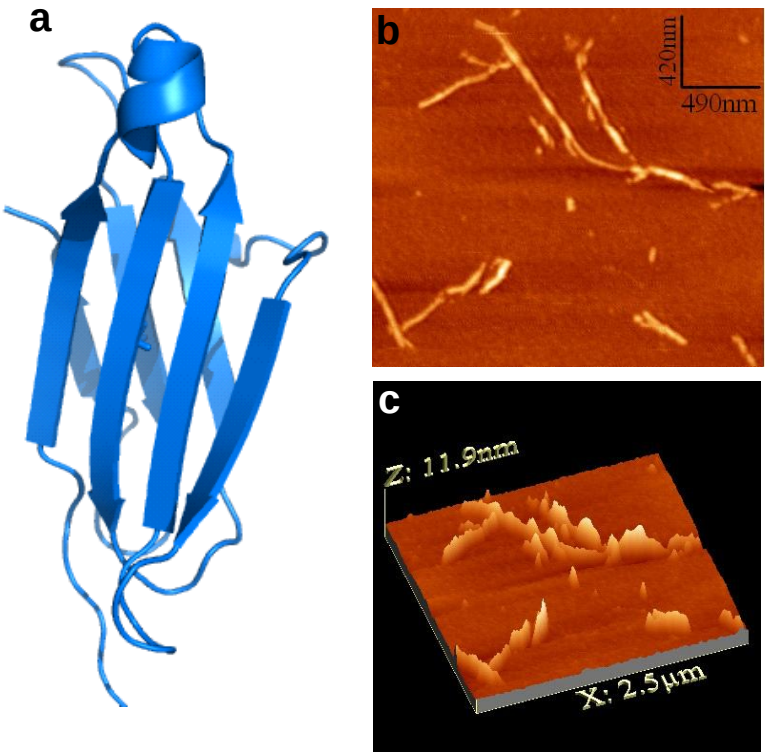

Figure 5.1 Amyloid fibril formation from human β_2-microglobulin. (a) Crystal structure of human β_2-microglobulin generated using Pymol (Delano Scientific LLC, CA, USA) from protein data bank (PDB ID: 1LDS). (b) AFM image of amyloid fibrils prepared at low pH. (c) 3D AFM topography showing the height profile of fibrils.

The AFM image reveals that the fibrils are ~ 10 nm wide and several hundreds of nm long (Figure 5.1b, c). After characterizing the nanoscale morphology of the fibrils formed under our laboratory condition, we embarked upon studies aimed at optically imaging these fibrils

using fluorescence-mode NSOM. In order to make the fibrils fluorescent, one can use a fluorescent dye that intercalates in the cross-β structural assembly of amyloid fibrils. Thioflavin-T (ThT) is one such dye that has been used extensively to detect amyloid formation as well as to image the matured fibrils (30-33). However, ThT suffers from many drawbacks as follows. (i) ThT is charged and can bind non-specifically to other non-amyloid (amorphous) protein aggregates (31); (ii) It cannot be used to stain amyloid fibrils that are formed at low pH and disaggregate at neutral pH (32); (iv) It is not a suitable dye for single molecule imaging because of its low fluorescence quantum yield (33); (v) Additionally, this fluorophore cannot be excited using commonly available laser lines such as 488 nm, 532 nm and 633 nm since it fluoresces at ~ 482 nm upon binding to amyloid fibrils. To circumvent the aforementioned shortcomings, we used a neutral fluorescent dye namely Nile Red that is known to be more specific for amyloid fibrils (34,35), binds non-covalently to fibrils and fluoresces over a wide range of pH, demonstrates the sensitivity in nanoscale fluorescence imaging (36) and can be excited using a commonly available laser line such as 488 nm of Ar^+ laser. After preparing amyloid fibrils from β_2-microglobulin, we have fluorescently stained the fibrils using Nile Red. The Nile red binding to the fibrils was indicated by the significant enhancement in its quantum yield and fluorescence anisotropy (Figure 5.2). The Nile Red stained fibrils were deposited onto freshly cleaved mica and used for NSOM studies.

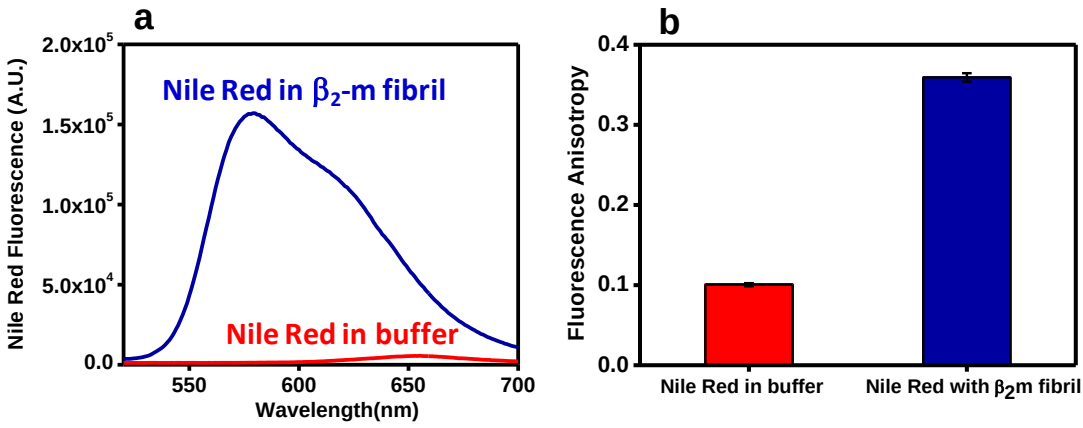

Figure 5.2 Nile red binding with β_2-microglobulin fibrils. (a) Fluorescence spectra of Nile Red in pH 2.5 buffer (red) and bound to amyloid fibrils (blue). (b) The steady-state fluorescence anisotropy of Nile Red in amyloid fibrils was much higher compared to that in water.

The experimental set up is similar to what has been described earlier (15-22). In our NSOM set up, the 488 nm laser is passed through a metal-coated tapered optical fiber tip

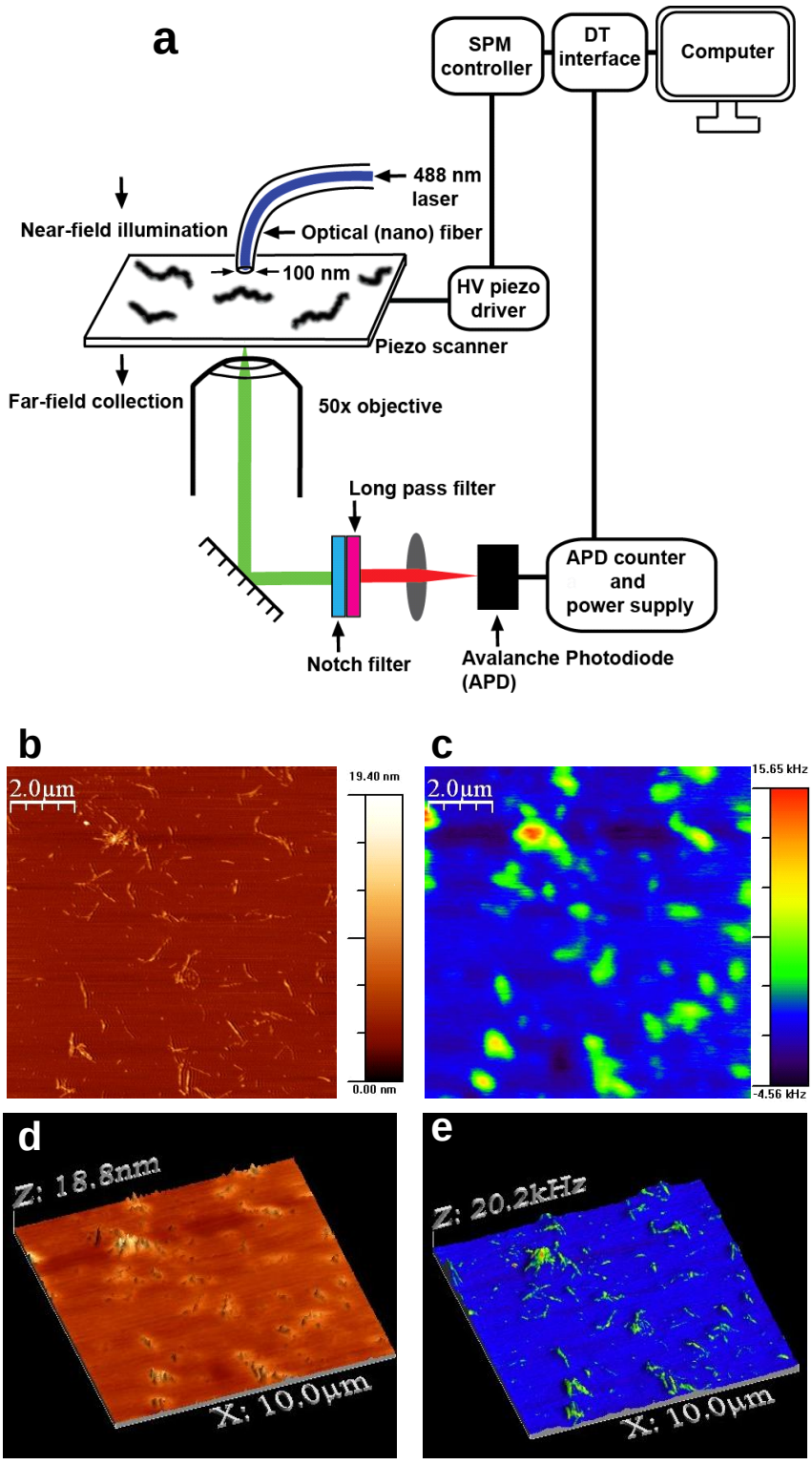

Figure 5.3 NSOM imaging of β_2-microglobulin amyloid fibrils. (a) The schematic of the experimental set up. (b) Topographic (AFM) and (c) the corresponding fluorescence (NSOM) image of fibrils non-covalently stained with Nile Red. 3D overlays of (d) NSOM fluorescence on AFM topography and (e) AFM topography on NSOM fluorescence, showing they are highly correlated.

having an aperture of ~ 100 nm (Figure 5.3a). The fiber is brought close (~ 10 nm) to the surface of the sample. The light output from the fiber being composed of evanescent waves rather than propagating waves is able to illuminate the 'near-field' region that is now limited by the aperture of the fiber but not by the wavelength of the incident light. Therefore, the resolution is substantially higher compared to the diffraction-limit as described previously (18-22). We have used transmission mode fluorescence NSOM and collected fluorescence emitted from fluorescent fibrils using far-field optics to image the fibrils. The collected fluorescence is passed through a notch filter and an appropriate long pass filter and is detected using a highly sensitive avalanche photodiode (APD). The feedback signal is used to generate topographic map (AFM) and the corresponding fluorescence map is obtained from the emitted photons detected by the APD during scanning.

The scanning of the mica surface, containing fluorescent fibrils, using a fiber probe generates topographic as well as fluorescence image simultaneously. Figure 5.3b shows the AFM topography while Figure 5.3c shows the corresponding NSOM fluorescence image. These images are highly spatially correlated. This is further illustrated in 3D overlays of both topographic and fluorescence images (Figure 5.3d, e). Simultaneous line profiling of these images yielded the plots of height (in nm) and fluorescence intensity (in kHz) along the line drawn against the width of a fibril (Figure 5.4).

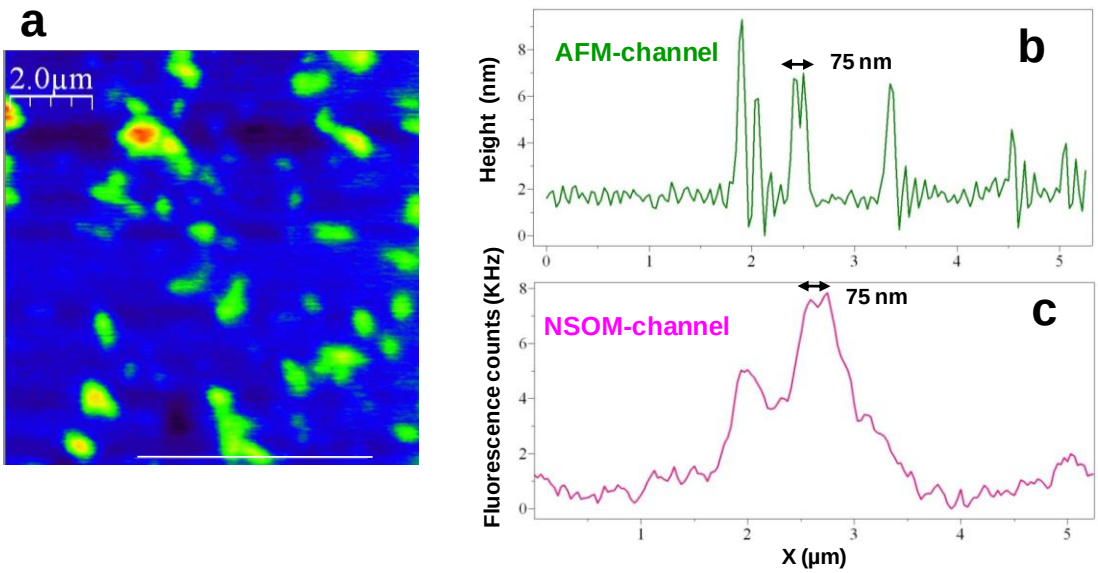

Figure 5.4 Simultaneous analysis of topography and fluorescence features of two amyloid fibrils obtained from NSOM imaging. (a) NSOM fluorescence image of fibrils showing few well-separated individual fibrils. (b) AFM topography and (c) NSOM fluorescence profile along a white line in panel a showing two fibrils that are separated by ~ 75 nm can be distinguished by NSOM.

In our NSOM image, we were able to resolve both the topographic and fluorescence features of two fibrils that are separated by only ~ 75 nm (shown by double-headed arrows in Figure 5.4b, c). Our measurements illuminate the fluorescence map of amyloid fibrils at the nanoscopic spatial resolution that is well beyond the diffraction limit and provide a useful handle to visualize and interrogate the supramolecular structural distribution of individual amyloid fibrils using optical information (Figure 5.5b).

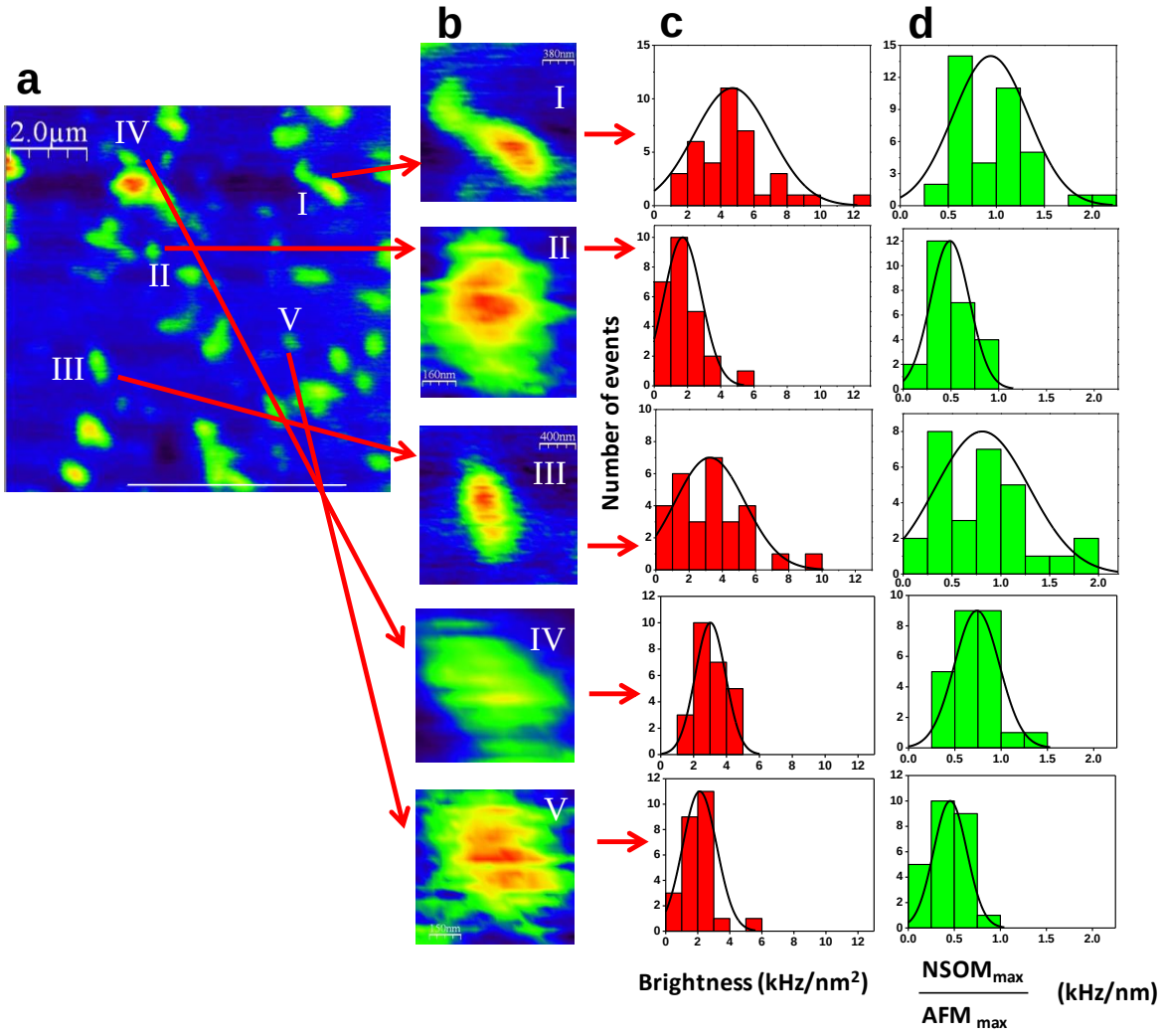

Figure 5.5 Simultaneous analysis of NSOM fluorescence of individual amyloid fibrils. (a) NSOM fluorescence image of fibrils showing a few well-separated individual fibrils (I-V). (b) The zoomed images of individual fluorescent fibrils. (c) The brightness (kHz/nm^2) and (c) the ratio (kHz/nm) analysis of the individual fluorescent fibrils.

After establishing the spatial correlation between the fibril topography and fluorescence, we next examined whether the fluorescence brightness along the length of an individual fibril

is uniform or not. Additionally, we asked whether or not the observed brightness among different fibrils is uniformly distributed. Our methodology allows us to map out both nanoscopic height profile and fluorescence counts of individual fibrils. Any heterogeneity in the fluorescence brightness is likely to indicate the diversity in structural distribution of these fibrils since the amyloid reporter, Nile Red, may have different binding affinities depending on the supramolecular packing of the cross-β structure within amyloid fibrils. We performed the analysis in the following way. As we have already mentioned that (concurrent) multiple profiling provides both topographic and fluorescence peaks across the width of a fibril, we traversed along the length of the fibril to obtain simultaneous profiles of both height and fluorescence. The area integration of the height profile yielded the cross-sectional area whereas the integration of the fluorescence profile yielded the total fluorescence counts emitted from the given cross-section of the fibrils. Therefore, the ratio of total fluorescence to the area would yield the fluorescence brightness per unit cross-sectional area (in kHz/nm^2). This analysis was performed for individual fibrils and the fluorescence brightness per unit area was plotted against the number of events in the form of a histogram (Figure 5.5). This plot reveals that there is a considerable variation of the brightness along the length of a single fibril indicating a possibility of conformational distribution within the fibril. As suggested earlier (18-22), there might be some contribution from the orientational distributions and the metal (coating of the tip) induced alterations of both radiative and nonradiative decay rates of fluorophores bound to the fibrils. These effects are likely to contribute to the broadening of the brightness distribution of an individual fibril.

Table 5.1 The mean fluorescence brightness and standard deviations associated with NSOM image analysis of five individual fibrils shown in Figure 5.5

Fibrils	Brightness per unit area (kHz/nm^2)	Ratio of $NSOM_{max}$ to AFM_{max} (kHz/nm)
I	4.70 ± 2.31	0.94 ± 0.39
II	1.71 ± 1.13	0.49 ± 0.20
III	3.25 ± 2.10	0.81 ± 0.49
IV	3.02 ± 0.92	0.74 ± 0.24
V	2.12 ± 1.07	0.46 ± 0.18

Next, we analyzed the mean brightness and its distribution among different fibrils (Fibrils I-V in Figure 5.5). This analysis indicated that the mean brightness ranged from 1.7 ± 1.1 to 4.7 ± 2.3 kHz/nm^2 among five isolated individual fibrils (Table 5.1). The brightness distribution for five different fibrils in the form of histograms demonstrates considerable variability that is likely to be the result of structural heterogeneity among different individual amyloid fibrils (Figure 5.5c). Since presumably a large number of Nile Red molecules are bound to each of the fibril and metal-induced alterations in fluorescence are expected to be similar among the fibrils, we believe that the differences in the average brightness among the fibrils are indicative of heterogeneous structural distributions and hence variations in the supramolecular packing of the cross-β architecture. However, we would like to point out that the total area and the total fluorescence have convolutions of the tip used in these measurements. For example, the height profile is typically much sharper compared to the fluorescence profile that is limited by the aperture of the fiber (Figure 5.4b, c). Therefore, we also performed similar analysis using the ratio of the height and fluorescence peaks (in kHz/nm; the fluorescence maxima in NSOM fluorescence and height maxima in topography) that showed a similar trend with our brightness per unit area analysis (Figure 5.5d). We would like to point out that the maximum fluorescence to height ratio ($NSOM_{max}/AFM_{max}$) is devoid of convolutions of the tip since we are considering only the maxima in both height and fluorescence. This analysis also revealed the similar heterogeneous distribution and suggests the variability in amyloid structural packing among different fibrils.

5.4 CONCLUSION

In summary, here we have demonstrated nanoscale optical imaging of individual amyloid fibrils using fluorescence. There are several implications of our study presented here. An important achievement involves nanoscopic optical imaging and analysis of single fibrils using Nile Red as an amyloid-sensitive fluorescent reporter that is neutral and works over a wide range of pH and proteins. Additionally, the use of a commonly available laser line broadens significantly the scope of the NSOM methodology and makes amyloid-Nile Red system a very widely viable system for single fibril imaging. Therefore, taken together, this methodology will be applicable for the study of nearly all the amyloid systems formed *in vitro* or isolated from patients. Multi-parameter nanoscale structural and optical distribution analysis will be useful to investigate prion polymorphs that are believed to be enciphered in the protein conformation within the aggregates. We anticipate that this method holds promise

to detect conformational distributions and heterogeneity in the amyloids that are believed to correlate with the supramolecular packing of misfolded proteins within the fibrils that underlie the structural basis of the strain phenomenon in prion and amyloid biology. We also envision that this methodology coupled to a multi-color illumination and detection format would serve as a powerful tool to probe membrane-amyloid interactions on the cell-surface at the single fibril resolution. Additionally, the analysis combining both topographic and optical information can have incredible potentials in a broad range of surface imaging in biological nanoscopy.

5.5 REFERENCES

(1) Luheshi, L. M.; Crowther, D.C.; Dobson, C. M. Protein misfolding and disease: from the test tube to the organism. *Curr. Opin. Chem. Biol.* **2008**, *12*, 25-31.

(2) Chiti, F.; Dobson, C. M. Protein misfolding, functional amyloid and human disease. *Annu. Rev. Biochem*. **2006**,*75*, 333-366.

(3). Jahn, T.R.; Radford, S.E. Folding versus aggregation: polypeptide conformations on competing pathways. *Arch. Biochem. Biophys.* **2008**, *469*, 100-117.

(4) Eichner, T.; Radford, S.E. Diversity of assembly mechanisms of a generic amyloid fold. *Mol. Cell* **2011**, *43*, 8-18.

(5) Tycko, R. Molecular structure of amyloid fibrils: Insights from solid state NMR. *Q. Rev. Biophys*. **2006**, *39*, 1-55.

(6) Moreno-Gonzalez, I.; Soto, C. Misfolded protein aggregates: Mechanisms, structures and potential for disease transmission. *Semin. Cell Dev. Biol.* **2011**, *22*, 482−487.

(7) Lee, J.; Culyba, E.K.; Powers, E.T.; Kelly, J.W. Amyloid β forms fibrils by nucleated conformational conversion of oligomers. *Nat. Chem. Biol*. **2011**, *7*, 602-609.

(8) Eisenberg, D.; Jucker, M. The amyloid state of proteins in human diseases. Cell 2012, 148, 1188−11203.

(9) Shorter, J.; Lindquist, S. Prions as adaptive conduits of memory and inheritance. *Nat. Rev. Genet*. **2005**, *6*, 435-450.

(10) Fowler, D. M.; Koulov, W. E.; Balch, Kelly, J. W. Functional amyloid – from bacteria to humans. *Trends Biochem. Sci.* **2007**, *32*, 217-224.

(11) Ban, T.; Yamaguchi, K.; Goto, Y. Direct observation of amyloid fibril growth, propagation, and adaptation. *Acc. Chem. Res*. **2006**, *39*, 663-670.

(12) Adamcik, J.; Mezzenga, R. Adjustable twisting periodic pitch of amyloid fibrils. *Soft Matter* **2011**, *7*, 5437-5443.

(13) Lara, C.; Adamcik, J.; Jordens, S.; Mezzenga, R. General self-assembly mechanism converting hydrolyzed globular proteins into giant multistranded amyloid ribbons. *Biomacromolecules* **2011**, *12*, 1868–1875.

(14) Connelly, L.; Jang, H.; Teran Arce, F.; Ramachandran, S.; Kagan, B. L.; Nussinov, R.; Lal, R. Effects of point substitutions on the structure of toxic Alzheimer's β-amyloid channel: atomic force microscopy and molecular dynamics simulations. *Biochemistry* **2012,** *10*, 3031-3038.

(15) Betzig, E.; Trautman, J. K. Near-field optics: microscopy, spectroscopy, and surface modification beyond the diffraction limit. *Science* **1992**, *257*, 189-195.

(16) Betzig, E.; Chichester, R. J. Single molecules observed by near-field scanning optical microscopy. *Science* **1993,** *262*, 1422-1425.

(17) Trautman, J. K.; Macklin, J. J.; Brus, L. E.; Betzig, E. Near - field spectroscopy of single molecules at room temperature. *Nature* **1994**, *369*, 40-42.

(18) Dunn, R. C.; Allen, E. V.; Joyce, S. A. ; Anderson, G. A.; Xie X. S. Near-field fluorescent imaging of single proteins. *Ultramicroscopy* **1995**, *57*, 113-117.

(19) Xie, X. S.; Dunn, R. C. Probing single molecule dynamics. *Science* **1994**, *265*, 361-364.

(20) Xie, X. S. Single-molecule spectroscopy and dynamics at room temperature. *Acc. Chem. Res.* **1996**, *29*, 598-606.

(21) Lewis, A.; Taha, H.; Strinkovski, A.; Manevitch, A.; Khatchatouriants, A.; Dekhter, R.; Ammann, E. Near-field optics: from subwavelength illumination to nanometric shadowing. *Nat. Biotech.* **2003**, *21*, 1378-1386.

(22) de Lange, F.; Cambi, A.; Huijbens, R.; de Bakker, B.; Rensen, W.; Garcia-Parajo, M.; van Hulst, N.; Figdor C. G. Cell biology beyond the diffraction limit: near-field scanning optical microscopy. *J. Cell Sci.* **2001**, *114*, 4153-4160.

(23) Hinterdorfer, P.; Garcia-Parajo, F. M.; Dufrêne F. Y. Single-Molecule Imaging of Cell Surfaces Using Near-Field Nanoscopy. *Acc. Chem. Res.* **2012**, *45*, 327–336.

(24) Kitts, C. C.; Vanden Bout, D. A. Near-field scanning optical microscopy measurements of fluorescent molecular probes binding to insulin amyloid fibrils. *J. Phys. Chem. B*. **2009**,*113*, 12090-12095.

(25) Paulite, M.; Fakhraai, Z.; Li, I. T. S.; Gunari, N.; Tanur, A. E.; C. Walker, G. C. Imaging Secondary structure of individual amyloid fibrils of a β_2-microglobulin fragment using near-field infrared spectroscopy. *J. Am. Chem. Soc.* **2011**, *133*, 7376–7383.

(26) Schierle, G. S. K.; van de Linde, S.; Erdelyi, M.; Esbjörner, E. K.; Klein, T.; Rees, E.; Bertoncini, C. W.; Dobson, C. M.; Sauer, M.; Kaminski C. F. In Situ Measurements of the Formation and Morphology of Intracellular β-Amyloid Fibrils by Super-Resolution Fluorescence Imaging. *J. Am. Chem. Soc.* **2011**, *133*, 12902–12905.

(27) Gosal, W. S.; Morten, I. J.; Hewitt, E. W.; Smith, D. A.; Thomson, N. H.; Radford, S. E. Competing pathways determine fibril morphology in the self assembly of beta2-microglobulin into amyloid *J. Mol. Biol.* **2005**, *351*, 850-864.

(28) Platt, G. W.; Radford, S. E. Glimpses of the molecular mechanisms of β_2-microglobulin fibril formation in vitro: Aggregation on a complex energy landscape. *FEBS Lett.* **2009**, *583*, 2623-2629.

(29) Eichner, T.; Kalverda, A. P.; Thompson, G. S.; Homans, S. W.; Radford, S. E. Conformational conversion during amyloid formation at atomic resolution. *Mol. Cell* **2011**, *41*, 161-172.

(30) Levine III, H. Quantification of β-sheet amyloid fibril structures with thioflavin T. *Methods Enzymol* **1999**, *309*, 274-284.

(31) Nilsson, M. R. Techniques to study amyloid fibril formation in vitro. *Methods* **2004**, *34*, 151-160.

(32) Khurana, R.; Coleman, C.; Ionescu-Zanetti, C.; Carter, S. A.; Krishna, V.; Grover, R. K.; Roy, R.; Singh, S. Mechanism of thioflavin T binding to amyloid fibrils. *J. Struct. Biol.* **2005**, *151*, 229-238.

(33) Sulatskaya, A.L.; Maskevich, A. A.; Kuznetsova, I. M.; Uversky, V. N.; Turoverov, K. K. Fluorescence quantum yield of thioflavin T in rigid isotropic solution and incorporated into the amyloid fibrils. *PLoS One* **2010**, *5*, 15385.

(34) Mishra, R.; Sörgjerd, K.; Nyström, S.; Nordigården, A.; Yu, Y.-C.; Hammarström, P. Lysozyme amyloidogenesis is accelerated by specific nicking and fragmentation but decelerated by intact protein binding and conversion. *J. Mol. Biol.* **2007**, *366*, 1029-1044.

(35) Mishra, R.; Sjolander, D.; Hammarström, P. Spectroscopic characterization of diverse amyloid fibrils in vitro by the fluorescent dye Nile red. *Mol. Biosyst.* **2011**, *7*, 1232-1240.

(36) Zeisel, D.; Dutoit, B.; Deckert, V.; Roth, T.; Zenobi R. Optical Spectroscopy and Laser Desorption on a Nanometer Scale. *Anal. Chem.* **1997**, *69*, 749-754.

(37) Horcas, I.; Fernández, R.; Gómez-Rodríguez, J. M.; Colchero, J.; Gómez-Herrero, J.; Baro, A. M. WSxM: A software for scanning probe microscopy and a tool for nanotechnology. *Rev. Sci. Instrum.* **2007**, *8*, 013705-013708.

List of Publications:

1. V. Dalal, S. Arya, M. Bhattacharya and S. Mukhopadhyay "Human Prion Protein Converts into Polymorphic Amyloids *via* Structurally-Labile Oligomers" ***Biochemistry*** **2015,** *54*, 7505–7513.

2. S. Arya, A. Kumari, V. Dalal, M. Bhattacharya and S. Mukhopadhyay "Appearance of annular ring-like intermediates during amyloid fibril formation from human serum albumin" ***Phys. Chem. Chem. Phys.*** **2015,** *17*, 22862-22871.

3. S. Mukhopadhyay, V. Dalal and S. Arya "Nanoscale optical imaging of protein amyloids" in "**Bionanoimaging: insights into protein misfolding and aggregation**" (invited book chapter; Elseveir **2013**, Editors. Vladimir N. Uversky & Yuri Lyubchenko)

4. V. Dalal, M. Bhattacharya, D. Narang, P.K. Sharma & S. Mukhopadhyay "Nanoscale Fluorescence Imaging of Single Amyloid Fibrils" ***J. Phys. Chem. Lett.*** **2012,** *3*, 1783-1787.
   Video slideshare of our work is available at:
   http://pubs.acs.org/iapps/liveslides/pages/index.htm?mscNo=jz300687f

5. V. Dalal, S. Arya and S. Mukhopadhyay "Ordered Water in Amyloid-competent Oligomers of Human Prion Protein" (manuscript under review).

Presentations and Abstracts:

- Presented a poster entitled " In Vitro Generation of Cytotoxic Amyloids from Human Prion Protein: Molecular Insights into the Conformational Conversion and Nanoscale Assembly " V. Dalal, M. Bhattacharya, S. Arya and S. Mukhopadhyay at the ***Gordon Research Conference on Proteins*** held at Holderness, New Hampshire, USA (June 2015).

- Presented a poster entitled "Insights into the structural heterogeneity of prions and amyloids using fluorescence and Raman" V. Dalal, M. Bhattacharya, S. Arya and S. Mukhopadhyay at the ***National Workshop on Fluorescence and Raman Techniques, FCS 2014*** held at the Indian Institute of Science Education and Research (IISER) Pune (December 2014).

- Presented a poster entitled "The Role of Intrinsically Disordered Region in Surfactant-induced Conformational Change of Human Prion Protein" V. Dalal, M. Bhattacharya, S. Srinivasan and S. Mukhopadhyay at the ***International Symposium on Protein Folding and Dynamics*** held at the National Centre for Biological Sciences (NCBS), TIFR, Bangalore, India (October 2012).